Numerical modelling of binary black hole dynamics in Active Galactic Nuclei discs

M.Sc Thesis

By **ARYAN BHAKE**

Supervisor: Dr. Bhargav Vaidya



INDIAN INSTITUTE OF TECHNOLOGY INDORE

May 20, 2025

Numerical modelling of binary black hole dynamics in Active Galactic Nuclei discs

A THESIS

Submitted in partial fulfillment of the requirements for the awards of the degree

of
Master of Science

by **ARYAN BHAKE**



DEPARTMENT OF ASTRONOMY, ASTROPHYSICS & SPACE ENGINEERING INDIAN INSTITUTE OF TECHNOLOGY INDORE

May 20, 2025



INDIAN INSTITUTE OF TECHNOLOGY INDORE

CANDIDATE'S DECLARATION

I hereby certify that the work which is being presented in the thesis entitled Numerical Modelling Of Binary Black Hole Dynamics In Active Galactic Nuclei Discs in the partial fulfillment of the requirements for the award of the degree of MASTER OF SCIENCE and submitted in the DEPARTMENT OF ASTRONOMY, ASTROPHYSICS AND SPACE ENGINEERING, Indian Institute of Technology Indore, is an authentic record of my own work carried out during the time period from July, 2023 to May, 2025 under the supervision of Dr. Bhargav Vaidya, Associate Professor, Department of Astronomy, Astrophysics And Space Engineering.

The matter presented in this thesis has not been submitted by me for the award of any other degree of this or any other institute.

Signature of the student with date (Aryan Bhake)

This is to certify that the above statement made by the candidate is correct to the best of my/our knowledge.

Signature of the Supervisor

(Dr. Bhargav Vaidya)

Aryan Bhake has successfully given his M.Sc. Oral Examination held on 05/05/2025

Signature(s) of Supervisor(s) of MSc thesis

Date: 10/05/2025

Manswela Chakrakoty Convenor, DPGC Date: 19/05/2025 Programme Coordinator, M.Sc.

Manaueta Chakraborty

Date: 19/05/2025

HoD, DAASE

(Don

Date:

ACKNOWLEDGEMENTS

First and foremost, I would like to express my deepest gratitude to my advisor, Dr. Bhargav Vaidya, for his constant support, patience and insightful guidance throughout the course of this work. Your mentorship has been one of the most formative experiences of my academic life, for which I am sincerely thankful. Your push for making me attend lectures, conferences and interact with the best minds in the world has helped me grow tremendously.

I would specially like to thank Dr. Raj Kishor Joshi whose mentorship and suggestions helped shape the direction and clarity of this thesis. Collaborating with you has taught me not just about physics but also about clarity in communication and the value of different perspectives in research. Thank you for repeatedly entertaining even my silliest questions and doubts. I would also like to thank Dr. Deepika Bollimpalli for helping out with critical feedback and insightful discussions. I am also grateful to the faculty and staff at IIT, Indore for their support.

To my lab mates and peers—thank you for being part of this journey. Whether it was bouncing ideas off one another, sharing frustrations over stubborn code bugs, or just taking breaks to laugh over coffee, your companionship made these long days far more enjoyable. A special mention to Devesh for always being willing to lend an ear or read a draft—even when deadlines loomed.

To my dearest friends outside of academia—you kept me grounded. Your constant check-ins, encouragement and occasional distractions reminded me that life exists beyond LaTeX documents, simulation logs, and arXiv alerts. Your kindness, patience and faith in me have meant more than you know.

To my parents and family—thank you for your unwavering belief in me. Your sacrifice, love and quiet strength have been the foundation on which everything else stands. Thank you for reminding me to take breaks, eat food and believe in myself even when I doubted everything.

This thesis is not just a culmination of my academic efforts, it is the product of every conversation, act of kindness and moment of support I have received along the way. To everyone who has been a part of this chapter, THANK YOU!

ABSTRACT

Binary black holes (BBH) embedded in active galactic nuclei (AGN) discs is a promising system for understanding the astrophysical phenomenon that can produce both gravitational wave (GW) and electromagnetic (EM) signals. This work addresses how the dense, dynamic conditions within such discs influence the evolution and eventual merger of binary black holes. The study is motivated by recent GW detections and the possibility of associated EM counterparts, which suggest that mergers within AGN discs may be more common or more easily observable than previously thought. Previous research has often relied on simplified models that do not fully capture the complexity of binary-disc interactions in these environments. To address this, we employ high-resolution hydrodynamical simulations to investigate the impact of mass ratio, orbital orientation and accretion dynamics on BBH systems within AGN discs. The simulations incorporate a systematic post-processing framework to quantify key parameters including mass accretion, torque and minidisc mass, to comprehensive model the binary's secular orbital evolution. Our results reveal that the orientation of the binary with respect to the disc and the mass ratio of the components significantly affect the transfer of angular momentum, accretion variability and minidisc structure around each black hole. The mean mass accretion rate onto the binary system exhibits dependence on the accretor's mass. These inflows display substantial variability, with their primary modulation frequency corresponding to the binary's orbital period for circular orbital configurations. We find that the smaller/secondary black hole often dominates accretion, especially in systems with unequal masses and that retrograde (oppositely aligned to the disc flow) binaries experience more chaotic flows and stronger angular momentum loss than prograde systems. Our results reveal that the behaviour of embedded within AGN discs deviates significantly from that of binaries evolving in isolated circumbinary environments. Moreover, we find that the orbital hardening of these binaries proceeds on time-scales considerably shorter than their migration through the disc. These findings have important implications for interpreting GW events, predicting EM and understanding the role of gas-rich environments in driving binary black hole mergers. This work contributes to a more complete picture of mergers in AGN and informs future multi-messenger (MM) observational strategies.

CONTENTS

List of Figures

List of Tables

| 1 | Intr | roduction | 1 | | | | | | |
|---|------------------------|---|---|--|--|--|--|--|--|
| | 1.1 | Why study mergers? | 1 | | | | | | |
| | 1.2 | Numerical studies | 4 | | | | | | |
| | | 1.2.1 HydroDynamical studies | 4 | | | | | | |
| | | 1.2.2 MagnetoHydroDynamical studies | 6 | | | | | | |
| | 1.3 | Key Findings | 7 | | | | | | |
| | | 1.3.1 Accretion Variability | 7 | | | | | | |
| | | 1.3.2 Evolution of Unequal Mass Binaries | 8 | | | | | | |
| | | 1.3.3 BBH Embedded inside Discs | 8 | | | | | | |
| | 1.4 | Beyond MHD: Numerical Relativity | 8 | | | | | | |
| | | 1.4.1 Combined Approximation Techniques | 9 | | | | | | |
| | 1.5 | Comparison to Binary Neutron Star mergers | 1 | | | | | | |
| | 1.6 | Applications to astrophysical problems | 2 | | | | | | |
| | | 1.6.1 The Final Parsec Problem | 2 | | | | | | |
| | | 1.6.2 Planets Near Binary Stars | 3 | | | | | | |
| | 1.7 | Objectives | 3 | | | | | | |
| 2 | Met | chodology 14 | 4 | | | | | | |
| | 2.1 Working of CBWaves | | | | | | | | |
| | | 2.1.1 Einstein Field Equations and Harmonic Gauge | 5 | | | | | | |
| | | 2.1.2 Solving the equations | 7 | | | | | | |
| | | 2.1.3 Motion in the Center of Mass Frame | 8 | | | | | | |
| | 2.2 | PLUTO code: Hydrodynamical equations | 0 | | | | | | |
| | 2.3 | Model Parameters | 1 | | | | | | |
| | 2.4 | Simulation Parameters | 3 | | | | | | |
| | | | | | | | | | |

| | 2.5 | Boundary Conditions | 23 |
|----|--------|---------------------------------|----|
| | 2.6 | Post-processing calculations | 24 |
| | | 2.6.1 Torque and Accretion rate | 24 |
| | | 2.6.2 Minidisc Mass density | 25 |
| | | 2.6.3 Mass sloshing | 25 |
| 3 | Resi | ults 2 | 26 |
| | 3.1 | Flow Structure | 26 |
| | 3.2 | Gravitational Torque | 28 |
| | 3.3 | Accretion Variability | 33 |
| | 3.4 | Minidisc Mass Evolution | 34 |
| | 3.5 | Sloshing | 40 |
| | 3.6 | Retrograde Equal-Mass Binaries | 41 |
| | 3.7 | Dependence on sink radius | 43 |
| 4 | Sum | mary 4 | 45 |
| | 4.1 | Main Findings: | 45 |
| 5 | App | endix 4 | 48 |
| | | A.1 The radiation field | 48 |
| | | B.1 Equations of motion | 52 |
| Bi | bliogi | raphy 5 | 57 |

List of Figures

| 1.1 | Merging binary black hole (Credit: NASA GSFC) | 2 |
|-----|--|----|
| 1.2 | ZTF photometry for ZTF19abanrhr (Credit: Graham et al. (2020)) | 3 |
| 1.3 | An illustration depicting a typical BH with its surrounding accretion disc and jet. Insets | |
| | show a time-lapse sequence of radio observations capturing jet activity in the microquasar | |
| | GRS 1915+105, alongside an optical image of the quasar M87's jet. (Image credit: Hubble | |
| | Heritage Team (STScI/AURA), NASA | 5 |
| 2.1 | An illustration of the shearing box model, binary embedded in an AGN disc at distance R | |
| | from a SMBH at the center, a_b is the binary separation | 22 |
| 3.1 | (a): Velocity streamlines for a equal mass fixed binary overlaid on the gas density distri- | |
| | bution. The arrows denote gas velocity vectors in the orbital plane. The spiral arms act | |
| | as conduits for angular momentum transport and the flow morphology exhibits balanced | |
| | stream accretion onto both black holes. The circular streaming near each component | |
| | indicates the presence of rotationally supported minidiscs. (b): Roche lobe contour lines | |
| | for equal mass binary | 27 |
| 3.2 | Plot shows the orbital separation decay with time for different mass ratios. For fixed | |
| | binaries, the separation is kept as $a_b = 1$ (black dashed line) | 29 |
| 3.3 | (a)-(b):Density distribution for $q = 1$ binary with fixed and inspiral orbits at different | |
| | times,respectively. (c)-(d): White dashed Mach number $\mathcal{M} \geq 1$ contour lines to show | |
| | supersonic flow and shock transitions for fixed and inspiral binaries. (e): Time series for | |
| | net Torque imparted onto the binary with a zoomed in region to show variability | 30 |
| 3.4 | (a)-(b):Density distribution for $q = 0.5$ binary with fixed and inspiral orbits at different | |
| | times,respectively. (c)-(d): White dashed Mach number $\mathcal{M} \geq 1$ contour lines to show | |
| | supersonic flow and shock transitions for fixed and inspiral binaries. (e): Time series for | |
| | net Torque imparted onto the binary with a zoomed in region to show variability | 31 |

| 3.5 | (a)-(b):Density distribution for $q = 0.2$ binary with fixed and inspiral orbits at different | |
|------|--|----|
| | times,respectively. (c)-(d): White dashed Mach number $\mathcal{M} \geq 1$ contour lines to show | |
| | supersonic flow and shock transitions for fixed and inspiral binaries. (e): Time series for | |
| | net Torque imparted onto the binary with a zoomed in region to show variability | 32 |
| 3.6 | (a)-(c): Time series of accretion rates for both fixed and inspiral orbits with corresponding | |
| | mass ratios. The blue line shows accretion rate for the primary and the orange line shows | |
| | the accretion rate for the secondary. The green line shows the total accretion rate of the | |
| | binary | 37 |
| 3.7 | (a)-(c): Time series for Minidisc mass density for different mass ratios. The blue line | |
| | shows minidisc mass density for the primary and the orange line shows the minidisc mass | |
| | density for the secondary | 39 |
| 3.8 | Comparison of slosh mass rate for different mass ratios and orbital prescriptions. The | |
| | blue line, orange and green lines show the slosh ate for $q=1.0,0.5,0.2$ respectively | 40 |
| 3.9 | (a)-(b): Density plots for retrograde motion system. (c)-(d): Torque and Accretion time | |
| | series respectively. The blue line shows accretion rate for the primary and the orange line | |
| | shows the accretion rate for the secondary | 42 |
| 3.10 | (a): Density with White dashed Mach number $\mathcal{M} \geq 1$ contour lines to show supersonic | |
| | flow and shock transitions and (b)-(c): Torque time series for sink radii $r_s = 0.02a_b$ and | |
| | $0.08a_b$ respectively | 43 |
| | | |

LIST OF TABLES

| 3.1 | Simulation details and results | • | | | • | • | • | • | • | • | • | • | • | | • | • | | • | • | 34 |
|-----|------------------------------------|---|--|--|---|---|-------|---|---|---|---|-------|---|---|---|---|--|---|---|----|
| 3.2 | Physical units for the simulations | | | | | | | | | | | | | • | | | | | | 35 |

CHAPTER 1

Introduction

Binary black holes (BBHs) mergers are one of the most energetic events in the Universe, releasing huge amount of energy in the form of gravitational waves (GW). Heavy BBH mergers observed so far, on average, have released approximately $\sim 1-3\,M_\odot c^2$ (where M_\odot is the solar mass) in GW energy. For example, GW150914 emitted $(3.0\pm0.5)\,M_\odot c^2\approx (5.4\pm0.9)\times10^{54}$ erg, with peak luminosities reaching $200\,M_\odot c^2\,\mathrm{s^{-1}}$ ($\sim 3-4\times10^{56}\,\mathrm{erg/s}$) (Abbott et al., 2016). The largest luminosities are achieved in equal-mass systems with aligned spins, where both black holes (BH) rotate at their maximum rates.

These mergers have become a focal point of study following the pioneering detections by the LIGO/Virgo/KAGRA (LVK) collaboration which highlighted the importance of dynamical channels in BBH formation. While the gravitational wave signals from these events offer significant insights into the mass, spin and possible eccentricities of the merging black holes, the information they provide about the surrounding environment is limited. Understanding the influence of different environments on BBH mergers is crucial for a complete picture of BBH evolution, as environmental factors can affect orbital decay, accretion rates, and torque exerted on the binary.

1.1 Why study mergers?

Discs around supermassive black holes (SMBHs) in active galactic nuclei (AGNs) present a promising pathway for producing merging BHs. Within these discs, BHs may undergo growth through super-Eddington accretion and repeated mergers, potentially giving rise to high mass BBH systems whose GW events can be observed (Gerosa and Fishbach, 2021). Graham et al. (2023) presented a new opportunity with a detection of an electromagnetic (EM) candidate counterpart to a GW event. Notably, these two recently observed GW events have been suggested as possible mergers of BBHs within AGN discs:

• **GW190521**, merging of two BHs with a combined mass of approximately 150 solar mass (M_{\odot}) , where one BH likely exceeded 65 M_{\odot} (Abbott et al., 2020a,b). This event was

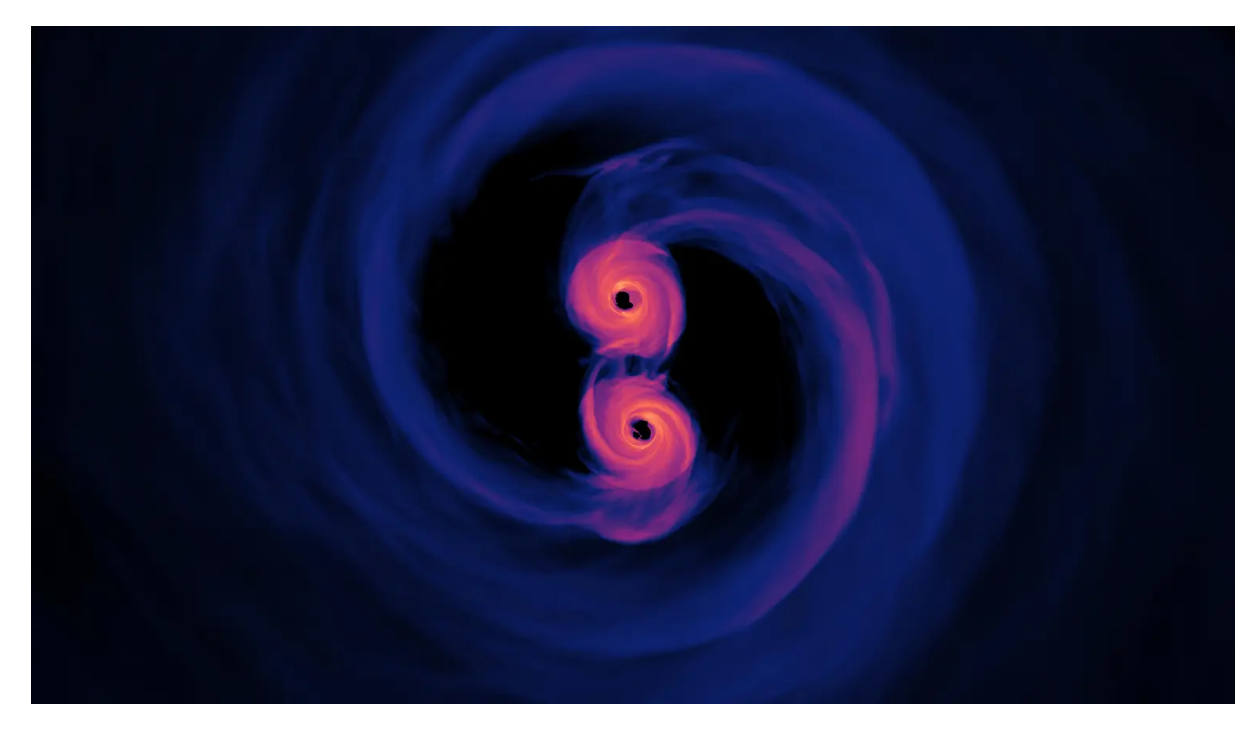


Figure 1.1: Merging binary black hole (Credit: NASA GSFC).

linked to an EM counterpart detected by the Zwicky Transient Facility (ZTF), originating from a known AGN that is spatially coincident with the GW localization (Chen et al., 2022; Graham et al., 2020).

• **GW170817A**, another GW signal detected on the same day as the neutron star merger GW170817, identified in a later independent analysis by Zackay et al. (2021); Gayathri et al. (2020). The large mass and spin alignment of this event has been interpreted as signatures of a merger occurring within an AGN disc.

The event GW190521 has captured considerable attention from gravitational wave astronomers since its detection in 2019. GW190521 represents both the most massive black hole binary merger observed by LVK and the first detection of a merger involving an intermediate mass black hole (IMBH). This aspect is especially intriguing to researchers interested in the formation and evolution of black holes as IMBHs spanning roughly 100 to 100,000 M_{\odot} lack obvious formation pathways. The challenge arises from the fact that stars exceeding around 50–80 M_{\odot} are not expected to directly collapse into black holes. This upper limit is influenced in part by pair instability supernovae which disrupts the star before it can form such a massive black hole. Additionally, most stars do not reside in dense enough environments to allow the extensive accretion required for stellar black holes to grow into the intermediate mass range especially at a rate that would make these black holes common. This theoretical absence of black holes within this mass range is known as the "upper mass gap." Observational data (still inconclusive) suggests a decline in merger rates for systems with primary masses approaching this boundary, around $80 M_{\odot}$ (Abbott et al., 2023).

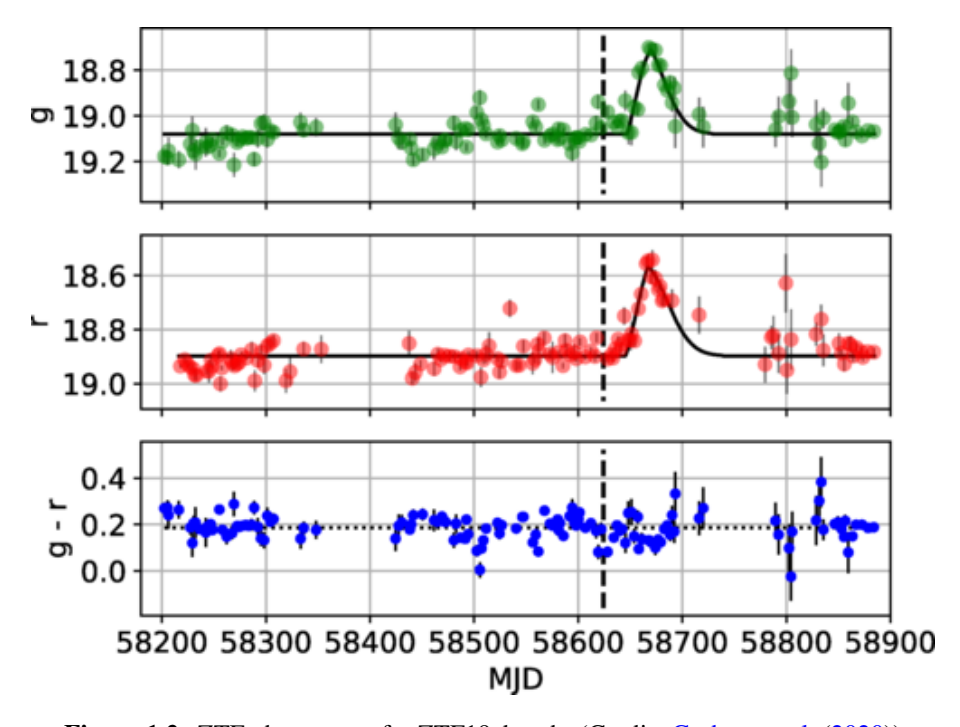


Figure 1.2: ZTF photometry for ZTF19abanrhr (Credit: Graham et al. (2020))

Further interest in GW190521 was sparked when only 34 days from its detection, ZTF observed a second rare event near the predicted sky location of GW190521. This event, a sudden brightening in the photometric observation of AGN J124942.3+344929, was designated ZTF19abanrhr shown in Fig 1.2. Such "flares" are expected outcomes of some models for black hole mergers within AGN discs, as the merger's dynamical interactions can heat surrounding gas. Given that AGN J124942.3+344929 had shown stable light emission in the months preceding this flare, the possibility of a connection between these two rare astrophysical events has intrigued researchers even further (Graham et al., 2020, 2023).

Although the potential connection of these events to BBHs in AGN discs remains speculative (Ashton et al., 2021), these observations suggest a potential new channel for BBH formation that warrants further investigation. Studies of merging binary black holes in AGN discs have commonly relied on simplified models, primarily doing population synthesis calculations (McKernan et al., 2012, 2014, 2018, 2019, 2022; Yang et al., 2019; Tagawa et al., 2020, 2021). While such modelling helps build a statistical understanding of the overall process and its observational implications, they largely simplify the interaction between BBHs and AGN discs. Most binary—disc interaction prescriptions in these models are adapted from theories developed for circumstellar and protoplanetary discs, however such environments differ significantly from AGN conditions.

1.2 Numerical studies

1.2.1 HydroDynamical studies

To date, only a limited number of two-dimensional (2D) simulations have examined the dynamics of BBHs embedded in AGN discs (Baruteau et al., 2010; Li et al., 2021, 2022; Li and Lai, 2022). These studies typically assume that the binary loses angular momentum through its interaction with the surrounding disc, particularly the outer regions (Pringle, 1991; MacFadyen and Milosavljević, 2008), leading to a contraction of the binary separation. This assumption originates from extending the classical theory of satellite—disc interactions, traditionally applied to extreme mass ratio systems, into the binary regime (Lin and Papaloizou, 1979). In this theoretical framework, the binary exchanges angular momentum with the disc through Lindblad resonances. Because the circumbinary disc (CBD) rotates more slowly than the binary, the gas response lags behind, producing non-axisymmetric density waves that exert a net negative torque on the binary.

However, recent high-resolution numerical studies challenge this picture, showing that isolated binaries often undergo orbital expansion instead (Tang et al., 2017; Moody et al., 2019; Muñoz et al., 2019, 2020; Duffell et al., 2020; Tiede et al., 2020; Dittmann and Ryan, 2021, 2022; D'Orazio and Duffell, 2021; Zrake et al., 2021). This apparent discrepancy arises primarily from the omission of circumsingle discs (CSDs) (or minidisc) structures in these earlier analyses. These minidiscs, which form around each black hole, are now understood to significantly alter the torque balance, typically contributing positive angular momentum to the binary system. Although such expansion has raised questions about whether BBHs in AGN discs can merge efficiently, this behaviour appears to be specific to configurations with circular, equal-mass binaries.

Ultimately, the coupled evolution of the binary and its gaseous environment, driven by gravitational and accretion torques plays a critical role in determining the binary's fate. A comprehensive understanding of disc-binary interactions is therefore vital for modelling the distribution of stellar and black hole binaries, and for explaining the mechanisms by which a CBD can promote orbital inspiral and hence a merger.

Numerous studies (eg.Armitage and Natarajan (2002); Farris et al. (2014)) have modelled the loss of angular momentum from binary systems to the surrounding disc, suggesting that disc-gas-assisted orbital migration may play a crucial role in facilitating supermassive BBH mergers at separations too wide for GW radiation (> 0.1 pc) to contribute significantly to angular momentum loss. However, there have been conflicting reports in previous studies regarding how the average mass accretion rate of a binary compares to a single star of equivalent mass. Li and Lai (2022) (hereafter LL22) conducted a series of 2-D hydrodynamical simulations of binaries embedded in AGN discs using a shearing box model. Their results indicate that

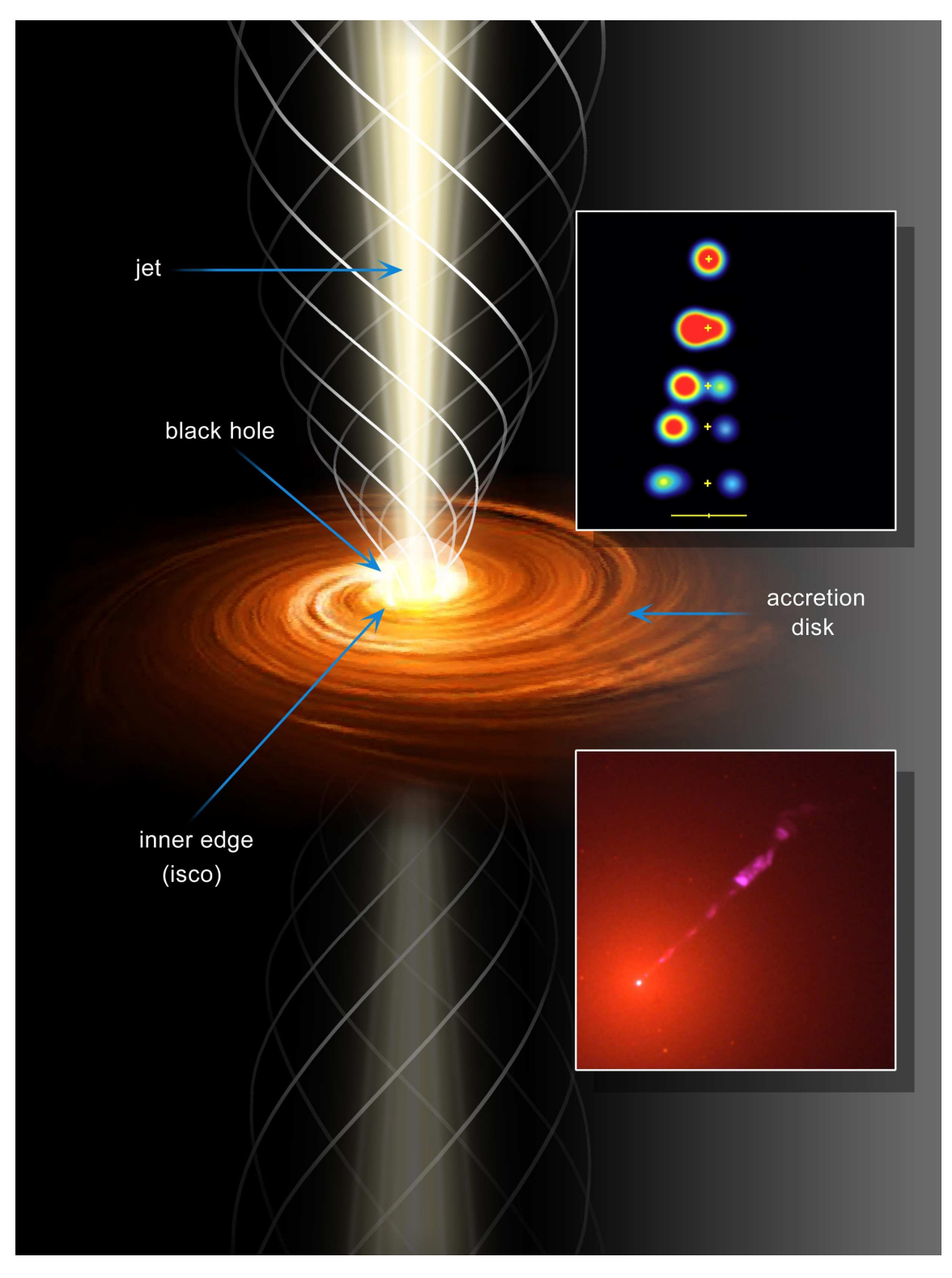


Figure 1.3: An illustration depicting a typical BH with its surrounding accretion disc and jet. Insets show a time-lapse sequence of radio observations capturing jet activity in the microquasar GRS 1915+105, alongside an optical image of the quasar M87's jet. (Image credit: Hubble Heritage Team (STScI/AURA), NASA

the accretion around the binary evolves into a quasi-steady state after a significant amount of viscous time. These findings suggest that the hydrodynamical evolution of binaries embedded in AGN discs may differ substantially from the behaviour of isolated binaries interacting with their own CBD.

1.2.2 MagnetoHydroDynamical studies

The study of BBH mergers within gaseous environments is gaining considerable interest, particularly in the context of AGN discs where dense ambient gas can influence the orbital evolution of the binary. A critical extension of these studies involves the incorporation of magnetic fields, which are ubiquitous in astrophysical discs and can substantially alter the dynamics of gas flow and accretion behaviour near the binary.

While early hydrodynamical simulations of BBH mergers in circumbinary discs focused on purely viscous or pressure-driven accretion processes, recent efforts have begun to explore magnetized disc environments. A handful of simulations have incorporated magnetic fields into the disc structure, providing deeper insight into the nature of gas inflow and angular momentum transport in such systems (Mishra and Calcino, 2024; Ressler et al., 2025; Most and Wang, 2024).

Most and Wang (2024) performed high-resolution 3-D Newtonian MHD simulations to investigate the behaviour of magnetized circumbinary discs. Their study revealed that, under certain conditions, the inner cavity surrounding the binary can host magnetically arrested disc (MAD) configurations. In these cases, magnetic flux accumulation near the binary leads to a suppression of continuous accretion. Instead, accretion proceeds in episodic bursts triggered by large-scale magnetic flux eruptions. This behaviour deviates significantly from the quasi-steady accretion observed in non-magnetized or weakly magnetized discs and has important implications for the variability of EM signatures associated with BBH mergers.

The variable nature of accretion in such environments introduces a new avenue for detecting and interpreting potential EM counterparts to BBH mergers. For instance, the sudden reconnection and rearrangement of magnetic fields during flux eruptions can produce transient high-energy flares or jet-like outflows, particularly if a small-scale magnetized disc forms around one or both black holes. These periodic features could manifest as precursors or afterglows in the EM spectrum, providing complementary observables alongside the gravitational wave signal (Most and Wang (2024) and references therein).

Moreover, magnetic stresses can contribute to angular momentum transport in regions where viscosity alone is insufficient, potentially enhancing the inspiral rate and modifying the final coalescence dynamics. The interaction between magnetic fields and the mini-discs or circumbinary gas may also affect the spin alignment of the binary components, which is a key observable in gravitational wave parameter estimation.

As magnetic field effects become increasingly incorporated into general relativistic magneto-hydrodynamic (GRMHD) frameworks, future simulations will enable more accurate modelling of both the dynamics and potential observables of BBH mergers in astrophysically realistic environments. These developments underscore the necessity of including MHD effects in any comprehensive treatment of BBH systems embedded in dense, magnetized media.

1.3 Key Findings

This section summarizes key findings from recent simulation efforts, particularly those conducted with the AREPO code (Muñoz and Lai, 2016; Muñoz et al., 2020; Siwek et al., 2022), alongside complementary results obtained using the PLUTO code (Miranda et al., 2016). Where appropriate, we also incorporate insights from other numerical studies to present a broader perspective on the current understanding of binary–disc interactions. The simulations under consideration predominantly investigate systems with near-equal mass binaries ($q \approx 1$), embedded in discs modeled as extended or effectively infinite, where a constant mass inflow is maintained at large radii.

1.3.1 Accretion Variability

For extended disc models with a sustained mass injection rate \dot{M}_0 at the outer boundary, the binary–disc system may evolve toward a quasi-steady configuration. In this state, the time-averaged accretion rate through the CBD and onto the binary components satisfies $\langle \dot{M}_b \rangle = \langle \dot{M}_1 \rangle + \langle \dot{M}_2 \rangle$, equating to \dot{M}_0 . Despite this steady average, the instantaneous accretion onto the cavity and the individual black holes often displays pronounced variability on timescales comparable to the binary orbital period (Muñoz and Lai, 2016; Miranda et al., 2016). This modulation reflects the dynamic nature of gas inflow near the cavity edge and the episodic structure of the accretion streams feeding the minidiscs.

Simulating circumbinary accretion over extended periods presents unique challenges due to the broad spatial scales and diverse timescales involved. Over longer simulation times, the binary's orbit may evolve toward mass equality between its components. Contrary to previous assumptions that circumbinary accretion universally causes binary orbital decay, recent findings reveal that the secular evolution of binary orbits may depend heavily on factors like eccentricity e_b , mass ratio q and thermodynamics of the gas being accreted (Lai and Muñoz, 2023).

1.3.2 Evolution of Unequal Mass Binaries

The total torque on the binary, $\langle \mathcal{T}_b \rangle$, can be computed by directly summing the gravitational, pressure and accretion torque from the gas onto each component of the binary:

$$\langle \mathcal{T}_b \rangle = \langle \mathcal{T}_b \rangle_{\text{grav}} + \langle \mathcal{T}_b \rangle_{\text{acc}} + \langle \mathcal{T}_b \rangle_{\text{pres}},$$

where \mathcal{T}_b denotes the angular momentum rate. For a binary separation a_b much larger than the component radii, the torque due to spins are negligible, leading to a total torque primarily acting on the binary given by just the gravitational and in some scenarios accretion torque.

Early simulations, such as those by Bate et al. (2002) showed that accretion flows in circumbinary systems are sensitive to q_b . Generally, the secondary tends to grow faster in mass than the primary, a trend confirmed in circular binaries with preferential accretion onto the secondary. Accretion variability was also observed to depend on the binary mass ratio. (Farris et al., 2014; Duffell et al., 2020; Muñoz et al., 2020)

1.3.3 BBH Embedded inside Discs

The hydrodynamics of binary systems within AGN discs are distinctly different from those in isolated cases. In these cases, accretion dynamics are influenced by the large scale flows within the AGN disc and the gravitational potential of the central SMBH shapes the behaviour of the binary. Some key results from these simulations indicate that binaries embedded in AGN discs can experience rapid orbital decay rates. Prograde, equal-mass binaries tend to contract due to dynamical friction from the trailing spiral patterns and retrograde binaries experience faster orbital decay. The orbital evolution also appears to vary with the equation of state (EOS) of the surrounding gas, where binaries in an isothermal EOS experience expansion, while those with a stiffer EOS generally experience contraction. Eccentric binaries in these setups often show eccentricity damping, leading to more circular orbits over time (Li and Lai, 2022; Dittmann and Ryan, 2021). The 2D shearing box approximation limits LL22 results to be valid for only cases where Hill radius is of comparable scale to the height of the disc. Dempsey et al. (2022) demonstrated that 3-D simulations yield more negative gravitational torques compared to 2-D, highlighting the importance of vertical structure and 3D flow dynamics in accurately capturing binary—disc interactions.

1.4 Beyond MHD: Numerical Relativity

A comprehensive theoretical treatment of these compact gravitational wave sources requires developing a sufficiently general solution to Einstein's field equations that applies to a wide range of matter configurations. This solution must capture the key physical mechanisms involved in

both the generation and propagation of gravitational waves from the source to a distant detector, while also accounting for the back-reaction of the emitted radiation on the dynamics of the source itself. Once established, such a framework can then be tailored to specific astrophysical systems, such as compact binaries in quasi-circular inspirals that lose orbital energy through gravitational wave emission prior to merger.

However, for general source configurations, solving Einstein's equations exactly is often difficult. Hence, one must rely on approximation schemes to make progress. The objective of these approximation methods is to extract physically reliable predictions from general relativity that can be tested against observational data. Nevertheless, these techniques sometimes lack a rigorous mathematical foundation directly rooted in the full theory, and their connection to first-principles formulations may not always be transparent (Futamase and Schutz, 1983; Rendall, 1992).

Among these approximation methods, the post-Newtonian (PN) framework stands out as the most successful and widely applied. First developed in the early 20th century by Droste (1917) and later expanded by Lorentz and Droste (1937), the PN formalism has played a central role in some of the major achievements of general relativity. It provides a systematic expansion of the equations of motion and gravitational radiation in powers of v/c, making it particularly suited for modelling systems where gravity is strong but not fully relativistic. Three particularly notable applications of the post-Newtonian approximation include:

- 1. The motion of point masses at 1st post-Newtonian (1PN) level, which is routinely employed in high-precision modelling of planetary motion within the Solar System (Einstein et al., 1938).
- 2. The derivation of the radiation-reaction force at 2.5PN order, which accounts for the energy and angular momentum loss due to gravitational radiation. This effect has been experimentally confirmed through pulsar timing measurements in binary systems such as the Hulse–Taylor pulsar (Taylor et al., 1979; Taylor and Weisberg, 1982; Taylor, 1993) and the double pulsar (Kramer and Wex, 2009).
- 3. The modelling of gravitational wave templates for inspiralling compact binaries, which requires accurate modelling of both orbital dynamics and waveform structure to high PN orders, essential for gravitational wave detection and source characterization (Cutler et al., 1993; Cutler and Flanagan, 1994).

1.4.1 Combined Approximation Techniques

The merging of two compact objects necessitates a continuous loss of their orbital binding energy through the emission of gravitational radiation. This leads to a reduction in their orbital separation and an increase in their orbital frequency. Consequently, the gravitational-wave

signal frequency doubles the orbital frequency for the primary harmonics, producing a "chirp" over time until the eventual collision and merging of the objects. Most inspiralling compact binaries maintain nearly circular orbits, aside from the slow inspiral, because gravitational radiation reaction forces rapidly circularize the orbit. This phenomenon results from angular momentum emitted via gravitational waves, causing a steady decline in orbital eccentricity. The primary challenge is associating the gravitational wave signal h_{ij} detected in the wave zone with the source's stress-energy tensor $T^{\alpha\beta}$. Solving Einstein's equations using various approximation schemes, each suited for specific physical scenarios, is essential. Significant methods include the PN expansion using powers of 1/c, the post-Minkowskian (PM) expansion using powers of G, multipole expansions (based on the source's radius), far-zone expansions in 1/R, and expansions based on small mass ratios in binaries. The PN method is effective for sources with relatively weak internal gravity and slow movement, but it is only applicable in the near-zone, which restricts its use under asymptotic boundary conditions. When applying the PN approximation to the inspiralling phase of a BBH, strong internal gravity must be acknowledged.

Typically, the PN approximation presumes weak gravitational fields throughout, including within the material source. By invoking the strong equivalence principle, it is maintained that the external gravitational field directing the binary system's orbital motion is unaffected by the internal structure of its components, up to tidal interactions. Consequently, it is predicted that outcomes derived under the weak gravity assumption are also valid for neutron star binaries. In contrast, the PM method applies throughout spacetime for weakly gravitating systems and can be re-expanded into a PN series, making it more fundamental. It also underlies the multipole and far-zone expansions. In this context, the source is considered "post-Newtonian" if it is both weakly stressed and slowly moving. A small dimensionless parameter ϵ , estimated by

$$\epsilon \equiv \max \left\{ \left| \frac{T^{0i}}{T^{00}} \right|, \left| \frac{T^{ij}}{T^{00}} \right|^{1/2}, \left| \frac{U}{c^2} \right|^{1/2} \right\} \ll 1, \qquad (1.1)$$

where U is the Newtonian potential, quantifies the validity of this assumption. This parameter basically shows a slow motion $\epsilon \sim v/c$ where v is velocity. When $1/c \ll 1$ small remainders would be $O(1/c^n)$. For self-gravitating sources, $|U/c^2|^{1/2} = O(1/c)$. Post-Newtonian corrections are denoted $O(1/c^n)$, and terms of order n beyond Newtonian gravity are denoted as $\frac{n}{2}$ PN.

At leading order $(1/c \to 0)$, gravitational radiation arises from the time-varying quadrupole moment. Higher-order PN corrections incorporate additional multipole moments. The quadrupole approximation itself reflects radiation-reaction effects at 2.5PN order.

Multipole expansions are a critical component of these models, though their application in General Relativity (GR) is complex due to GR's inherent nonlinearity and tensorial characteristics. In linear GR, the mass and current multipole moments are defined at future null infinity, grounded in the foundational works of Papapetrou (1962); Peters (1964); Sachs and Bergmann

(1958); Thorne (1980). Modern approaches utilize symmetric trace-free (STF) mass and current moments Damour and Iyer (1991). In the context of fully non-linear theory, radiative multipole moments manifest in the 1/R expansion of the metric at null infinity. Bondi et al. (1962); Sachs (1962); Penrose (1963) established the geometric framework for such spacetimes, but these radiative moments are distinct from source moments, which are better expressed through integrals of the source's energy-momentum distribution.

To address nonlinearities, the PM expansion is employed both within and beyond the source regions (Thorne and Kovàcs, 1975; Crowley and Thorne, 1977). Blanchet and Damour (1986); Blanchet (1987) developed an alternative multipolar expansion in complete GR, which introduced "source" multipole moments. These are calculated using a PM expansion of the vacuum field equations outside the source. This process results in the multipolar-post-Minkowskian (MPM) formalism, applicable throughout the weak-field region and particularly effective for determining radiative moments as nonlinear functions of the source moments. This method, while comprehensive, provides explicit source multipole formulas mainly for PN sources. The technique of matched asymptotic expansions (Burke and Thorne, 1970; Poujade and Blanchet, 2002) is used to align the PN near-zone expansion with the MPM exterior solution. This MPM-PN framework establishes a solid analytical methodology for generating gravitational waves, encompassing all pertinent PN corrections and nonlinear multipole interactions, including tails and memory effects (Blanchet and Damour, 1988, 1992). Recent advancements employing scattering amplitudes and effective field theory (EFT) have progressed the PM framework to higher orders (Bern et al., 2021; Dlapa et al., 2022; Mougiakakos et al., 2021). Significantly, EFT-based waveforms align with those derived from the MPM-PN formalism up to 2.5PN order (Bini et al., 2023).

1.5 Comparison to Binary Neutron Star mergers

While the focus of this thesis is on binary black hole dynamics, it is instructive to compare BBH systems with binary neutron star (BNS) mergers, as both represent critical sources for gravitational wave astronomy but exhibit fundamentally different physics and observational signatures. Unlike BBHs, which are characterized primarily by their mass and spin parameters, BNS systems incorporate complex nuclear physics, matter effects and potentially rich EM signatures. BNS mergers uniquely differ from BBH mergers in their post-merger evolution and observable outputs. A key distinction lies in the fate of the merger remnant. When two neutron stars merge, the outcome depends critically on their total mass relative to the maximum mass of a non-rotating neutron star. Recent numerical simulations have established a quasi-universal relation where prompt collapse to a black hole occurs when the binary mass exceeds approximately 1.41 times the maximum mass of static neutron stars (Ecker et al., 2025). Below this threshold, the merger typically results in a short-lived hypermassive neutron star before

eventually collapsing to a black hole.

The presence of matter in BNS systems introduces significant tidal effects absent in BBH mergers. During the late inspiral phase, each neutron star experiences tidal deformation due to the gravitational field of its companion, affecting the orbital dynamics and leaving distinctive imprints in the gravitational waveform. These tidal signatures potentially provide valuable constraints on the neutron star's EOS, offering insights into nuclear physics at densities currently unreachable by laboratory experiments.

The most striking difference between BNS and BBH mergers is the presence of EM counterparts. While BBHs in isolation are not expected to produce significant EM emissions (except in special environments like AGN discs as studied in this thesis), BNS mergers reliably generate a lot of EM signals. These include short gamma-ray bursts (sGRBs) and thermal emissions powered by the radioactive decay of newly synthesized heavy elements in the neutron-rich ejecta. The above mentioned landmark multi-messenger detection of GW170817 in 2017 provided definitive confirmation of these theoretical predictions.(Gottlieb et al., 2023)

The composition of neutron stars further complicates the merger dynamics. Recent theoretical work suggests that exotic particles like hyperons may be present in neutron star cores, potentially altering the thermal properties of the merger remnant. Numerical simulations indicate that hyperonic equations of state induce higher heat capacity and lower thermal pressure compared to purely nucleonic models, resulting in characteristic shifts in the post-merger gravitational wave frequency spectrum. The rich phenomenology of BNS mergers offers complementary insights to BBH studies. In contrast to BBH mergers, both BNS and black hole-neutron star (BH-NS) systems serve as potential laboratories for studying the equation of state of supranuclear matter and the physics of relativistic jets. The emission mechanisms in these systems depend sensitively on mass ratios, component spins and orbital parameters, providing multiple constraints on fundamental physics.(Duez, 2025)

1.6 Applications to astrophysical problems

Circumbinary accretion impacts numerous astrophysical systems, influencing the evolution of binary stars, massive black hole binaries (MBHBs), planetary systems around binaries, and the dynamics of post-main sequence binaries.

1.6.1 The Final Parsec Problem

In hierarchical galaxy formation, mergers between massive black holes (MBHs) are expected due to the formation of MBHBs following galaxy collisions. Observational evidence of dual AGNs with kiloparsec scale separations supports the existence of MBHBs as merger remnants (Goulding et al., 2019). However, evolving MBHBs from kiloparsec separations down to the

gravitational wave driven regime (less than 0.01) poses the "final parsec problem." Circumbinary accretion could provide a gas dynamical solution to this problem by driving the inward migration of MBHBs through interaction with a surrounding CBD. This process resembles the inward migration of massive planets in protoplanetary discs, and could be instrumental in bringing MBHBs into the detection range of low-frequency gravitational wave observatories such as LISA.

1.6.2 Planets Near Binary Stars

Planets orbiting binary stars like those discovered by the Kepler mission provide unique insights into CBD dynamics. Many of these circumbinary planets are found close to the stability limit of their host binary commonly interpreted as migration from further out in the disc. The dynamics within the CBD are crucial in shaping the final positions of these planets and the strong gravitational forces within these environments create a unique evolution pathway for planets in binary systems (Lai and Muñoz, 2023).

1.7 Objectives

The primary objective of this thesis is to investigate the hydrodynamical evolution of BBHs embedded within an AGN disc, using the PLUTO code (Mignone et al., 2007). By simulating BBHs with varying mass ratios and modelling their inspiral phase, we aim to understand how these parameters influence the orbital dynamics, accretion behaviour and potential EM signatures of the system. In particular, this study focuses on quantifying the impact of the circumbinary gas and the formation of individual minidiscs around the black holes on the binary's evolution. We seek to address the following key questions:

- How does the mass ratio of the binary affect the torque exerted by the surrounding gas?
- How does the mass and evolution of the individual minidiscs change during the inspiral, and what role do they play in regulating the accretion rate and angular momentum exchange?
- Under what physical conditions might these mergers produce detectable EM counterparts, and how can such signals be used to probe the structure and state of the AGN disc?

CHAPTER 2

METHODOLOGY

We utilize the PLUTO code to simulate the evolution of binaries with a shearing box approximation. It utilizes a conservative numerical framework based on finite volume and finite difference methods to solve hydrodynamic equations, employing high-resolution shock-capturing Godunov-type algorithms. A key advantage of PLUTO is its flexibility, allowing us to customise simulation setups to match specific astrophysical systems. For time integration, it offers a range of schemes, including Runge-Kutta (RK) methods, MUSCL-Hancock for hyperbolic partial differential equations, and advanced techniques such as Super-Time-Stepping or RK-Legendre for efficiently handling parabolic terms. To achieve high accuracy and minimize numerical oscillations, PLUTO provides a variety of reconstruction schemes, such as slope-limited Total Variation Diminishing (TVD), Weighted Essentially Non-Oscillatory (WENO), Piecewise Parabolic Method (PPM) and MP5. Additionally, it supports multiple Riemann solvers, including Roe, HLLD, HLLC, and Two-Shock solvers for resolving sharp discontinuities, along with simpler options like HLL and Lax-Friedrichs for general applications.

We also use the CBWaves code (Csizmadia et al., 2012) to model the binary's inspiral trajectory. It also helps in constructing the GW templates in a fast and accurate way. This code applies the PN framework by using the analytical setups developed till date (Kidder, 1995). The gravitational radiation field, calculated simulataneously by evaluating the analytical waveforms. Time integration is done by RK4 method. The input parameters such as masses, spins and initial eccentricity are given by hand.

Section 2.1, 2.2, 2.3 and 2.4 describe the framework, setup and parameters used in our model to simulate the flows surrounding the binary. Section 2.5 provides an overview of the Boundary Conditions (BC) chosen for the study. In section 2.6, we outline the method employed to calculate the torque and accretion rate.

2.1 Working of CBWaves

Employing the PN formalism as outlined in Section 1.4.1, we solve the equations of motion in the center-of-mass frame. Within this framework, radiation-reaction effects associated with the emission of gravitational waves to infinity, are incorporated through damping terms that first appear at the 2.5PN order, corresponding to corrections of order $\epsilon^{5/2}$. The formalism adopts a two-zone decomposition of spacetime: a near zone and a wave zone. The gravitational field is modeled as a perturbation of flat spacetime, and the Einstein equations are solved separately in each zone.

In the near zone, where the energy-momentum tensor is non-zero and retardation effects can be neglected due to the slow-motion approximation, the PN expansion is applied. Conversely, in the wave zone—governed by the vacuum Einstein equations—the PM expansion is utilized. These regions overlap in an intermediate domain, and a matching procedure ensures consistency between the two solutions. This approach enables the gravitational radiation field observed at large distances to be expressed in terms of integrals over the source's multipole moments, effectively encoding its internal structure.

For compact binary systems, these source integrals are typically evaluated under the assumption that the components can be treated as point masses. While this simplification facilitates analytical progress, it introduces certain subtleties at the 3PN order, which are discussed in greater detail by Csizmadia et al. (2012). In our implementation, the orbital dynamics of the binary are computed up to 3.5PN accuracy, while the gravitational waveform is modelled up to the 2PN level.

2.1.1 Einstein Field Equations and Harmonic Gauge

The Einstein field equations are derived by performing a variation of the total action with respect to the spacetime metric $g_{\alpha\beta}$:

$$S = \frac{c^3}{16\pi G} \int d^4x \, \sqrt{-g} \, R + S_m[\Psi, g_{\alpha\beta}], \tag{2.1}$$

where the first term represented the Einstein-Hilbert action describing the gravitational field, R is the Ricci scalar, which measures the curvature and S_m accounts for the matter contribution, with Ψ representing the matter fields. Varying this action yields a system of ten second-order partial differential equations, here the spacetime indices are greek $\mu, \nu = 0, 1, 2, 3$, spatial indices are Latin i, j = 1, 2, 3:

$$G^{\alpha\beta}[g,\partial g,\partial^2 g] = \frac{8\pi G}{c^4} T^{\alpha\beta}[\Psi,g], \tag{2.2}$$

where $G^{\alpha\beta}=R^{\alpha\beta}-\frac{1}{2}Rg^{\alpha\beta}$ is the Einstein tensor and $T^{\alpha\beta}=\frac{2}{\sqrt{-g}}\frac{\delta S_m}{\delta g_{\alpha\beta}}$ denotes the matter

stress-energy tensor. The Bianchi identity enforces conservation of energy-momentum:

$$\nabla_{\mu}G^{\alpha\mu} = 0 \quad \Rightarrow \quad \nabla_{\mu}T^{\alpha\mu} = 0. \tag{2.3}$$

To facilitate calculations, one employs harmonic coordinates, which satisfy the condition:

$$H^{\alpha} \equiv \partial_{\mu} h^{\alpha \mu} = 0, \tag{2.4}$$

where the metric perturbation is defined as:

$$h^{\alpha\beta} = \sqrt{-g}g^{\alpha\beta} - \eta^{\alpha\beta}.$$
 (2.5)

Here, g denotes the determinant of the spacetime metric, defined as $g \equiv \det(g_{\alpha\beta})$, and $\eta^{\alpha\beta}$ refers to an auxiliary Minkowski metric, given by $\eta^{\alpha\beta} \equiv \operatorname{diag}(-1,1,1,1)$. Adopting this coordinate system facilitates a perturbative treatment of gravity by expressing the physical metric as a deviation from flat spacetime. This approach is particularly useful for analyzing gravitational waves, as it enables the field equations to be reformulated in terms of small perturbations propagating on a fixed Minkowskian background.

In harmonic coordinates, the field equations reduce to:

$$\Box h^{\alpha\beta} - \partial H^{\alpha\beta} = \frac{16\pi G}{c^4} \tau^{\alpha\beta},\tag{2.6}$$

with the flat-space d'Alembertian operator $\Box = \eta^{\mu\nu}\partial_{\mu}\partial_{\nu}$ and

$$\partial H^{\alpha\beta} = \partial^{\alpha} H^{\beta} + \partial^{\beta} H^{\alpha} - \eta^{\alpha\beta} \partial_{\mu} H^{\mu}. \tag{2.7}$$

The effective stress-energy pseudo-tensor is:

$$\tau^{\alpha\beta} = |g|T^{\alpha\beta} + \frac{c^4}{16\pi G}\Lambda^{\alpha\beta},\tag{2.8}$$

with $\Lambda^{\alpha\beta}$ containing the non-linear gravitational self-interaction terms. The conservation law (2.3) follows from:

$$\partial_{\mu}\tau^{\alpha\mu} = 0 \quad \Rightarrow \quad \nabla_{\mu}T^{\alpha\mu} = 0.$$
 (2.9)

Assuming harmonic gauge, the source term becomes:

$$\Lambda^{\alpha\beta} = \Lambda_{\text{barm}}^{\alpha\beta} + (\text{gauge terms}), \tag{2.10}$$

where $\Lambda_{\text{harm}}^{\alpha\beta}$ includes all non-linear terms up to fourth order in the perturbation $h^{\alpha\beta}$.

In GR, the Einstein field equations are highly non-linear and exhibit general covariance, meaning the form of the equations remains invariant under arbitrary smooth coordinate trans-

formations. This invariance introduces a gauge freedom in choosing the coordinate system or, equivalently, the metric perturbation $h^{\alpha\beta}$ used in perturbative expansions. To extract physically meaningful solutions, and to ensure the field equations form a "well-posed" hyperbolic system suitable for evolution, one must fix this gauge freedom by imposing additional conditions. The harmonic (or de Donder) gauge condition,

$$\partial_{\beta}\bar{h}^{\alpha\beta} = 0, \tag{2.11}$$

where $\bar{h}^{\alpha\beta} = h^{\alpha\beta} - \frac{1}{2}\eta^{\alpha\beta}h$ is the trace-reversed metric perturbation, simplifies the Einstein equations into a wave-like form:

$$\Box \bar{h}^{\alpha\beta} = -16\pi T^{\alpha\beta} + \Lambda_{\text{harm}}^{\alpha\beta}.$$

This gauge choice effectively reduces the system to ten coupled wave equations for the components of $\bar{h}^{\alpha\beta}$, allowing for the use of standard Green's function techniques, energy estimates, and iterative perturbative approaches. Furthermore, the harmonic gauge maintains manifest Lorentz invariance and is well suited for PN expansions.

We will seek approximate solutions with the following assumptions:

- 1. The matter stress energy tensor $T^{\alpha\beta}$ has compact spatial support.
- 2. The matter fields are smooth: $T^{\alpha\beta} \in C^{\infty}(\mathbb{R}^3)$. We consider a smooth hydrodynamic fluid system that is characterized by Euler-type equations with strong relativistic corrections.
- 3. A PN source, characterized by a small parameter $\epsilon \ll 1$.
- 4. The system was stationary in the distant past:

$$\partial_t h^{\alpha\beta}(\mathbf{x}, t) = 0 \quad \text{for } t \le -\mathcal{T}.$$
 (2.12)

This final condition enforces asymptotic flatness by eliminating incoming radiation from past null infinity, aligning the solution with realistic astrophysical systems.

2.1.2 Solving the equations

The primary input parameters for the system include the initial relative separation between the two compact objects, defined as $\mathbf{r} = \mathbf{x}_1 - \mathbf{x}_2 = r \,\hat{\mathbf{n}}$, the individual masses m_i , the specific spin magnitudes s_i , and the initial orbital eccentricity e. Rather than working with the conventional spin angular momentum vectors \mathbf{S}_1 and \mathbf{S}_2 , the formulation adopts dimensionless specific spin vectors \mathbf{s}_i , which are related to the physical spin via $\mathbf{S}_i = m_i^2 \mathbf{s}_i$. Each specific spin vector is represented as $\mathbf{s}_i = (s_{ix}, s_{iy}, s_{iz})$, with a magnitude determined by $s_i = \sqrt{s_{ix}^2 + s_{iy}^2 + s_{iz}^2}$. For black

holes, s_i is generally restricted to the range $0 < s_i < 1$, while typical neutron star configurations impose a more conservative upper limit, with $0 < s_i < 0.7$.

Using the above field equations, the gravitational radiation field h_{ij} observed far from the source can be expressed as (Kidder, 1995):

$$h_{ij} = \frac{2G\mu}{c^4D} \left(Q_{ij} + P^{0.5}Q_{ij} + PQ_{ij} + PQ_{ij}^{SO} + P^{1.5}Q_{ij} + P^{1.5}Q_{ij}^{SO} + P^2Q_{ij} + P^2Q_{ij}^{SS} \right), \quad (2.13)$$

where D is the distance to source, and $\mu = \frac{m_1 m_2}{m_1 + m_2}$ is the binary's reduced mass. The term Q_{ij} corresponds to the leading-order Newtonian quadrupole moment, while the P^n terms represent PN corrections of order n. Spin contributions appear as spin-orbit (Q_{ij}^{SO}) and spin-spin (Q_{ij}^{SS}) terms. Explicit expressions for the terms in Eq.(2.13) and summarized in Appendix A.1.

A full characterization of the gravitational radiation emitted by a binary system requires an accurate description of its orbital motion. The presence of spin and the emission of gravitational waves lead to both precession of the orbital plane and a gradual inspiral of the binary. Within the adiabatic PN framework, it is assumed that these changes occur over timescales much longer than the orbital period, at least until the system approaches merger.

The binary's acceleration, which governs the evolution of its orbit, can be derived from the conservation of energy-momentum in a perturbed spacetime. When expressed in harmonic gauge, this yields the following form:

$$\mathbf{a} = \mathbf{a}_N + \mathbf{a}_{PN} + \mathbf{a}_{SO} + \mathbf{a}_{2PN} + \mathbf{a}_{SS} + \mathbf{a}_{RR}^{BT} + \mathbf{a}_{PNSO} + \mathbf{a}_{3PN} + \mathbf{a}_{RR1PN} + \mathbf{a}_{RRSO} + \mathbf{a}_{RRSS}, \quad (2.14)$$

where each component represents: Newtonian (N), post-Newtonian (PN), spin-orbit (SO), second PN (2PN), spin-spin (SS), and radiation-reaction (RR) contributions. Explicit expressions for these terms are provided in Appendix B.1.

2.1.3 Motion in the Center of Mass Frame

To simplify the analysis, we shift the coordinate system such that the origin coincides with the center of mass (CoM) of the binary. This is achieved by enforcing the condition that the binary's mass dipole moment vanishes, $I_i = 0$. Under this transformation, the positions of the individual components, \mathbf{y}_1 and \mathbf{y}_2 , can be expressed in terms of the relative separation vector $\mathbf{x} \equiv \mathbf{y}_1 - \mathbf{y}_2$ and the relative velocity $\mathbf{v} \equiv \mathbf{v}_1 - \mathbf{v}_2 = d\mathbf{x}/dt$. We denote the magnitude of the orbital separation as $r \equiv |\mathbf{x}|$, and introduce the unit vector $\mathbf{n} = \mathbf{x}/r$. Then radial component of the relative velocity is $\dot{r} = \mathbf{n} \cdot \mathbf{v}$.

The relevant mass parameters include:

• The binary's total mass $m = m_1 + m_2$,

- The reduced mass $\mu = \frac{m_1 m_2}{m}$,
- The mass difference ratio $\Delta = \frac{m_1 m_2}{m}$,
- The symmetric mass ratio

$$\nu = \frac{\mu}{m} = \frac{m_1 m_2}{(m_1 + m_2)^2}, \qquad (2.15)$$

This symmetric mass ratio, ν , varies between [0,0.25] taking its maximum for equal-mass systems and becomes negligible in the limit when one body is much smaller than the other. Thus ν is numerically small and can be seen as a small expansion parameter. We also define the dimensionless mass fractions $X_1 = m_1/m$ and $X_2 = m_2/m$, such that $\Delta = X_1 - X_2$ and $\nu = X_1X_2$. Within the CoM frame, the general expressions for the individual positions of the two bodies are given by:

$$\mathbf{y}_1 = \left[X_2 + \nu \,\Delta \,\mathcal{P} \right] \mathbf{x} + \nu \,\Delta \,\mathbf{Q} \,\mathbf{v} \,, \tag{2.16a}$$

$$\mathbf{y}_2 = \left[-X_1 + \nu \,\Delta \mathcal{P} \right] \mathbf{x} + \nu \,\Delta \, \mathbf{Q} \, \mathbf{v} \,, \tag{2.16b}$$

Here, corrections beyond the Newtonian level within the PN framework scale with ν and Δ . Naturally, for the equal mass case, the positions satisfy $\mathbf{y}_1 = -\mathbf{y}_2$. The dimensionless coefficients \mathcal{P} and \mathbf{Q} , which characterize the radiation-reaction terms, take the following form when expanded up to the 3.5PN order: [Note: Any PN coefficient not explicitly listed is assumed to be zero, all equations are in powers of $1/c^{2n}$ where n is the order of PN] (Blanchet, 2014).

$$\mathcal{P}_{1PN} = \frac{v^{2}}{2} - \frac{Gm}{2r}, \qquad (2.17a)$$

$$\mathcal{P}_{2PN} = \frac{3v^{4}}{8} - \frac{3vv^{4}}{2} + \frac{Gm}{r} \left(-\frac{\dot{r}^{2}}{8} + \frac{3\dot{r}^{2}v}{4} + \frac{19v^{2}}{8} + \frac{3vv^{2}}{2} \right) + \frac{G^{2}m^{2}}{r^{2}} \left(\frac{7}{4} - \frac{v}{2} \right), \qquad (2.17b)$$

$$\mathcal{P}_{3PN} = \frac{5v^{6}}{16} - \frac{11vv^{6}}{4} + 6v^{2}v^{6} + \frac{Gm}{r} \left(\frac{\dot{r}^{4}}{16} - \frac{5\dot{r}^{4}v}{8} + \frac{21\dot{r}^{4}v^{2}}{16} - \frac{5\dot{r}^{2}v^{2}}{16} \right) + \frac{21\dot{r}^{2}v^{2}v^{2}}{16} - \frac{11\dot{r}^{2}v^{2}v^{2}}{2} + \frac{53v^{4}}{16} - 7vv^{4} - \frac{15v^{2}v^{4}}{2} \right) + \frac{G^{2}m^{2}}{r^{2}} \left(-\frac{7\dot{r}^{2}}{3} + \frac{73\dot{r}^{2}v}{8} + 4\dot{r}^{2}v^{2} + \frac{101v^{2}}{12} - \frac{33vv^{2}}{8} + 3v^{2}v^{2} \right) + \frac{G^{3}m^{3}}{r^{3}} \left(-\frac{14351}{1260} + \frac{v}{8} - \frac{v^{2}}{2} + \frac{22}{3}\ln\left(\frac{r}{r'_{0}}\right) \right), \qquad (2.17c)$$

$$\mathcal{P}_{3.5PN} = \frac{G^{2}m^{2}}{r^{2}}\dot{r} \left(-\frac{8\dot{r}^{2}}{5} - \frac{2v^{2}}{15} + \frac{68v^{2}v}{35} \right) + \frac{G^{3}m^{3}}{r^{3}}\dot{r} \left(\frac{52}{15} - \frac{116}{35}v \right) \qquad (2.17d)$$

and

$$Q_{2\text{PN}} = -\frac{7\,Gm\,\dot{r}}{4},\tag{2.18a}$$

$$Q_{2.5\text{PN}} = \frac{4 \, Gm \, v^2}{5} - \frac{8 \, G^2 m^2}{5 \, r},\tag{2.18b}$$

$$Q_{3\text{PN}} = Gm \,\dot{r} \left(\frac{5 \,\dot{r}^2}{12} - \frac{19 \,\dot{r}^2 \,v}{24} - \frac{15 \,v^2}{8} + \frac{21 \,v \,v^2}{4} \right) + \frac{G^2 m^2 \,\dot{r}}{r} \left(-\frac{235}{24} - \frac{21 \,v}{4} \right), \tag{2.18c}$$

$$Q_{3.5\text{PN}} = Gm \, v^4 \left(\frac{6}{7} - \frac{22 \, v}{7} \right) + \frac{G^2 m^2}{r} \left(\frac{44}{15} \dot{r}^2 + \frac{6}{35} v^2 + \frac{68}{35} \dot{r}^2 v + \frac{132}{35} v^2 v \right)$$

$$+\frac{G^3m^3}{r^2}\left(-\frac{172}{105} - \frac{64}{35}\nu\right). \tag{2.18d}$$

Velocities are determined by differentiating the positions derived above. Then, we begin by evaluating the relative acceleration $\mathbf{a} = \mathbf{a}_1 - \mathbf{a}_2$, and then implement the substitutions defined in Eq.(2.16). The instantaneous acceleration takes the general form: [the coefficients \mathcal{A} and \mathcal{B} are expressed in Appendix B.1]

$$\mathbf{a}_{\text{inst}} = -\frac{Gm}{r^2} \left[(1 + \mathcal{A}) \mathbf{n} + \mathcal{B} \mathbf{v} \right], \tag{2.19}$$

After determining optimal initial parameters CBWaves starts calculating these required quantities stated above. The outvars string defines the list of output variables written during the simulation. These include the simulation time t, the number of completed orbits and the components of the relative position vector (r_x, r_y, r_z) along with the positions of the individual compact objects (x_1, y_1, z_1) and (x_2, y_2, z_2) . These outputs provide comprehensive diagnostics of the binary's orbital evolution. We determine a best-fit curve for separation $r = \sqrt{r_x^2 + r_y^2 + r_z^2}$ and pass that function f(t) into the PLUTO code to update the system's orbital separation and the positions of individual black holes at each time step. This information is required to calculate the gravitational potential of the binary.

2.2 PLUTO code: Hydrodynamical equations

We construct our hydrodynamical model using the PLUTO code. The system consists of a BBH with component masses m_1 and m_2 , embedded in a localized region of an accretion disc surrounding a SMBH of mass M. To simplify the disc geometry, we adopt the local shearing box approximation (Fig 2.1), following the approach of Goldreich and Lynden-Bell (1965). This approximation replaces the global cylindrical structure of the disc with a local Cartesian coordinate system defined by unit vectors \hat{x} and \hat{y} . The center of mass (CoM) of the binary is placed at the origin, (x, y) = (0, 0), corresponding to a fiducial radius R from the SMBH. At this location, the disc exhibits a Keplerian orbital velocity $V_K = \sqrt{GM/R}$ and angular frequency

 $\Omega_K = V_K/R$. The simulation is performed in a rotating frame that moves with this Keplerian frequency. The setup closely follows the prescription outlined in Li and Lai (2022).

To model the dynamics of an inviscid, compressible fluid in two dimensions, we solve the standard equations of hydrodynamics in a rotating frame. The flow is governed by a γ -law equation of state, and the system is evolved using the following set of conservation laws:

$$\frac{\partial \rho}{\partial t} + \nabla \cdot (\rho \mathbf{u}) = 0, \tag{2.20}$$

$$\frac{\partial(\rho\mathbf{u})}{\partial t} + \nabla \cdot (\rho\mathbf{u}\mathbf{u} + P\mathbf{I}) = \rho \left(2\mathbf{u} \times \Omega_K + 2q_{\rm sh}\Omega_K^2 x - \nabla \phi_b\right),\tag{2.21}$$

$$\frac{\partial E}{\partial t} + \nabla \cdot [(E + P)\mathbf{u}] = \rho \,\mathbf{u} \cdot \left(2q_{\rm sh}\Omega_K^2 x - \nabla \phi_b\right),\tag{2.22}$$

where **u** is the velocity, ρ is gas density, P is pressure, E is total energy density and **I** is the identity matrix. Ω_K is aligned with \hat{z} , $q_{\rm sh} = -d \ln \Omega_K/d \ln R$ is the shear parameter (equal to 3/2 for a Keplerian disc), and ϕ_b is the gravitational potential of the binary. This potential is defined by

$$\phi_b(r_k) = -\frac{Gm_1}{\sqrt{(r_1 - r_k)^2 + \xi_g^2}} - \frac{Gm_2}{\sqrt{(r_2 - r_k)^2 + \xi_g^2}},$$
(2.23)

here r_1 and r_2 denote the positions of each binary component, r_k is the position of k^{th} cell inside the computational domain, and ξ_g is the gravitational softening length set as $0.01a_b$. We use an ideal equation of state $\gamma = 5/3$ and ignore self gravity of gas.

The binary's total mass $m_b = m_1 + m_2$ orbits the SMBH with separation a_b and eccentricity e_b . The mass ratio between the components is $q_b \equiv m_2/m_1 \le 1$. The angular momentum L_b , mean orbital frequency Ω_b and energy E_b are given by:

$$\Omega_b = \sqrt{\frac{Gm_b}{a_b^3}}, \quad L_b = \mu_b \Omega_b a_b^2 \sqrt{1 - e_b^2}, \quad E_b = -\frac{\mu_b Gm_b}{2a_b},$$
(2.24)

where $v_b = \sqrt{\frac{Gm_b}{a_b}}$ and $\mu_b = \frac{m_1m_2}{m_b}$ is the reduced mass. We consider both prograde (where $\hat{\Omega}_b \cdot \hat{z} = 1$) and retrograde ($\hat{\Omega}_b \cdot \hat{z} = -1$) orientations and keep the binaries co-planar with the disc.

2.3 Model Parameters

The following dimensionless parameters describe the simulation environment as in LL22:

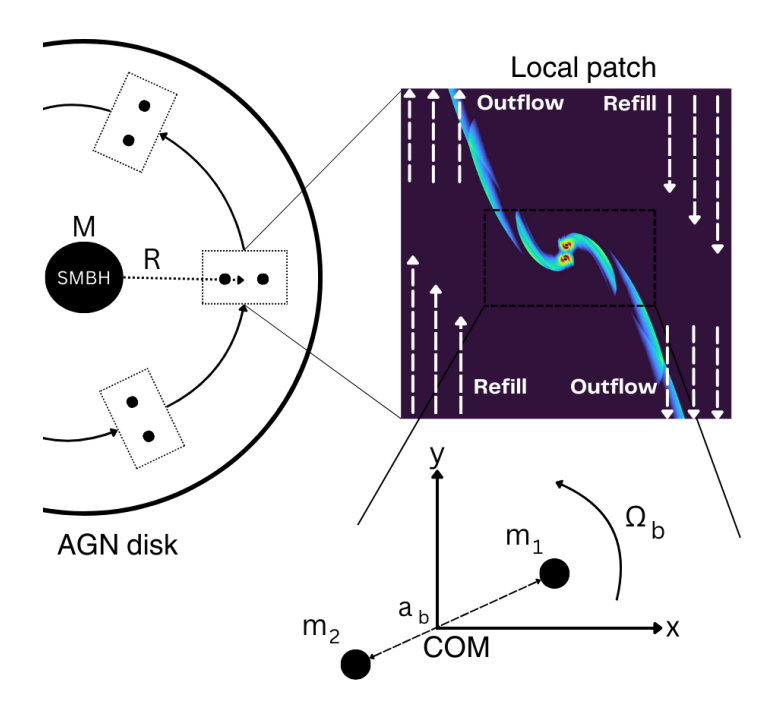


Figure 2.1: An illustration of the shearing box model, binary embedded in an AGN disc at distance R from a SMBH at the center, a_b is the binary separation.

1. Mass ratio of the binary to central SMBH:

$$q_{\rm M} = \frac{m_{\rm b}}{M}.\tag{2.25}$$

2. Disc aspect ratio h at disc radius R:

$$h = \frac{H_g}{R} = \frac{c_s}{V_K},\tag{2.26}$$

where H_g is the gas scale height and c_s is the sound speed.

3. The ratio of the binary Hill radius $R_H \approx R(m_b/M)^{1/3}$ to a_b :

$$\lambda = \frac{R_{\rm H}}{a_b} = \frac{R}{a_b} \left(\frac{m_b}{M}\right)^{1/3}.$$
 (2.27)

The Hill radius (or Roche radius) (R_H) is a measure of the region around an object where its gravitational influence dominates over that of a larger body it is orbiting. Outside this radius, the tidal forces from the larger central body exceed the gravitational binding forces of the smaller body. Here we use a slightly different way for defining the Hill radius, $R_H = R(m_b/M)^{1/3}$. R_H helps define the spatial scale where circumbinary structures (like minidiscs) form and evolve.

From the binary's point of view, the flow dynamics are governed by the following characteristic velocity ratios.

$$\frac{c_{s,\infty}}{v_b} = hq^{-1/3}\lambda^{-1/2},\tag{2.28}$$

$$\frac{\mathbf{V}_s}{\mathbf{v}_b} = q_{\rm sh} \frac{\Omega_K}{\Omega_b} = q_{\rm sh} \lambda^{-3/2},\tag{2.29}$$

where V_s represents the Keplerian shear magnitude over a distance of a_b . We set $q_{sh} = 3/2$ for the simulations. The time-independent background wind profile in the shearing box can be written as (Li and Lai, 2022):

$$\mathbf{V}_{\mathbf{w}} = -q_{\mathbf{sh}} \Omega_{\mathbf{K}} x \hat{\mathbf{y}} \tag{2.30}$$

2.4 Simulation Parameters

We fix $q_M = 10^{-6}$, h = 0.01 and $\lambda = 2.5$ for different simulation runs. The root domain is set to a large size to ensure that the outer boundaries are sufficiently distant, allowing the binary to only influence the wind profile in the immediate vicinity. Such a large domain helps maintain the shearing box approximation very well.

For $q_M = 10^{-6}$, h = 0.01, and $\lambda = 2.5$, we can compute the velocity ratios:

$$\frac{c_{s,\infty}}{v_b} = 0.01 \times (10^{-6})^{-1/3} \times (2.5)^{-1/2} = 0.633,$$
(2.31)

$$\frac{V_s}{v_b} = \frac{3}{2} \times (2.5)^{-3/2} = 0.380,$$
 (2.32)

To make our simulations stable we use van Leer integrator (van Leer, 1979) along with the Harten, Lax and van Leer (HLL) Riemann solver (Harten et al., 1983). We use Runge-Kutta 2nd order time stepping method (RK2) with linear spatial reconstruction. We use a nested grid to resolve the flow in the vicinity of the binary. The code units are set to the natural units of the binary system. i.e. a_b , v_b and Ω_b^{-1} . The detailed results are listed in Table 3.1 and the physical scale units are given in Table 3.2.

2.5 Boundary Conditions

The boundary conditions used in the simulations affect the overall flow structure and are necessary to ensure the robustness of the shearing box model. The x-boundary is kept open for outflow and the y-boundaries are defined in the following way:

$$y_{\max} = \begin{cases} \text{refill}, & \text{if } 0 \le x \le 0 \\ \text{outflow}, & \text{if } x > 0 \end{cases}, \quad y_{\min} = \begin{cases} \text{outflow}, & \text{if } x \ge 0 \\ \text{refill}, & \text{if } x < 0 \end{cases}.$$

Refilling is implemented by assigning ghost cells the properties of the ambient medium to ensure a smooth continuation of the background flow. In regions exhibiting outflow, ghost cells are assigned the values from the domain edge. Along the *x*-direction, no refilling is applied due to viscous timescales being significantly longer to the total simulation duration. In contrast, the *y*-direction employs asymmetric boundary conditions: downstream boundaries are treated with outflow conditions, while upstream boundaries are replenished with ambient gas. With these boundary conditions, wave damping along y boundaries is not needed.

2.6 Post-processing calculations

2.6.1 Torque and Accretion rate

We compute the rate of change of angular momentum from the binary to (or from) AGN disc and the accretion rate. We concentrate more on the gravitational torque as we find pressure torque to be negligible. We use a post-processing strategy that is comparable to that described in Muñoz et al. (2019). Our model treats each binary component as a circular sink with a sink radius r_s . Within this sink radius, we set the velocity to zero and assign small values to both pressure and density. At the end of each time step, we update the pressure, density, and velocity for the disc. The following equations are used to calculate the accretion rate and the force due to pressure and accretion.

$$\dot{M}_i = \oint (\rho \mathbf{u}) \cdot d\mathbf{A},\tag{2.33}$$

$$f_{\text{acc},i} = \frac{1}{M_i} \oint d\dot{M}_i (\boldsymbol{u} - \boldsymbol{v}_{i,SB})$$
 (2.34)

$$f_{\text{pres},i} = \frac{1}{M_i} \oint (-\mathbf{P}) \cdot d\mathbf{A}$$
 (2.35)

where $d\mathbf{A}$ is the area element about accretor done at an evaluation radius $r_e = r_s + \epsilon$, where $\epsilon > \sqrt{2\delta_f}$ and δ_f is the cell size at finest resolution ~ 0.01 . is The gravitational force on each accretor is computed as:

$$\mathbf{f}_{\text{grav},i} = -\sum_{k} \frac{Gm_k(r_i - r_k)}{|r_i - r_k|^3},$$
(2.36)

where $m_k = \rho \delta^2$ is the mass of gas in cell k, and δ is the cell size at r_k .

The equation of motion for the binary components are then given by:

$$\mathcal{T}_b = \mathbf{r}_b \times (\mathbf{f}_1 - \mathbf{f}_2), \tag{2.37}$$

$$\dot{E}_b = -\frac{G\dot{M}_b}{|\mathbf{r}_b|} + \mathbf{v}_b \cdot (\mathbf{f}_1 - \mathbf{f}_2), \tag{2.38}$$

where \dot{M}_b is the time-averaged accretion rate. We compute each component of torque using Eq (2.37).

2.6.2 Minidisc Mass density

We place our binary system in the mid-plane of the AGN disc, and given the 2-D nature of our simulation we neglect the vertical gas profile of the AGN disc. To track the evolution of the gas bound to each black hole, we define the "minidisc" region as an annular shell surrounding each BH with radius $r \in [1.1r_s, 4.0r_s]$. Within this region, we compute the minidisc mass density per unit height via:

$$\frac{M_{\text{minidisc},i}}{H} = \int_{1.1r_s}^{4r_s} \rho \, dA,\tag{2.39}$$

where dA is the area element. This accounts for gas gravitationally bound but not yet accreted.

2.6.3 Mass sloshing

To quantify transfer or "sloshing" of mass between the minidiscs, we compute the net mass flux density across the mid-plane perpendicular to the binary axis. At each snapshot, the mid-plane is defined using the BH positions:

- 1. The midpoint (x_{mid}, y_{mid}) between the BHs is determined.
- 2. A unit normal to the line connecting the BHs is computed.
- 3. The velocity component normal to this midplane, $u_{\perp} = \mathbf{u} \cdot \hat{\mathbf{n}}$, is calculated.
- 4. The sloshing flux is obtained by summing ρu_{\perp} .

Mathematically, the sloshing mass flux density (per unit Area dA per unit time) is:

$$\Phi_{\text{slosh}} = \sum_{\text{midplane}} \rho \left(\mathbf{u} \cdot \hat{\mathbf{n}} \right), \tag{2.40}$$

where the normal is restricted to across a length ($\sim 0.5 a_b$). Sloshing is manifested due to asymmetries in $M_{\rm minidisc,1}$ and $M_{\rm minidisc,2}$ and can be associated with changes in torque balance and periodic oscillations in accretion rates. The sink positions (x_i, y_i, z_i) are tracked dynamically. This post-processing analysis framework allows us to quantify how angular momentum is redistributed in the binary-disc system, how mass is transferred and accreted, and how minidiscs evolve over time. Observing episodes of sloshing provides key insight into the short-term variability in the electromagnetic signatures of BBH systems.

CHAPTER 3

RESULTS

The main outcomes of our simulations are listed in Table 3.1. We present a detailed analysis of flow structure, torque, accretion, minidisc mass density and sloshing in sections 3.1, 3.2, 3.3, 3.4 and 3.5 respectively. We also present a case of retrograde orientation in section 3.6 and dependence of sink choice in section 3.7.

3.1 Flow Structure

The morphology of the gas flow surrounding BBHs is a crucial indicator of angular momentum transport and accretion processes. Figure 3.1 illustrates typical 2-D co-rotating streamlines in a shear flow. The flow is governed by a combination of large-scale shocks, rotational shear and dynamically evolving minidiscs. One of the most prominent features is the presence of grand spiral arms, large shock fronts that originate from the binary and extend towards the $\pm y$ boundaries along the direction set by the background shear flow.

Physically, these spirals are half bow shocks generated by the binary's supersonic motion relative to the surrounding gas in the co-rotating frame. In the middle panel of Figure 3.3, we also plot the contour lines of the sonic Mach number, defined as $\mathcal{M} = v/c_s$ where v is the local flow velocity to highlight the transitions between different flow regimes. We have plotted the contours for $\mathcal{M}=1$ with white lines, which separate supersonic and subsonic flows, highlighting the locations of shock transitions. The accreting gas undergoes a shock transition before being captured into CSDs around individual black holes. This transition is critical for regulating the mass accretion process, as the shocks dissipate kinetic energy and allow the gas to settle into bound orbits around the black holes These high Mach number flows result in sharp shock fronts and enhanced compression near the compression near the black holes. In lower mass ratio binaries this lead to more variable accretion patterns and a suppression of the secondary's minidisc extent.

Alongside the spirals the flow exhibits a horseshoe flow or co-orbital flow. These horseshoe flows are bound by the inner and outer shear flows (also called disc flows), similar to those seen in circumstellar or circumplanetary discs (Fung et al., 2015; Ormel, 2013). However, in BBH

systems, these flows are more variable and asymmetric especially in cases of non unity mass ratios. Horseshoe flow emerges where the gas parcels have nearly the same angular velocity as the binary. The gravitational potential near the binary induces streamlines that undergo a reversal near the L4 & L5 Lagrange points (see Lagrange points).

Closer to each black hole, compact CSDs form. Each CSD has its own smaller shocks which drive inflow and redistribute the angular momentum within it. These evolve continuously, responding to both gas infall and binary orbital motion. As the BHs are non-spinning, they are tidally locked. The part of CSD facing towards the other BH experiences tidal forces and is observed to be bulged. The outer edges of the CSDs are enveloped by localized bow shocks which act as launch points for outgoing streams. These streams are periodically flung outward and merge with the grand spiral once every orbit, creating a slingshot-like mechanism that recycles disc material and transports angular momentum. As the Hill spheres of these BHs are filled, the excess gas becomes partially unbound and forms a sloshing pulse, carrying a significant portion of the angular momentum and energy of the outer CSD of one BH across the L1 Lagrange point to the other BH, also consistent with Avara et al. (2024).

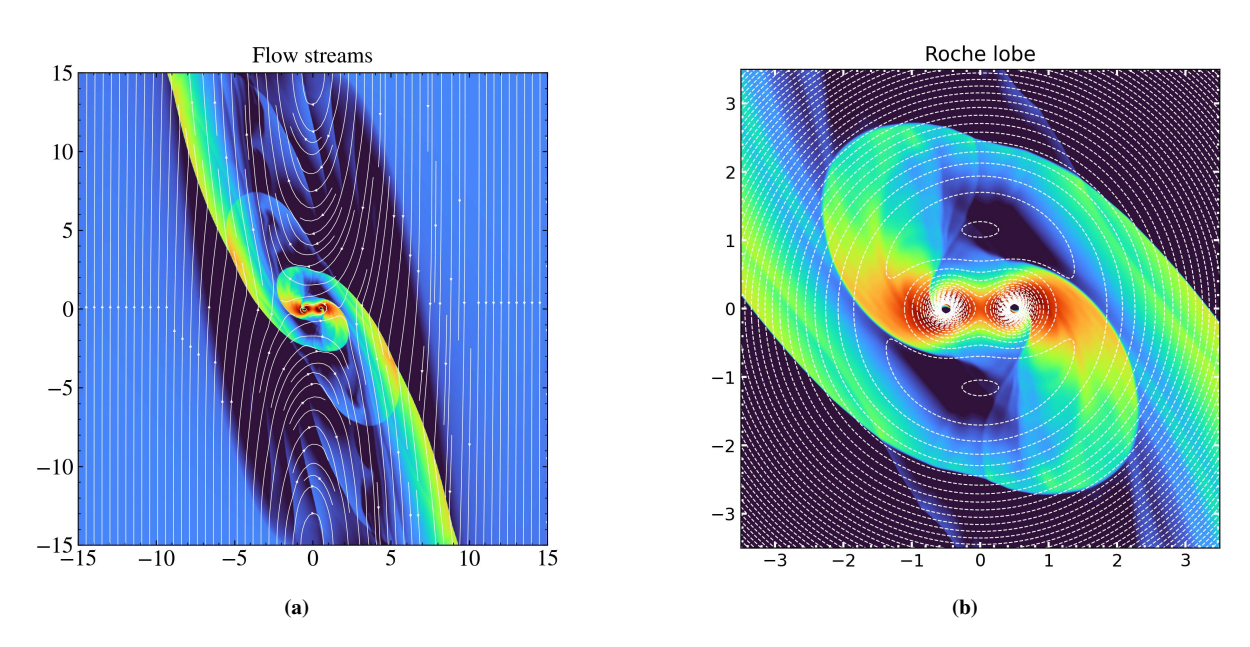


Figure 3.1: (a): Velocity streamlines for a equal mass fixed binary overlaid on the gas density distribution. The arrows denote gas velocity vectors in the orbital plane. The spiral arms act as conduits for angular momentum transport and the flow morphology exhibits balanced stream accretion onto both black holes. The circular streaming near each component indicates the presence of rotationally supported minidiscs. (b): Roche lobe contour lines for equal mass binary.

Velocity streams are visible entering the binary CBD opposite spiral shaped outflow lanes in Fig 3.1. These streams exhibit gradual deflection and acceleration as they approach each BH, forming curved trajectories that wrap into the CSDs. The flow structure indicates a quasi-steady balance between angular momentum removal via shocks and replenishment through large scale inflow at the boundaries. This behaviour confirms earlier results from LL22.

In unequal mass binaries, the flow becomes increasingly asymmetric. The more massive

primary having a deeper potential, allows itself to host a stable longer lived CSD. This disc maintains a quasi-Keplerian structure and experiences minor perturbations from surrounding shocks. The secondary forms a more tenuous and irregular CSD. These asymmetries arise due to the imbalance in the gravitational potential of the two components. We also observe that fixed and inspiral binary configurations exhibit qualitatively distinct flow topologies. In fixed orbit simulations, where the binary separation remains fixed, the flow gradually reaches a quasi state. In contrast, in inspiralling binaries, as the separation decreases, the spiral shocks become increasingly compressed and nonlinear, leading to concentrated inflow and transient enhancements in accretion. The inspiral process leads to non-steady-state behavior: CSDs undergo cycles of mass loading and unloading, the spiral arms become more tightly wound, and gravitational torques become more intense.

These findings demonstrate how inspiral accelerates the interaction between the disc and binary, enhancing the angular momentum exchange and triggering burst accretion episodes, which we discuss in section 3.3.

3.2 Gravitational Torque

The gravitational torque, \mathcal{T}_{grav} , exerted by the surrounding gas on a binary system embedded in an accretion flow plays a pivotal role in dictating its orbital evolution. The gravitational torque acting on the binary arises from local overdensities, spiral shocks, and non-axisymmetric flows generated by the interaction of the binary with the surrounding gas. Unlike cavity-forming systems, the torque is mediated primarily through dynamical friction, shock-driven density wakes, and stream-fed minidisc interactions. We analyze the time-evolved torque profiles for binaries of varying mass ratios, under both fixed-separation and inspiralling configurations. Each profile is decomposed into a full time-series and a selected zoom-in window to show both long-term trends and short-term variability (see Fig 3.3). The torque is normalized in units of $\rho v_b^2 a_b^2$. The corresponding values of average torque magnitudes are listed in Table 3.1. We consider the dominant torque term is only gravitational (Muñoz et al., 2019, 2020), computed as given in chapter 2.

Across all mass ratios, the torque shows strong periodic variability tied to the binary orbital phase. For equal-mass binaries, the torque is relatively symmetric and weakly negative on average, with low amplitude fluctuations. As the mass ratio decreases, the torque becomes increasingly asymmetric and chaotic. These patterns agree with LL22.

inspiralling binaries show enhanced torque variability compared to fixed binaries, but not always a more negative net torque. In some cases, orbital decay causes a redistribution of gas flows that reduces the long-term torque efficiency. Nonetheless, the average torque remains negative in all runs, indicating sustained angular momentum loss and orbital hardening over time.

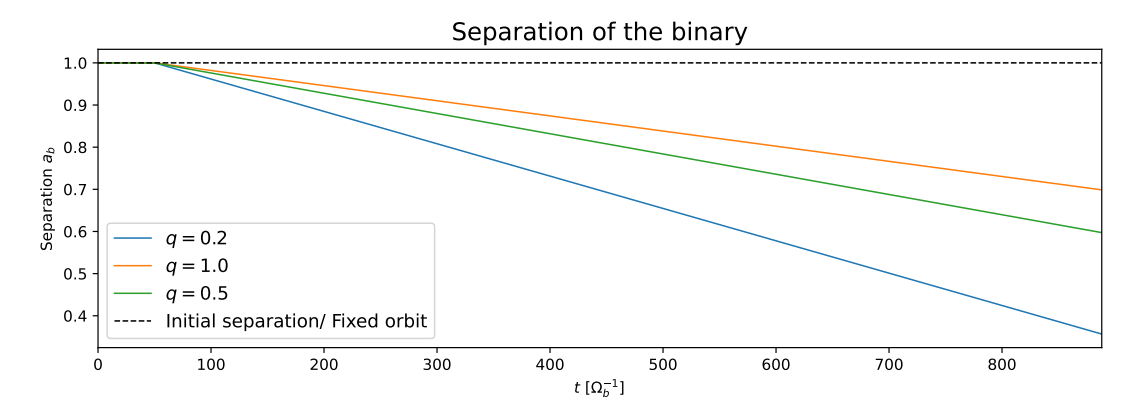


Figure 3.2: Plot shows the orbital separation decay with time for different mass ratios. For fixed binaries, the separation is kept as $a_b = 1$ (black dashed line).

The location of strongest torque deposition typically occurs near the binary separation, where spiral shocks intersect with the ambient disc. Overall, our simulations confirm that embedded binaries experience significant torque-driven evolution, with mass ratio and inspiral dynamics playing a central role in modulating both the amplitude and sign of angular momentum transfer.

Fig 3.2 illustrates the orbital separation evolution of binary black holes with different mass ratios over time. Initially set at a fixed value, the separations for inspiralling binaries begin to decrease due to gravitational torques. Notably, binaries with smaller mass ratios (e.g., q = 0.2) exhibit faster orbital decay, consistent with enhanced accretion asymmetries and stronger torques. In contrast, the q = 1.0 system maintains a comparatively larger separation over the same period, highlighting the role of mass ratio in regulating inspiral efficiency. This differential evolution underscores the sensitivity of binary hardening to the hydrodynamic response of the AGN disc.

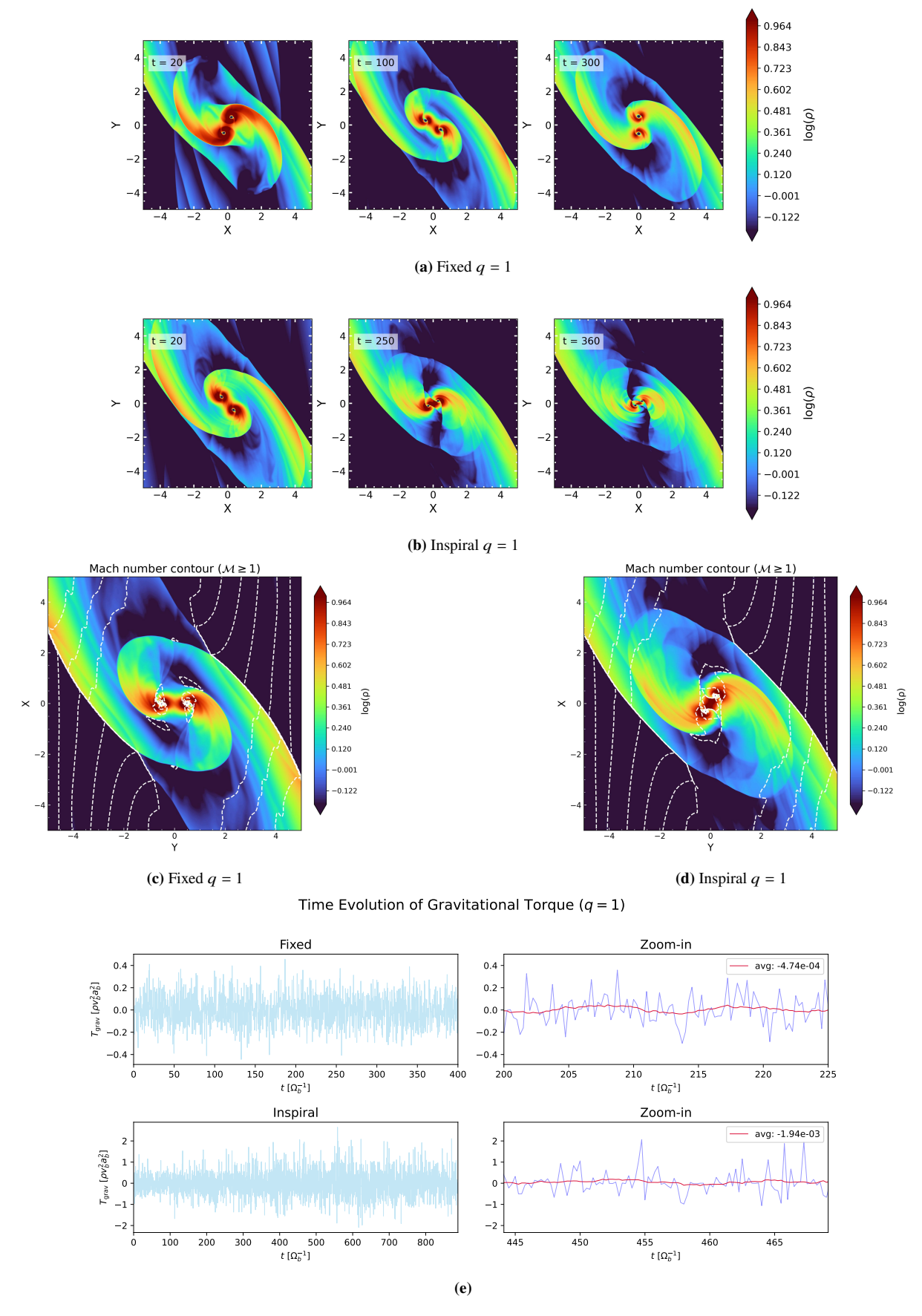


Figure 3.3: (a)-(b):Density distribution for q=1 binary with fixed and inspiral orbits at different times,respectively. (c)-(d): White dashed Mach number $\mathcal{M} \geq 1$ contour lines to show supersonic flow and shock transitions for fixed and inspiral binaries. (e): Time series for net Torque imparted onto the binary with a zoomed in region to show variability.

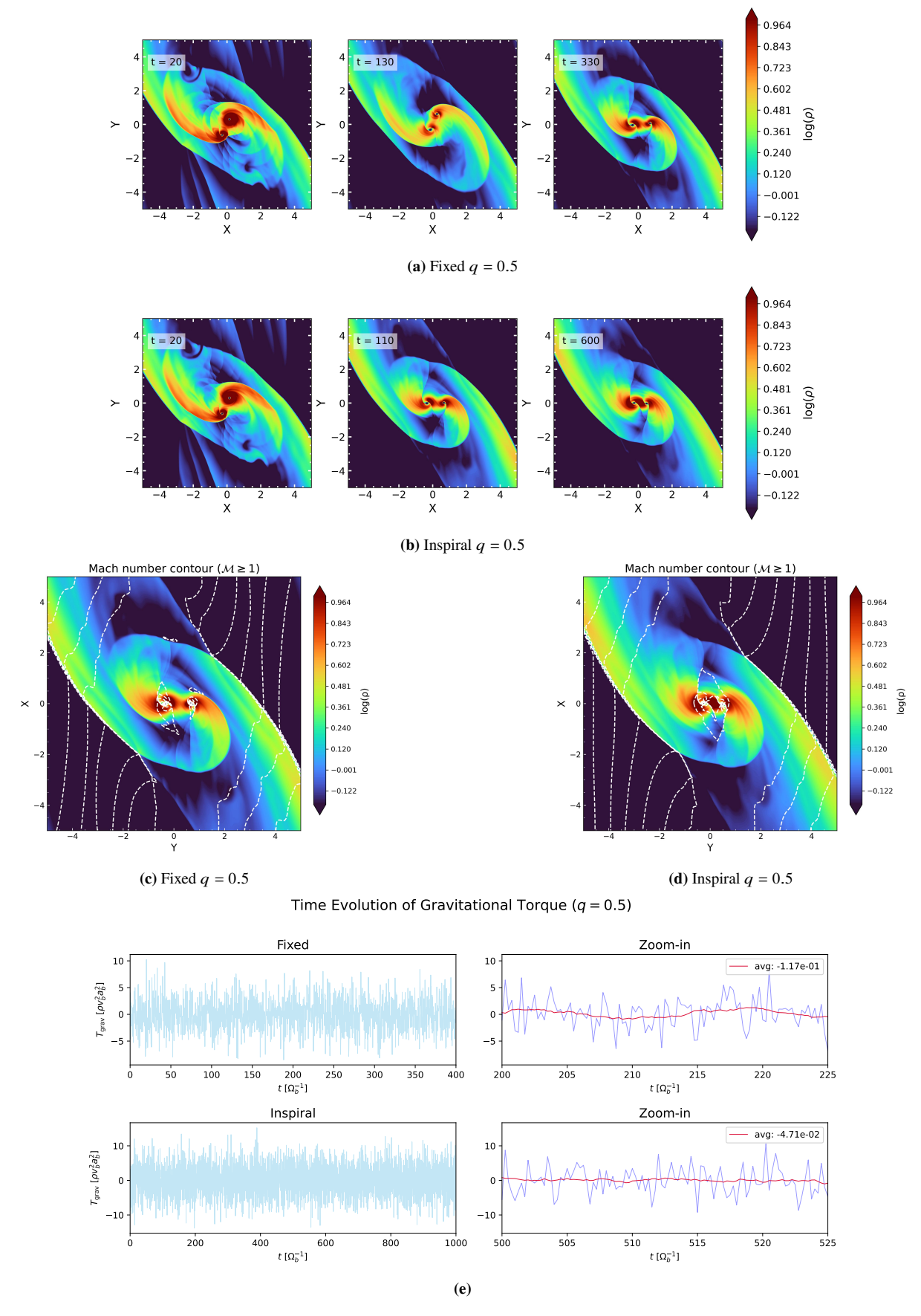


Figure 3.4: (a)-(b):Density distribution for q=0.5 binary with fixed and inspiral orbits at different times,respectively. (c)-(d): White dashed Mach number $\mathcal{M} \geq 1$ contour lines to show supersonic flow and shock transitions for fixed and inspiral binaries. (e): Time series for net Torque imparted onto the binary with a zoomed in region to show variability.

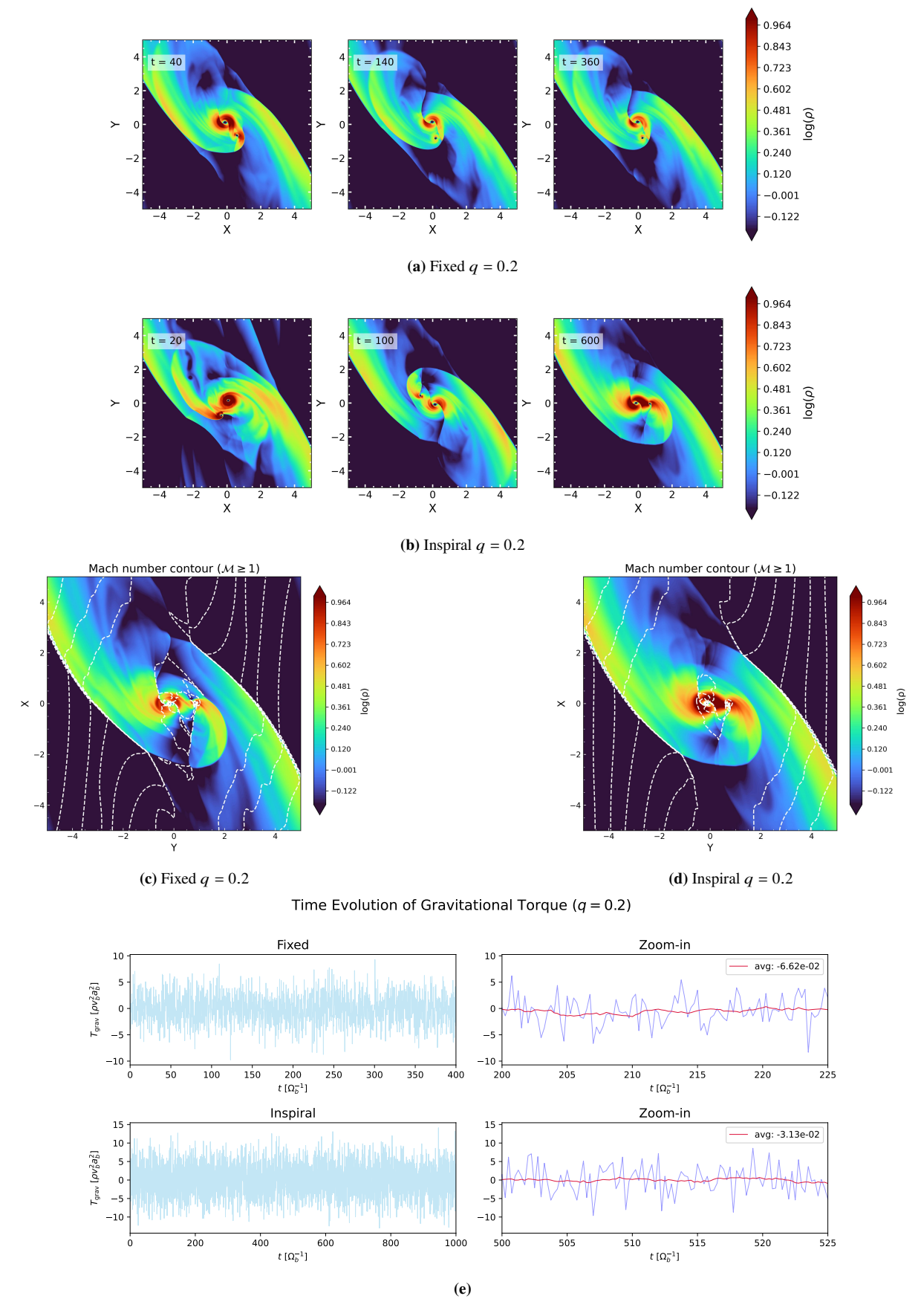


Figure 3.5: (a)-(b):Density distribution for q=0.2 binary with fixed and inspiral orbits at different times,respectively. (c)-(d): White dashed Mach number $\mathcal{M} \geq 1$ contour lines to show supersonic flow and shock transitions for fixed and inspiral binaries. (e): Time series for net Torque imparted onto the binary with a zoomed in region to show variability.

3.3 Accretion Variability

Accretion onto individual black holes in a binary system is a dynamic process governed by the interplay between gravitational torques and the binary's orbital motion. In our simulations, the accretion rate onto each component is tracked using an evaluation radius $r_e = 1.2 \times r_s$ around each black hole. The time series (see Fig. 3.6) behaviour exhibits prominent variability across all configurations, modulated on the binary's orbital time period and influenced by both mass ratio and orbital evolution mode (fixed or inspiral).

In a rotating frame comoving with the binary, the ambient gas experiences a non-inertial force environment including the coriolis, centrifugal and binary gravitational potentials as given in equation (2.21). This produces a low-density region around the binary, see Fig. 3.3. Material enters this lower dense region through the shear streams, feeding the CSDs surrounding each black hole. These streams are periodically modulated due to the binary's motion, leading to alternating accretion episodes onto each component. Across all mass ratios explored, we observe preferential accretion for the secondary, a trend that becomes more pronounced as q decreases. This phenomenon has been reported in prior studies (Farris et al., 2014; Muñoz et al., 2019; Li et al., 2021; Duffell et al., 2020) and is attributed to the secondary's greater proximity to the shear flow. For unequal mass binaries, the centre of mass is displaced toward the primary and the secondary orbits closer to the shear flow. It encounters denser inflow regions and is more effective at intercepting material from the accretion streams. The resulting accretion asymmetry not only affects minidisc structure but also may alter the long-term mass ratio evolution. Accreted material initially enters rotationally supported minidiscs which act as transient mass reservoirs, especially in high-q binaries. These discs exhibit internal shock dissipation and spiral wave modes that regulate angular momentum loss and mediate inflow to the event horizon scale. When mass piles up in one disc, pressure gradients and tidal forces can drive material across the binary axis, a process we identify as sloshing (see 3.5). Such events are often preceded or followed by sharp accretion bursts.

Figure 3.6 presents the time series of normalized accretion rates $[\rho v_b a_b]$ onto each black hole for both fixed and inspiral runs across the three mass ratios. In fixed-separation binaries, the accretion variability is quasi-periodic and closely tied to orbital phase. The streams settle into a steady pattern where the accretion alternates between the two components on a timescale of $\sim \Omega_b^{-1}/2$ i.e when the binary is at a π phase (aligned on X-axis).

For the equal mass binary, accretion is nearly symmetric throughout the evolution. In both fixed and inspiral cases, the accretion rates onto the two black holes remain balanced over time. The inspiral phase leads to a significant increase in accreted mass. As the mass ratio decreases to q=0.5, asymmetries in accretion emerge. In the fixed binary, the secondary black hole accretes nearly twice as much as the primary $(\dot{m}_2/\dot{m}_1 \sim 1.76)$. However, during inspiral, this asymmetry vanishes, both black holes accrete equally. This suggests that the dynamic orbital

Table 3.1: Simulation details and results

| Run | q | r_s $[a_b]$ | $L_x \times L_y \\ [a_b^2]$ | $\langle \mathcal{T}_{\text{grav}} \rangle \\ [\rho v_b^2 a_b^2]$ | $\dot{M} \ [ho v_b a_b]$ | $m_{ m disc,1} \ [ho a_b^2]$ | $m_{\mathrm{disc,2}} \ [\rho a_b^2]$ | Slosh rate $[\dot{M}/a_b]$ | Remarks | |
|----------------------|----------------|---------------|-----------------------------|---|---------------------------|-------------------------------|--------------------------------------|----------------------------|----------------|--|
| | Fixed binaries | | | | | | | | | |
| 1-Fixed | 1.0 | 0.04 | 20 × 20 | -4.47×10^{-4} | 1.38×10^{-3} | 2.88×10^{-3} | 2.88×10^{-3} | 1.93×10^{-14} | Fiducial run | |
| | 0.5 | 0.04 | 15×15 | -1.17×10^{-1} | 3.20×10^{-3} | 8.42×10^{-3} | 7.46×10^{-3} | -2.39×10^{-5} | _ | |
| | 0.2 | 0.04 | 15×15 | -6.62×10^{-2} | 3.68×10^{-3} | 5.98×10^{-3} | 4.66×10^{-3} | -2.68×10^{-4} | _ | |
| Inspiral binaries | | | | | | | | | | |
| 2-Inspiral | 1.0 | 0.04 | 15 × 15 | -1.94×10^{-3} | 8.90×10^{-1} | 4.03×10^{-3} | 4.03×10^{-3} | 1.12×10^{-5} | _ | |
| | 0.5 | 0.04 | 15×15 | -4.71×10^{-2} | 1.182×10^{0} | 6.05×10^{-3} | 5.84×10^{-3} | -1.47×10^{-4} | _ | |
| | 0.2 | 0.04 | 15×15 | -3.13×10^{-2} | 1.181×10^{0} | 8.12×10^{-3} | 5.45×10^{-3} | -2.05×10^{-4} | _ | |
| Retrograde and sinks | | | | | | | | | | |
| 1-Retrograde | 1.0 | 0.04 | 15 × 15 | -7.25×10^{-1} | 5.64×10^{-3} | _ | _ | -5.31×10^{-3} | Quickest decay | |
| 3-Sinks | 1.0 | 0.02 | 12×12 | -4.22×10^{-2} | 2.80×10^{-2} | 7.58×10^{-3} | 7.62×10^{-3} | -1.60×10^{-13} | _ | |
| | 1.0 | 0.08 | 12 × 12 | -1.97×10^{-5} | 1.49×10^{-4} | 1.60×10^{-3} | 1.60×10^{-3} | -1.10×10^{-14} | | |

Run indicates the simulation identifier; \mathbf{q} is the binary mass ratio; $\mathbf{r_s}$ is the sink radius; $\mathbf{L_x} \times \mathbf{L_y}$ is the computational domain size; $\mathcal{T}_{\text{grav}}$ is the net average gravitational torque; \mathbf{M} is the mass accretion rate; $\mathbf{m}_{\text{disc},1}$ and $\mathbf{m}_{\text{disc},2}$ are the masses of the individual minidiscs; Slosh rate represents the slosh mass flux rate per unit length; and Remarks provide additional notes. All quantities are time-averaged over the quasi-steady phase (over the last $\sim 300\Omega_b^{-1}$). All lengths are expressed in units of binary separation (a_b) and corresponding units are given under the quantities.

decay redistributes inflow trajectories and streamlines, allowing the primary better access to gas and restoring accretion balance.

The asymmetry is most extreme for q=0.2, where the fixed binary shows a strong preference for secondary accretion $(\dot{m}_2/\dot{m}_1 \sim 4.2)$. Even here, the inspiralling binary achieves symmetric accretion, indicating that orbital evolution has a regulating effect.

3.4 Minidisc Mass Evolution

Each black hole in a binary embedded within a gaseous environment may develop its own bound, rotationally supported gas structure, we have already defined as a minidisc or circumsingle disc. These minidiscs serve as transient reservoirs that mediate gas inflow to the black hole event horizon scale. In this section, we analyze the minidisc mass evolution using the integrated surface density within a circular region of radius $r_{\rm disc} = 4 \times r_s$ around each black hole.

Gas streams entering the binary through Lagrange points L2 and L3 become gravitationally captured by the individual black holes. If the incoming gas possesses sufficient angular momentum, it circularizes and forms a quasi-Keplerian disc around the black hole. These minidiscs are subject to intense shock heating at their outer boundaries, where high-velocity gas streams from the circumbinary disc collide with the disc material. It has been previously noted (Bowen et al., 2017, 2018, 2019; Combi et al., 2022) that the time fluid elements spend in a minidisc is comparable to or shorter than a binary orbital period. Each disc processes incoming material, redistributing angular momentum and feeding the black hole via inward drift. The

Table 3.2: Physical units for the simulations

| Parameter | Mass ratio | Value (code units) | Normalization (Physical Units) |
|--------------------------------------|------------|--------------------|---|
| Separation length (a_b) | q = 1 | 1 | $1.48 \times 10^8 \text{ m}$ |
| | q = 0.5 | 1 | $2.21 \times 10^8 \text{ m}$ |
| | q = 0.2 | 1 | $1.77 \times 10^8 \text{ m}$ |
| Time (Ω_h^{-1}) | | 1 | 0.474 yrs |
| Orbital period $(T = 2\pi/\Omega_b)$ | | 2π | 2.977 yrs |
| Velocity $(v_b = \Omega_b a_b)$ | q = 1 | 1 | $7.4 \times 10^{8} \text{ m/yr}$ |
| | q = 0.5 | 1 | $1.105 \times 10^8 \text{ m/yr}$ |
| | q = 0.2 | 1 | $8.805 \times 10^8 \text{ m/yr}$ |
| Surface Density (ρ_0) | | 1 | $1.67 \times 10^{-10} \text{ g/cm}^2$ |
| Accretion rate (\dot{M}) | q = 1 | 1 | $3.85 \times 10^{-6} M_{\odot}/\text{yr}$ |
| | q = 0.5 | 1 | $8.62 \times 10^{-6} \ M_{\odot}/\text{yr}$ |
| | q = 0.2 | 1 | $5.45 \times 10^{-6} \ M_{\odot}/\text{yr}$ |
| Minidisc Mass $(m_{\rm disc})$ | q = 1 | 1 | $1.83 \times 10^{-1} \ M_{\odot}$ |
| | q = 0.5 | 1 | $4.48 \times 10^{-1} \ M_{\odot}$ |
| | q = 0.2 | 1 | $3.38 \times 10^{-1} \ M_{\odot}$ |

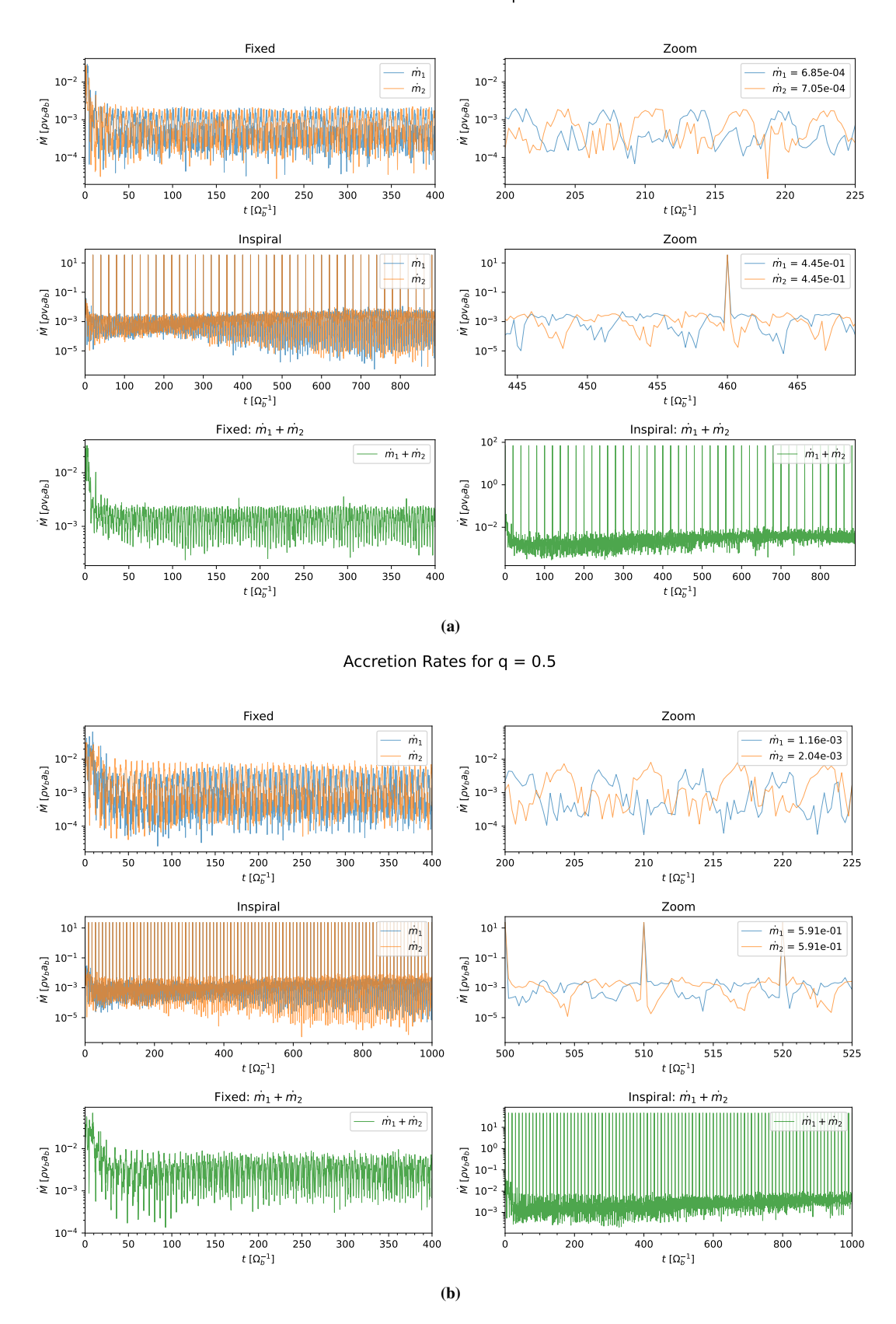
Normalization of code units to physical quantities for different binary mass ratios. All values assume $M_{\odot} = 1.989 \times 10^{33}$ g.

shock-dissipation and spiral wave modes within the discs result in episodic accretion bursts (Farris et al., 2014; Shi and Krolik, 2015). The structure and variability of these minidiscs are not static, they undergo cyclical states characterized by alternating phases of mass buildup and rapid depletion, in part due to the episodic nature of the gas supply, as described by Avara et al. (2024).

Across all mass ratios, our simulations reveal that minidisc mass is not simply a monotonic function of accretion rate. Instead, it exhibits a cyclical pattern, modulated on timescales comparable to the binary orbital period. For q=0.2 and q=0.5, the secondary minidisc undergoes particularly large swings in mass, oscillating between what can be termed "disc-dominated" and "stream-dominated" states. In the disc-dominated phase, the disc fills the Roche lobe with quasi-Keplerian material, exhibiting a relatively stable radial velocity structure and low net inflow. In this phase, newly arriving gas is efficiently circularized, and the minidisc acts as a temporary buffer against the central BH accretion.

In contrast, during the stream-dominated phase, the minidisc is depleted and incoming material bypasses orbit, plunging nearly radially inward with high velocities. This transition corresponds to bursts of accretion spikes. These phases reflect variations in the specific angular momentum of the supplied gas, much of it is delivered below the threshold needed for stable disc formation at the tidal truncation radius, as also shown in Avara et al. (2024) and Combi et al. (2022). As a result, only a fraction of the stream material forms a disc and the rest is promptly accreted, especially during the low-mass, stream-dominated state.

Accretion Rates for q = 1



For the equal-mass binary (see Fig. 3.7), the evolution of the minidisc masses is nearly identical across both black holes in both fixed and inspiral runs. This is expected due to the inherent symmetry of the system, both black holes orbit with the same velocity and have

Accretion Rates for q = 0.2

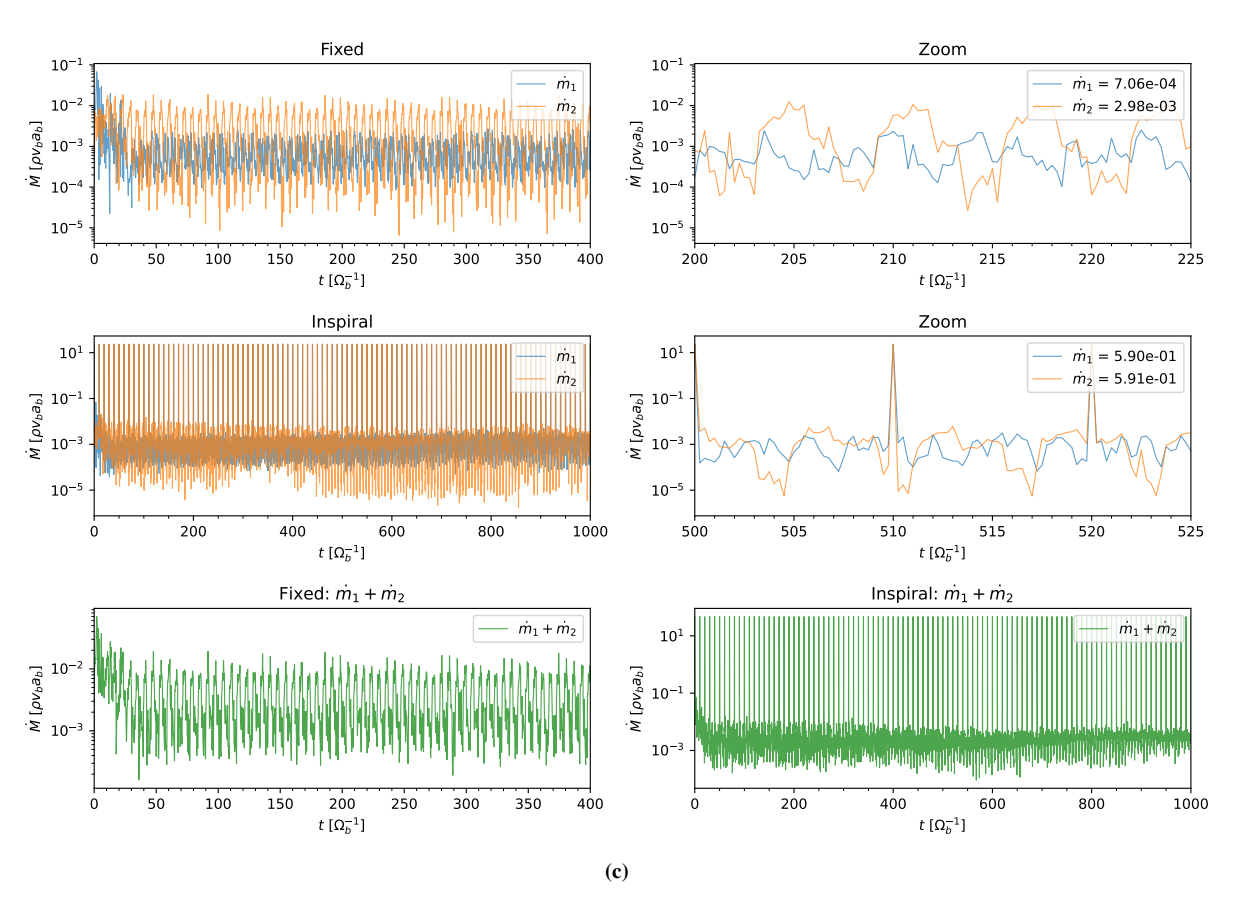


Figure 3.6: (a)-(c): Time series of accretion rates for both fixed and inspiral orbits with corresponding mass ratios. The blue line shows accretion rate for the primary and the orange line shows the accretion rate for the secondary. The green line shows the total accretion rate of the binary.

gravitational potential and interact with the background gas in a mirror-symmetric way. The inspiralling system leads to slightly higher minidisc masses due to increased inflow rates, but the symmetry in mass buildup remains intact. For q=0.2, the primary minidisc, though less favoured in direct inflow, often builds up a more massive and persistent disc due to lower accretion rates and greater angular momentum retention. Conversely, the secondary's minidisc fluctuates more violently, frequently being stripped or consumed. At q=0.5, the amplitude is reduced. The depletion of the secondary's minidisc can be attributed, in part, to ram pressure stripping.

Inspiral dynamics further affects this process. Inspiral also enhances radial velocity gradients in the disc, increasing shock dissipation near both BHs and promoting more uniform disc growth. We observe that inspiral leads to more uniform mass supply and suppresses long-term asymmetries, although short-term disc-stream cycling persists. This is consistent with the idea that inspiral drives stronger spiral shocks and stationary features within the minidiscs, rapidly redistributing angular momentum and leading to frequent structural reconfigurations (Ennoggi et al., 2025).

Minidisc evolution in AGN-embedded binaries is highly dynamic, featuring alternating states driven by angular momentum fluctuations, asymmetric inflow, and orbital motion. These cycles strongly influence the timing and efficiency of accretion and are a crucial component of the binary's secular evolution and observable variability.

CSD mass density for q = 1

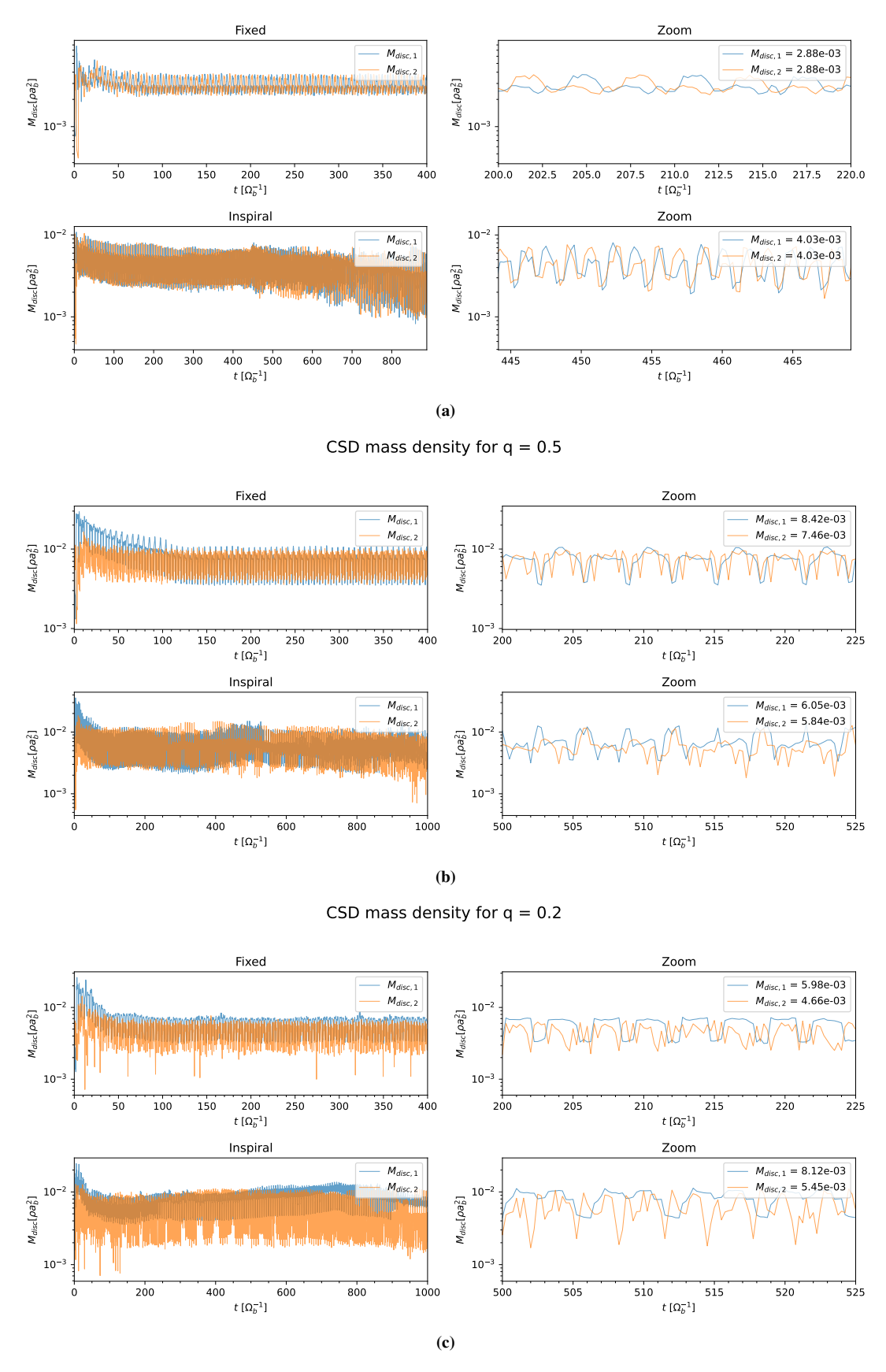


Figure 3.7: (a)-(c): Time series for Minidisc mass density for different mass ratios. The blue line shows minidisc mass density for the primary and the orange line shows the minidisc mass density for the secondary.

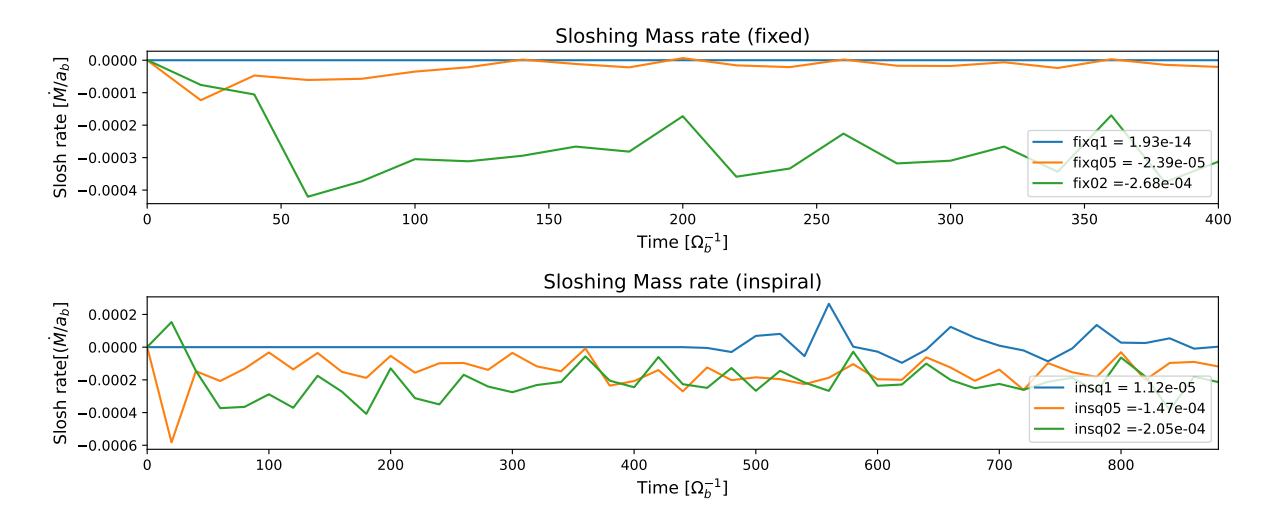


Figure 3.8: Comparison of slosh mass rate for different mass ratios and orbital prescriptions. The blue line, orange and green lines show the slosh ate for q = 1.0, 0.5, 0.2 respectively.

3.5 Sloshing

As mentioned before, mass sloshing refers to the lateral transfer of gas between the two minidiscs, typically along the binary axis perpendicular to the orbital velocity. Physically, mass sloshing acts as a dynamical equalizer, attempting to balance the distribution of gas between the two black holes. Importantly, sloshing contributes to the modulation of both minidisc mass and accretion rate and thus may be linked to short-timescale variability in electromagnetic emission. In observational terms, sloshing may manifest as oscillatory signatures in light curves or spectral line asymmetries (Noble et al., 2012; Ryan and MacFadyen, 2017; Bowen et al., 2017).

Figure 3.8 presents the time-averaged mass flux associated with sloshing between the two minidiscs, measured across a plane perpendicular to the binary axis. In the fixed binaries, net sloshing is negligible for the equal-mass case (q=1.0), something we expect with the symmetric flow structure. As the mass ratio decreases, the net sloshing flux becomes significantly more negative i.e towards to secondary. At q=0.5, the slosh rate settles to $\sim -2.4 \times 10^{-5} [\dot{M}/a_b]$, while for q=0.2, it reaches $\sim -2.7 \times 10^{-4} [\dot{M}/a_b]$. In the inspiralling binaries, sloshing persists but with notable differences. For q=1.0, the flux becomes slightly positive. At q=0.5 and q=0.2, the slosh rate remain negative. This reinforce our finding that while inspiral suppresses some of the long-term asymmetry, episodic mass transfer across the midplane continues to play a role in modulating the minidisc mass balance.

Notably, the sloshing flux in all runs is quasi-periodic, with sharper, more frequent pulses in lower q systems. This temporal structure is consistent with episodic overflow from one minidisc to another and correlates with known cycles of accretion variability. The amplitude of these pulses scales with mass ratio asymmetry, and their persistence during inspiral confirms that sloshing is an active feature throughout the binary's evolution.

3.6 Retrograde Equal-Mass Binaries

We now turn to the case of retrograde binaries, in which the orbital angular momentum vector of the binary is anti-aligned with that of the surrounding AGN disc $(\hat{\Omega}_b \cdot \hat{z} = -1)$. This configuration leads to fundamentally different accretion dynamics and torque behaviour compared to the prograde case, despite the global disc structure beyond the Hill radius remaining largely unaffected. As shown in Fig. 3.9, which presents density plotd at early and late times, the internal region within the Hill spheres undergoes drastic evolution. At early times (t = 20), transient circumsingle discs can be seen around each black hole, but these quickly dissolve as the simulation proceeds. By t = 400, the minidisc structures are completely disrupted, and the gas morphology becomes highly turbulent and incoherent. The absence of stable circumsingle discs results from frequent encounters with bow shocks launched by the companion BH and intensified ram pressure stripping caused by the high relative velocity between the binary and the disc.

This chaotic flow configuration leads to a highly irregular accretion pattern. Figure 3.9(d) shows the accretion rate time series for the retrograde binary. Unlike the quasi-periodic accretion observed in prograde cases, retrograde accretion is dominated by aperiodic bursts with no apparent correlation to orbital phase. The lack of disc-mediated mass storage leads to near-direct inflow from the background disc onto the black holes. This behavior is consistent with the finding that the relative velocity between the gas and the binary is significantly higher in the retrograde setup, enhancing accretion shocks and preventing the formation of rotationally supported structures. The increased inflow speed, combined with a lack of angular momentum buffering, results in higher time-averaged accretion rates than in prograde binaries, in agreement with results reported by LL22.

The gravitational torque acting is highly irregular, with large, stochastic oscillations and no dominant frequency or phase correlation. However, the torque converges to a strongly negative value, $\langle \mathcal{T}_{\text{grav}} \rangle \approx -0.725 \left[v_b^2 a_b \right]$, nearly twice the magnitude of the corresponding prograde binary. This stronger net torque arises from the enhanced gravitational drag exerted by the turbulent inflow and the lack of stable circumsingle discs to mediate angular momentum transfer. Consequently, the orbital hardening rate in the retrograde system is significantly higher, leading to faster inward migration and potentially earlier merger.

Another notable feature of the retrograde evolution is the transient formation of underdense regions near orbital phases $\pi/2$ and $3\pi/2$, corresponding to times when the binary is aligned along the y-axis. These phase-dependent cavities, visible in Fig. 3.9(b), are not present in the prograde case and appear to result from repeated shock clearing and orbital phase-dependent shear. Their presence suggests a temporary evacuation of gas around the BHs, which could lower the optical depth in these regions and facilitate the breakout of radiation or jets during late inspiral and merger.

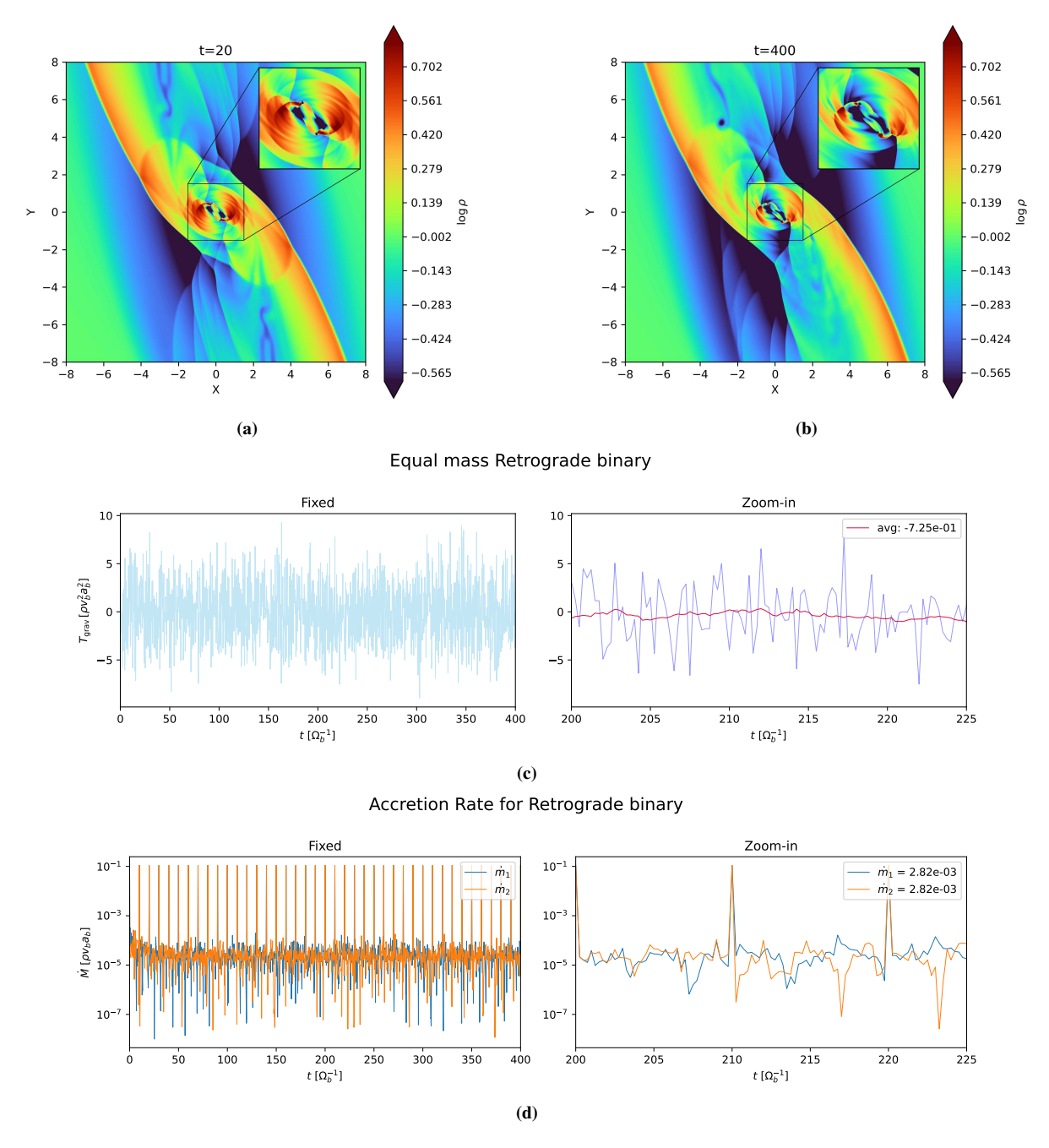


Figure 3.9: (a)-(b): Density plots for retrograde motion system. (c)-(d): Torque and Accretion time series respectively. The blue line shows accretion rate for the primary and the orange line shows the accretion rate for the secondary.

Overall, the retrograde configuration leads to stronger torque, faster accretion, suppression of minidisc formation and more chaotic dynamics within the Hill sphere. These features make retrograde binaries qualitatively distinct from their prograde counterparts, and their enhanced angular momentum loss rates may make them more efficient merger candidates.

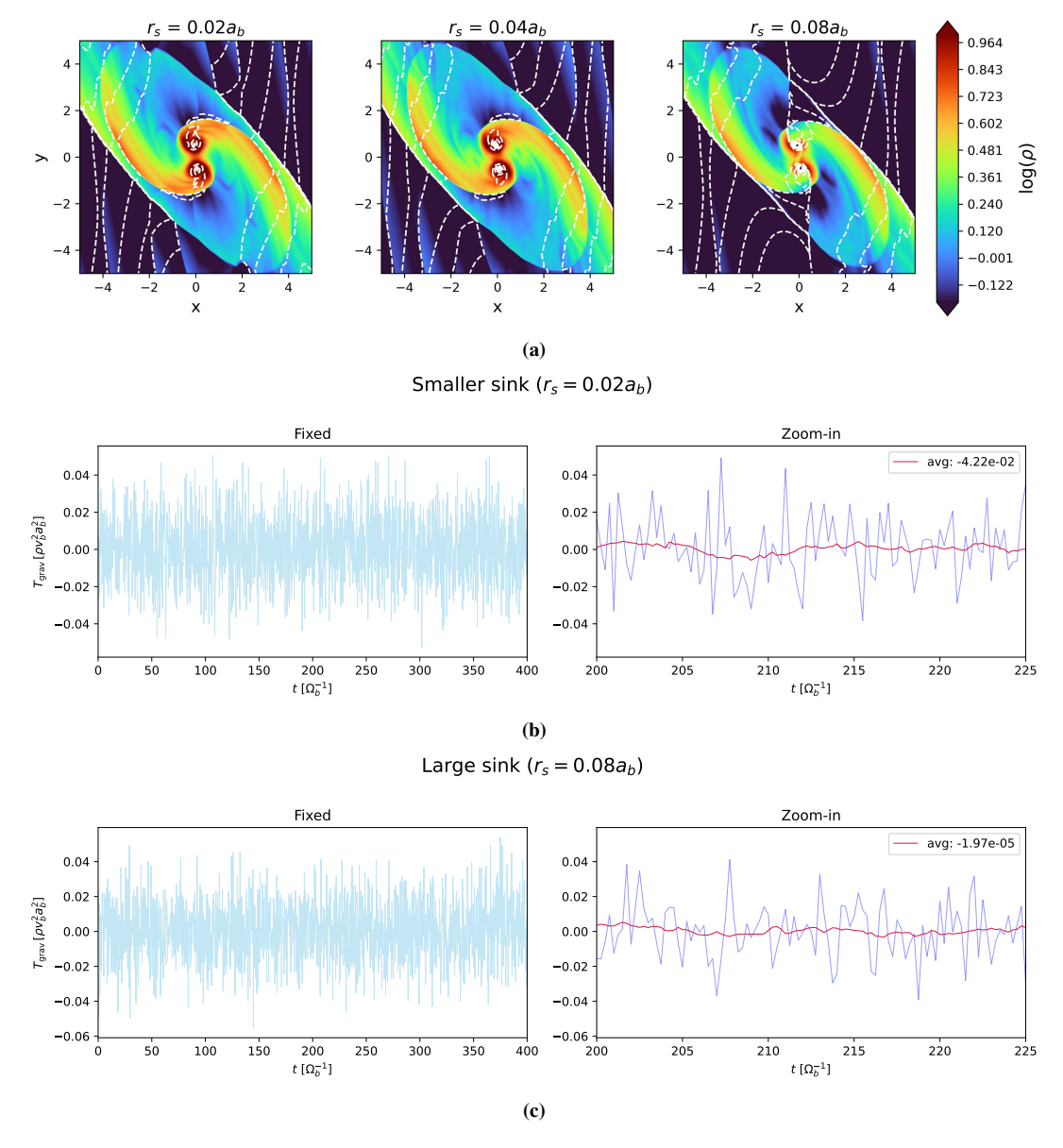


Figure 3.10: (a): Density with White dashed Mach number $M \ge 1$ contour lines to show supersonic flow and shock transitions and (b)-(c): Torque time series for sink radii $r_s = 0.02a_b$ and $0.08a_b$ respectively.

3.7 Dependence on sink radius

We verify that our orbital evolution results are robust across a range of numerical setups. Varying the evaluation radius, root domain size and finest resolution results in negligible changes ($\lesssim 2-3\%$) in the accretion rate. The choice of sink radius significantly influences the structure of the minidiscs and the resulting gravitational torques on the binary (see Fig 3.10. As the sink radius increases, the small-scale features within the minidiscs are progressively suppressed. This leads to a diminished ability of the gas to exert coherent torques on the binary. Simulations with larger sinks exhibit highly fluctuating but weak net torques, indicative of the loss of persistent non-axisymmetric structures. In contrast, smaller sinks preserve finer disc morphology, enabling sustained torque asymmetries that are essential for angular momentum

exchange between the binary and the surrounding disc. These results highlight the critical role of resolving the inner disc structure in capturing the correct gravitational interaction between the gas and the binary.

CHAPTER 4

SUMMARY

This study investigates the orbital dynamics and accretion properties of BBHs within AGN discs, environments. AGN discs, rich in gas and other baryonic material are unique environments for studying BBH evolution as they provide conditions that could lead to detectable EM counterparts to GW signals. Through high resolution simulations this study explores how the mass ratio and orbital orientation influence the dynamics of BBHs within these AGN discs.

We conducted simulations of BBH systems embedded in accretion flows within AGN discs, focusing on different configurations: prograde fixed orbit and inspiralling binaries, where the binary orbit aligns with the disc rotation and retrograde binaries, where the orbit is oppositely aligned. These simulations explored the impact of orbital alignment, mass ratio, on angular momentum exchange, accretion rates, minidiscs evolution and torque evolution. Key flow structures, accretion shocks, and angular momentum redistribution processes were analysed to understand how these binaries evolve over time and drive orbital contraction. To simulate this we employed the PLUTO code to model the evolution of binary black holes within a shearing box approximation of an AGN disc. We also prescibe inspiralling orbits where the separation between the BHs reduces as a function of time calculated from CBWaves using post-Newtonian expansion techniques. This combined approach enables accurate representation of both the gas dynamics surrounding the binary and the orbital evolution.

The simulations explore a parameter space spanning different mass ratios (q = 0.2, 0.5, 1.0). A key feature of the methodology is the use of combination of refill and outflow boundary conditions, hence we do not have to use wave damping. Some of the key findings are listed below.

4.1 Main Findings:

• Flow Structure and Angular Momentum Transport:

BBHs embedded in AGN discs generate prominent spiral arms and shock fronts, which serve as conduits for angular momentum transport. The flow morphology is highly sensitive to the mass ratio and orbital configuration. In prograde binaries, well-defined

minidiscs form around each black hole, and the system reaches a quasi-steady state with periodic accretion variability. The black holes are non-spinning and hence are tidally locked, the tidal forces create a bulge in the minidisc region facing the other black hole. In retrograde binaries, minidiscs are quickly disrupted due to high ram pressure stripping and the gas flow becomes turbulent and chaotic.

• Gravitational Torque and Orbital Evolution:

The surrounding gas exerts a net negative torque on the BBH, driving orbital decay and eventual merger. This torque is stronger and more variable in retrograde systems, leading to faster orbital hardening compared to prograde cases.

Accretion Variability and Minidisc Evolution:

Accretion onto each black hole is highly dynamic, modulated by the binary's orbital motion and the structure of the inflowing gas. Across all mass ratios, the secondary (less massive) black hole tends to accrete more efficiently, especially in unequal-mass binaries. This preferential accretion is attributed to the secondary's closer proximity to the ambient shear flow, allowing it to intercept more inflowing material. Minidisc masses fluctuate cyclically, alternating between "disc-dominated" (stable, rotationally supported) and "stream-dominated" (depleted, direct inflow) states. These cycles are linked to variations in the angular momentum of the accreted gas and can trigger bursts of accretion.

• Mass Sloshing:

The simulations reveal significant mass sloshing in unequal-mass binaries. This process acts as a dynamical equalizer, tending to redistribute mass and angular momentum between the components. The amplitude and frequency of sloshing events increase as the mass ratio decreases.

• Retrograde vs. Prograde Dynamics:

Retrograde binaries exhibit fundamentally different behaviour from prograde ones. The lack of stable minidiscs, increased turbulence and higher relative velocities between the binary and the disc lead to stronger, more chaotic torques and higher average accretion rates. These systems are likely to merge more rapidly and their chaotic gas dynamics may produce distinctive EM variability.

• Sink dependence:

The results are robust across a range of numerical setups, though the choice of sink radius affects the fine structure of the minidiscs and the detailed torque calculations. Smaller sink radii preserve more of the minidisc's structure.

Conclusion

We demonstrate that the hydrodynamical environment of AGN discs plays a critical role in shaping the evolution and observable properties of embedded BBHs. The presence of dense gas and strong shocks in AGN discs ensures that BBHs experience sustained angular momentum loss, driving them toward merger on realistic timescales. Accretion dynamics are highly asymmetric with the secondary black hole typically dominating the accretion rate, especially in unequal-mass systems. This may lead to mass ratio evolution over time. The orientation of the binary orbit relative to the disc has a profound effect on the system's evolution, with retrograde binaries merging more rapidly due to enhanced torques and accretion variability. The complex interplay between accretion, torque, and mass sloshing produces rich variability that could manifest in EM counterparts to GW events, offering a pathway for multi-messenger observations.

Future Directions:

This thesis lays the groundwork for more comprehensive models that integrate further physics, such as magnetic fields (magnetohydrodynamics, MHD) and full 3-D simulations. Magnetic fields are expected to significantly impact angular momentum transfer, variability in accretion, and jet formation, which are essential for predicting EM counterparts. A detailed paper presenting this results is currently in preparation (Joshi et al., 2025 in preparation). Key findings reveal that BBH embedded in magnetized AGN discs can launch well-collimated, magnetically driven outflows under certain local disc conditions. The development and morphology of these outflows depend on the binary's position in the disc and the surrounding shear, which affects the accumulation of toroidal magnetic fields. In some regions, the ambient conditions inhibit outflows and favours accretion-dominated dynamics, while elsewhere, robust outflows can form, potentially creating pathways through the optically thick disc and enabling the escape of EM radiation. Accretion onto BBHs occurs episodically, with burst phases marked by plasmoid ejections. The system presents a wide range of flow structures, including turbulent accretion and spiral shocks, highlighting the intricate interaction between the BBH and its local environment. The findings are directly relevant for interpreting current and future observations from GW detectors and time-domain EM surveys and for constraining models of black hole growth and galaxy evolution.

CHAPTER 5

APPENDIX

Appendix A

A.1 The radiation field

The gravitational waveform generated by a compact binary system is expressed by a sum of contributions originating from different PN orders. The particular form of the contributions listed in Eq. (2.13) can be found in Kidder (1995), but for conveniences they are also summarized below. Accordingly, the quadrupole term and higher order relativistic corrections read as

$$Q^{ij} = 2 \left[v^{i}v^{j} - \frac{Gm}{r} n^{i}n^{j} \right], \tag{A.1}$$

$$P^{0.5}Q^{ij} = \frac{\delta m}{cm} \left\{ 3 \frac{Gm}{r} \left[2n^{(i}v^{j)} - \dot{r}n^{i}n^{j} \right] (\hat{\mathbf{N}} \cdot \hat{\mathbf{n}}) + \left[\frac{Gm}{r} n^{i}n^{j} - 2v^{i}v^{j} \right] (\hat{\mathbf{N}} \cdot \mathbf{v}) \right\}, \tag{A.2}$$

$$PQ^{ij} = \frac{1}{3c^{2}} (1 - 3\eta) \left\{ 4 \frac{Gm}{r} \left[3\dot{r}n^{i}n^{j} - 8n^{(i}v^{j)} \right] (\hat{\mathbf{N}} \cdot \hat{\mathbf{n}}) (\hat{\mathbf{N}} \cdot \mathbf{v}) + 2 \left[3v^{i}v^{j} - \frac{Gm}{r} n^{i}n^{j} \right] (\hat{\mathbf{N}} \cdot \mathbf{v})^{2} + \frac{Gm}{r} \left[(3v^{2} - 15\dot{r}^{2} + 7\frac{Gm}{r})n^{i}n^{j} + 30\dot{r}n^{(i}v^{j)} - 14v^{i}v^{j} \right] (\hat{\mathbf{N}} \cdot \hat{\mathbf{n}})^{2} \right\} + \frac{4}{3} \frac{Gm}{r} \dot{r}(5 + 3\eta)n^{(i}v^{j)} + \left[(1 - 3\eta)v^{2} - \frac{2}{3}(2 - 3\eta)\frac{Gm}{r} \right] v^{i}v^{j} + \frac{Gm}{r} \left[(1 - 3\eta)\dot{r}^{2} - \frac{1}{3}(10 + 3\eta)v^{2} + \frac{29}{3}\frac{Gm}{r} \right] n^{i}n^{j}, \tag{A.3}$$

$$P^{1.5}Q^{ij} = \frac{\delta m}{mc^3} (1 - 2\eta) \left\{ \frac{1}{4} \frac{Gm}{r} \left[(45\dot{r}^2 - 9v^2 - 28\frac{Gm}{r})n^i n^j + 58v^i v^j - 108\dot{r}n^{(i}v^{j)} \right] (\hat{\mathbf{N}} \cdot \hat{\mathbf{n}})^2 (\hat{\mathbf{N}} \cdot \mathbf{v}) \right.$$

$$+ \frac{1}{2} \left[\frac{Gm}{r} n^i n^j - 4v^i v^j \right] (\hat{\mathbf{N}} \cdot \mathbf{v})^3 + \frac{Gm}{r} \left[\frac{5}{4} (3v^2 - 7\dot{r}^2 + 6\frac{Gm}{r})\dot{r}n^i n^j - \frac{1}{6} (21v^2 - 105\dot{r}^2) \right] \left. + 44\frac{Gm}{r} (n^i v^j) - \frac{17}{2}\dot{r}v^i v^j \right] (\hat{\mathbf{N}} \cdot \hat{\mathbf{n}})^3 + \frac{3}{2} \frac{Gm}{r} \left[10n^{(i}v^{j)} - 3\dot{r}n^i n^j \right] (\hat{\mathbf{N}} \cdot \hat{\mathbf{n}}) (\hat{\mathbf{N}} \cdot \mathbf{v})^2 \right\}$$

$$+ \frac{\delta m}{mc^3} \frac{1}{12} \frac{Gm}{r} (\hat{\mathbf{N}} \cdot \hat{\mathbf{n}}) \left\{ n^i n^j \dot{r} \left[\dot{r}^2 (15 - 90\eta) - v^2 (63 - 54\eta) + \frac{Gm}{r} (242 - 24\eta) \right] \right.$$

$$- \dot{r}v^i v^j (186 + 24\eta) + 2n^{(i}v^{j)} \left[\dot{r}^2 (63 + 54\eta) - \frac{Gm}{r} (128 - 36\eta) + v^2 (33 - 18\eta) \right] \right\}$$

$$+ \frac{\delta m}{mc^3} (\hat{\mathbf{N}} \cdot \mathbf{v}) \left\{ \frac{1}{2} v^i v^j \left[\frac{Gm}{r} (3 - 8\eta) - 2v^2 (1 - 5\eta) \right] - n^{(i}v^{j)} \frac{Gm}{r} \dot{r} (7 + 4\eta) \right.$$

$$- n^i n^j \frac{Gm}{r} \left[\frac{3}{4} (1 - 2\eta) \dot{r}^2 + \frac{1}{3} (26 - 3\eta) \frac{Gm}{r} - \frac{1}{4} (7 - 2\eta) v^2 \right] \right\}, \tag{A.4}$$

where $\mathbf{r} = \mathbf{x_1} - \mathbf{x_2}$, $\mathbf{v} = d\mathbf{r}/dt$, $\hat{\mathbf{n}} = \mathbf{r}/r$, $m = m_1 + m_2$, $\delta m = m_1 - m_2$, $\eta = \mu/m$ and the derivative with respect to time is indicated by an overdot. The P^2Q^{ij} contribution to the waveform is (Will and Wiseman, 1996):

$$\begin{split} P^2 \mathcal{Q}^{ij} &= \frac{1}{c^4} \bigg[\frac{1}{60} (1 - 5\eta + 5\eta^2) \bigg\{ 24 (\hat{\mathbf{N}} \cdot \mathbf{v})^4 \bigg[5v^i v^j - \frac{m}{r} \hat{n}^i \hat{n}^j \bigg] \\ &+ \frac{m}{r} (\hat{\mathbf{N}} \cdot \hat{\mathbf{n}})^4 \bigg[2 \left(175 \frac{m}{r} - 465 \dot{r}^2 + 93 v^2 \right) v^i v^j + 30 \dot{r} \left(63 \dot{r}^2 - 50 \frac{m}{r} - 27 v^2 \right) \hat{n}^{(i} v^{j)} \\ &+ \left(1155 \frac{m}{r} \dot{r}^2 - 172 \left(\frac{m}{r} \right)^2 - 945 \dot{r}^4 - 159 \frac{m}{r} v^2 + 630 \dot{r}^2 v^2 - 45 v^4 \right) \hat{n}^i \hat{n}^j \bigg] \\ &+ 24 \frac{m}{r} (\hat{\mathbf{N}} \cdot \hat{\mathbf{n}})^3 (\hat{\mathbf{N}} \cdot \mathbf{v}) \bigg[87 \dot{r} \dot{v}^i v^j + 5 \dot{r} \left(14 \dot{r}^2 - 15 \frac{m}{r} - 6 v^2 \right) \hat{n}^i \hat{n}^j \\ &+ 16 \left(5 \frac{m}{r} - 10 \dot{r}^2 + 2 v^2 \right) \hat{n}^{(i} v^j) \bigg] + 288 \frac{m}{r} (\hat{\mathbf{N}} \cdot \hat{\mathbf{n}}) (\hat{\mathbf{N}} \cdot \mathbf{v})^3 \bigg[\dot{r} \hat{n}^i \hat{n}^j - 4 \hat{n}^{(i} v^j) \bigg] \\ &+ 24 \frac{m}{r} (\hat{\mathbf{N}} \cdot \hat{\mathbf{n}})^2 (\hat{\mathbf{N}} \cdot \mathbf{v})^2 \bigg[\left(35 \frac{m}{r} - 45 \dot{r}^2 + 9 v^2 \right) \hat{n}^i \hat{n}^j - 76 v^i v^j + 126 \dot{r} \hat{n}^{(i} v^j) \bigg] \bigg\} \\ &+ \frac{1}{15} (\hat{\mathbf{N}} \cdot \mathbf{v})^2 \bigg\{ \bigg[5(25 - 78 \eta + 12 \eta^2) \frac{m}{r} - (18 - 65 \eta + 45 \eta^2) v^2 \\ &+ 9(1 - 5 \eta + 5 \eta^2) \dot{r}^2 \bigg] \frac{m}{r} \hat{n}^i \hat{n}^j + 3 \bigg[5(1 - 9 \eta + 21 \eta^2) v^2 - 2(4 - 25 \eta + 45 \eta^2) \frac{m}{r} \bigg] v^i v^j \\ &+ 18(6 - 15 \eta - 10 \eta^2) \frac{m}{r} \dot{r} \hat{n}^{(i} v^j) \bigg\} + \frac{1}{15} (\hat{\mathbf{N}} \cdot \hat{\mathbf{n}}) (\hat{\mathbf{N}} \cdot \mathbf{v}) \frac{m}{r} \bigg\{ \bigg[3(36 - 145 \eta + 150 \eta^2) v^2 \bigg] v^2 \bigg\} \end{split}$$

$$\begin{split} &-5(127-392\eta+36\eta^2)\frac{m}{r}-15(2-15\eta+30\eta^2)\dot{r}^2\Big]\dot{r}\hat{n}^i\hat{n}^j\\ &+6(98-295\eta-30\eta^2)\dot{r}v^iv^j+2\bigg[5(66-221\eta+96\eta^2)\frac{m}{r}\\ &-9(18-45\eta-40\eta^2)\dot{r}^2-(66-265\eta+360\eta^2)v^2\Big]\hat{n}^{(i}v^{j)}\bigg\}\\ &+\frac{1}{60}(\hat{\mathbf{N}}\cdot\hat{\mathbf{n}})^2\frac{m}{r}\bigg\{\bigg[3(33-130\eta+150\eta^2)v^4+105(1-10\eta+30\eta^2)\dot{r}^4\\ &+15(181-572\eta+84\eta^2)\frac{m}{r}\dot{r}^2-(131-770\eta+930\eta^2)\frac{m}{r}v^2\\ &-60(9-40\eta+60\eta^2)v^2\dot{r}^2-8(131-390\eta+30\eta^2)\left(\frac{m}{r}\right)^2\Big]\hat{n}^i\dot{n}^j\\ &+4\bigg[(12+5\eta-315\eta^2)v^2-9(39-115\eta-35\eta^2)\dot{r}^2+5(29-104\eta+84\eta^2)\frac{m}{r}\Big]v^iv^j\\ &+4\bigg[15(18-40\eta-75\eta^2)\dot{r}^2-5(197-640\eta+180\eta^2)\frac{m}{r}\\ &+3(21-130\eta+375\eta^2)v^2\Big]\dot{r}\hat{n}^{(i}v^{j)}\bigg\}\\ &+\frac{1}{60}\bigg\{\bigg[(467+780\eta-120\eta^2)\frac{m}{r}v^2-15(61-96\eta+48\eta^2)\frac{m}{r}\dot{r}^2\\ &-(144-265\eta-135\eta^2)v^4+6(24-95\eta+75\eta^2)v^2\dot{r}^2\\ &-2(642+545\eta)\left(\frac{m}{r}\right)^2-45(1-5\eta+5\eta^2)\dot{r}^4\bigg]\frac{m}{r}\hat{n}^i\dot{n}^j\\ &+\bigg[4(69+10\eta-135\eta^2)\frac{m}{r}v^2-12(3+60\eta+25\eta^2)\frac{m}{r}\dot{r}^2\\ &+45(1-7\eta+13\eta^2)v^4-10(56+165\eta-12\eta^2)\left(\frac{m}{r}\right)^2\bigg]v^iv^j\\ &+4\bigg[2(36+5\eta-75\eta^2)v^2-6(7-15\eta-15\eta^2)\dot{r}^2+5(35+45\eta+36\eta^2)\frac{m}{r}\bigg]\frac{m}{r}\dot{r}\hat{n}^i\dot{n}^i\dot{r}^j\bigg], \end{split}$$

The analogous expressions for spin contributions are:

$$PQ_{SO}^{ij} = \frac{2G}{cr^{2}} (\mathbf{\Delta} \times \hat{\mathbf{N}})^{(i} n^{j)}, \qquad (A.6)$$

$$P^{1.5}Q_{SO}^{ij} = \frac{2G}{c^{2}r^{2}} \left\{ n^{i} n^{j} \left[(\hat{\mathbf{n}} \times \mathbf{v}) \cdot (12\mathbf{S} + 6\frac{\delta m}{m} \mathbf{\Delta}) \right] - n^{(i} \left[\mathbf{v} \times (9\mathbf{S} + 5\frac{\delta m}{m} \mathbf{\Delta}) \right]^{j)} + \left[3\dot{r} (\hat{\mathbf{N}} \cdot \hat{\mathbf{n}}) - 2(\hat{\mathbf{N}} \cdot \mathbf{v}) \right] \left[(\mathbf{S} + \frac{\delta m}{m} \mathbf{\Delta}) \times \hat{\mathbf{N}} \right]^{(i)} n^{j)} - v^{(i} \left[\hat{\mathbf{n}} \times (2\mathbf{S} + 2\frac{\delta m}{m} \mathbf{\Delta}) \right]^{j)} + \dot{r} n^{(i)} \left[\hat{\mathbf{n}} \times (12\mathbf{S} + 6\frac{\delta m}{m} \mathbf{\Delta}) \right]^{j)} - 2(\hat{\mathbf{N}} \cdot \hat{\mathbf{n}}) \left[(\mathbf{S} + \frac{\delta m}{m} \mathbf{\Delta}) \times \hat{\mathbf{N}} \right]^{(i)} v^{j)} \right\}, \qquad (A.7)$$

$$P^{2}Q_{SS}^{ij} = -\frac{6G}{c^{2}\mu r^{3}} \left\{ n^{i}n^{j} \left[(\mathbf{S_{1}} \cdot \mathbf{S_{2}}) - 5(\mathbf{\hat{n}} \cdot \mathbf{S_{1}})(\mathbf{\hat{n}} \cdot \mathbf{S_{2}}) \right] + 2n^{(i}S_{1}^{j)}(\mathbf{\hat{n}} \cdot \mathbf{S_{2}}) + 2n^{(i}S_{2}^{j)}(\mathbf{\hat{n}} \cdot \mathbf{S_{1}}) \right\}.$$
(A.8)

where $S = S_1 + S_2$ and $\Delta = m(S_2/m_2 - S_1/m_1)$.

In black hole perturbation theory and in numerical simulations the radiation field is frequently given in terms of spin weighted spherical harmonics. As the injection of numerical templates also requires this type of expansion (Ajith et al., 2011) CBwaves does contain a module evaluating some of the spin weighted spherical harmonics. The relations we have applied in generating the components read as

$$MH_{lm} = \oint_{-2}^{-2} Y_{lm}^*(\iota, \phi) (rh_+ - irh_\times) d\Omega, \tag{A.9}$$

where, for example,

$$^{-2}Y_{2\pm 2} = \sqrt{\frac{5}{64\pi}} \left(1 \pm \cos \iota\right)^2 e^{\pm 2i\phi},\tag{A.10}$$

$$^{-2}Y_{2\pm 1} = \sqrt{\frac{5}{16\pi}} \sin \iota (1 \pm \cos \iota) e^{\pm i\phi}, \tag{A.11}$$

$$^{-2}Y_{20} = \sqrt{\frac{5}{32\pi}}\sin^2\iota. \tag{A.12}$$

 $h_{+}^{(lm)}$ and $h_{\times}^{(lm)}$ are defined as

$$rh_{+}^{(lm)}(t) - irh_{\times}^{(lm)}(t) = MH_{lm}(t).$$
 (A.13)

Note that these modes of rh_+ and rh_\times are used for injections (Ajith et al., 2011).

Appendix B

B.1 Equations of motion

The various order of relative accelerations, as listed in Eq. (2.14), can be given as

$$\mathbf{a}_N = -\frac{Gm}{r^2}\hat{\mathbf{n}},\tag{B.1}$$

$$\mathbf{a}_{PN} = -\frac{Gm}{c^2 r^2} \left\{ \hat{\mathbf{n}} \left[(1 + 3\eta) v^2 - 2(2 + \eta) \frac{Gm}{r} - \frac{3}{2} \eta \dot{r}^2 \right] - 2(2 - \eta) \dot{r} \mathbf{v} \right\},\tag{B.2}$$

$$\mathbf{a}_{SO} = \frac{G}{c^2 r^3} \left\{ 6\hat{\mathbf{n}} [(\hat{\mathbf{n}} \times \mathbf{v}) \cdot (\mathbf{S} + \boldsymbol{\sigma})] - [\mathbf{v} \times (4\mathbf{S} + 3\boldsymbol{\sigma})] + 3\dot{r} [\hat{\mathbf{n}} \times (2\mathbf{S} + \boldsymbol{\sigma})] \right\}, \tag{B.3}$$

$$\mathbf{a}_{2PN} = -\frac{Gm}{c^4r^2} \left\{ \hat{\mathbf{n}} \left[\frac{3}{4} (12 + 29\eta) (\frac{Gm}{r})^2 + \eta (3 - 4\eta) v^4 + \frac{15}{8} \eta (1 - 3\eta) \dot{r}^4 \right] \right\}$$

$$-\frac{3}{2}\eta(3-4\eta)v^2\dot{r}^2 - \frac{1}{2}\eta(13-4\eta)\frac{Gm}{r}v^2 - (2+25\eta+2\eta^2)\frac{Gm}{r}\dot{r}^2\bigg]$$

$$-\frac{1}{2}\dot{r}\mathbf{v}\left[\eta(15+4\eta)v^2-(4+41\eta+8\eta^2)\frac{Gm}{r}-3\eta(3+2\eta)\dot{r}^2\right],\tag{B.4}$$

$$\mathbf{a}_{SS} = -\frac{3G}{c^2 \mu r^4} \left\{ \mathbf{\hat{n}} (\mathbf{S}_1 \cdot \mathbf{S}_2) + \mathbf{S}_1 (\mathbf{\hat{n}} \cdot \mathbf{S}_2) + \mathbf{S}_2 (\mathbf{\hat{n}} \cdot \mathbf{S}_1) - 5\mathbf{\hat{n}} (\mathbf{\hat{n}} \cdot \mathbf{S}_1) (\mathbf{\hat{n}} \cdot \mathbf{S}_2) \right\},$$
(B.5)

$$\mathbf{a}_{RR}^{BT} = \frac{8}{5} \eta \frac{G^2 m^2}{c^5 r^3} \left\{ \dot{r} \hat{\mathbf{n}} \left[18v^2 + \frac{2}{3} \frac{Gm}{r} - 25\dot{r}^2 \right] - \mathbf{v} \left[6v^2 - 2\frac{Gm}{r} - 15\dot{r}^2 \right] \right\},\tag{B.6}$$

where $\sigma = (m_2/m_1)\mathbf{S}_1 + (m_1/m_2)\mathbf{S}_2$. Note also that the above form of \mathbf{a}_{SO} tacitly presumes the use of the covariant spin supplementary condition, $S_A^{\mu\nu}u_{A\nu} = 0$, where u_A^{μ} is the four-velocity of the center-of-mass world line of body A, with A = 1, 2. Finally, as discussed above the term \mathbf{a}_{RR}^{BT} refers to the radiation reaction expression derived from a Burke-Thorne type radiation reaction potential (Iyer and Will, 1995; Zeng and Will, 2007).

Higher order corrections to the acceleration are given as

$$\begin{split} \mathbf{a}_{PNSO} &= \frac{G}{c^4 r^3} \bigg\{ \hat{\mathbf{n}} \bigg[(\hat{\mathbf{n}} \times \mathbf{v}) \cdot \mathbf{S} \bigg(-30 \eta \dot{r}^2 + 24 \eta v^2 - \frac{Gm}{r} (38 + 25 \eta) \bigg) \\ &+ \frac{\delta m}{m} (\hat{\mathbf{n}} \times \mathbf{v}) \cdot \Delta \bigg(-15 \eta \dot{r}^2 + 12 \eta v^2 - \frac{Gm}{r} (18 + \frac{29}{2} \eta) \bigg) \bigg] \\ &+ \dot{r} \mathbf{v} \bigg[(\hat{\mathbf{n}} \times \mathbf{v}) \cdot \mathbf{S} (-9 + 9 \eta) + \frac{\delta m}{m} (\hat{\mathbf{n}} \times \mathbf{v}) \cdot \Delta (-3 + 6 \eta) \bigg] \\ &+ \hat{\mathbf{n}} \times \mathbf{v} \bigg[\dot{r} (\mathbf{v} \cdot \mathbf{S}) (-3 + 3 \eta) - 8 \frac{Gm}{r} \eta (\hat{\mathbf{n}} \cdot \mathbf{S}) - \frac{\delta m}{m} \bigg(4 \frac{Gm}{r} \eta (\hat{\mathbf{n}} \cdot \Delta) + 3 \dot{r} (\mathbf{v} \cdot \Delta) \bigg) \bigg] \\ &+ \dot{r} \hat{\mathbf{n}} \times \mathbf{S} \bigg[- \frac{45}{2} \eta \dot{r}^2 + 21 \eta v^2 - \frac{Gm}{r} (25 + 15 \eta) \bigg] \\ &+ \frac{\delta m}{m} \dot{r} \hat{\mathbf{n}} \times \Delta \bigg[-15 \eta \dot{r}^2 + 12 \eta v^2 - \frac{Gm}{r} (9 + \frac{17}{2} \eta) \bigg] \end{split}$$

$$+ \mathbf{v} \times \mathbf{S} \left[\frac{33}{2} \eta \dot{r}^2 + \frac{Gm}{r} (21 + 9\eta) - 14\eta v^2 \right]$$

$$+ \frac{\delta m}{m} \mathbf{v} \times \mathbf{\Delta} \left[9\eta \dot{r}^2 - 7\eta v^2 + \frac{Gm}{r} (9 + \frac{9}{2}\eta) \right] \right\}, \tag{B.7}$$

$$\mathbf{a}_{3PN} = \frac{Gm}{c^{3}r^{2}} \left\{ \hat{\mathbf{n}} \left[\left[16 + \left(\frac{1399}{12} - \frac{41}{16}\pi^{2} \right) \eta + \frac{71}{2}\eta^{2} \right] \left(\frac{Gm}{r} \right)^{3} + \eta \left[\frac{20827}{840} + \frac{123}{64}\pi^{2} - \eta^{2} \right] \left(\frac{Gm}{r} \right)^{2} v^{2} \right. \\ \left. - \left[1 + \left(\frac{22717}{168} + \frac{615}{64}\pi^{2} \right) \eta + \frac{11}{8}\eta^{2} - 7\eta^{3} \right] \left(\frac{Gm}{r} \right)^{2} \dot{r}^{2} \right. \\ \left. - \frac{1}{4}\eta (11 - 49\eta + 52\eta^{2})v^{6} + \frac{35}{16}\eta (1 - 5\eta + 5\eta^{2})\dot{r}^{6} - \frac{1}{4}\eta \left(75 + 32\eta - 40\eta^{2} \right) \frac{Gm}{r} v^{4} \right. \\ \left. - \frac{1}{2}\eta \left(158 - 69\eta - 60\eta^{2} \right) \frac{Gm}{r} \dot{r}^{4} + \eta \left(121 - 16\eta - 20\eta^{2} \right) \frac{Gm}{r} v^{2} \dot{r}^{2} \right. \\ \left. + \frac{3}{8}\eta \left(20 - 79\eta + 60\eta^{2} \right) v^{4} \dot{r}^{2} - \frac{15}{8}\eta \left(4 - 18\eta + 17\eta^{2} \right) v^{2} \dot{r}^{4} \right] \right. \\ \left. + \dot{r} \mathbf{v} \left[\left[4 + \left(\frac{5849}{840} + \frac{123}{32}\pi^{2} \right) \eta - 25\eta^{2} - 8\eta^{3} \right] \left(\frac{Gm}{r} \right)^{2} + \frac{1}{8}\eta \left(65 - 152\eta - 48\eta^{2} \right) v^{4} \right. \\ \left. + \frac{15}{8}\eta \left(3 - 8\eta - 2\eta^{2} \right) \dot{r}^{4} + \eta \left(15 + 27\eta + 10\eta^{2} \right) \frac{Gm}{r} v^{2} \right. \\ \left. - \frac{1}{6}\eta \left(329 + 177\eta + 108\eta^{2} \right) \frac{Gm}{r} \dot{r}^{2} - \frac{3}{4}\eta \left(16 - 37\eta - 16\eta^{2} \right) v^{2} \dot{r}^{2} \right] \right\},$$
 (B.8)

$$\mathbf{a}_{RR1PN} = \frac{8}{5} \eta \frac{G^2 m^2}{c^7 r^3} \left\{ \dot{r} \hat{\mathbf{n}} \left[\left(\frac{87}{14} - 48\eta \right) v^4 - \left(\frac{5379}{28} - \frac{136}{3} \eta \right) v^2 \frac{Gm}{r} + \frac{25}{2} (1 + 5\eta) v^2 \dot{r}^2 \right. \\ \left. + \left(\frac{1353}{4} - 133\eta \right) \dot{r}^2 \frac{Gm}{r} - \frac{35}{2} (1 - \eta) \dot{r}^4 + \left(\frac{160}{7} + \frac{55}{3} \eta \right) \left(\frac{Gm}{r} \right)^2 \right] \\ \left. - \mathbf{v} \left[-\frac{27}{14} v^4 - \left(\frac{4861}{84} + \frac{58}{3} \eta \right) v^2 \frac{Gm}{r} + \frac{3}{2} (13 - 37\eta) v^2 \dot{r}^2 \right. \\ \left. + \left(\frac{2591}{12} + 97\eta \right) \dot{r}^2 \frac{Gm}{r} - \frac{25}{2} (1 - 7\eta) \dot{r}^4 + \frac{1}{3} \left(\frac{776}{7} + 55\eta \right) \left(\frac{Gm}{r} \right)^2 \right] \right\}, \tag{B.9}$$

$$\mathbf{a}_{RRSO} = -\frac{G^{2}\eta m}{5c^{7}r^{4}} \left\{ \frac{\dot{r}\hat{\mathbf{n}}}{\mu r} \left[\left(120v^{2} + 280\dot{r}^{2} + 453\frac{Gm}{r} \right) \mathbf{L}_{N} \cdot \mathbf{S} \right. \\ \left. + \left(120v^{2} + 280\dot{r}^{2} + 458\frac{Gm}{r} \right) \mathbf{L}_{N} \cdot \boldsymbol{\sigma} \right] \right. \\ \left. + \frac{\mathbf{v}}{\mu r} \left[\left(87v^{2} - 675\dot{r}^{2} - \frac{901}{3}\frac{Gm}{r} \right) \mathbf{L}_{N} \cdot \mathbf{S} + 4 \left(18v^{2} - 150\dot{r}^{2} - 66\frac{Gm}{r} \right) \mathbf{L}_{N} \cdot \boldsymbol{\sigma} \right] \right. \\ \left. - \frac{2}{3}\dot{r}\mathbf{v} \times \mathbf{S} \left(48v^{2} + 15\dot{r}^{2} + 364\frac{Gm}{r} \right) + \frac{1}{3}\dot{r}\mathbf{v} \times \boldsymbol{\sigma} \left(291v^{2} - 705\dot{r}^{2} - 772\frac{Gm}{r} \right) \right.$$

$$+\frac{1}{2}\hat{\mathbf{n}} \times \mathbf{S} \left(31v^4 - 260v^2\dot{r}^2 + 245\dot{r}^4 - \frac{689}{3}v^2\frac{Gm}{r} + 537\dot{r}^2\frac{Gm}{r} + \frac{4}{3}\frac{G^2m^2}{r^2} \right) + \frac{1}{2}\hat{\mathbf{n}} \times \boldsymbol{\sigma} \left(115v^4 - 1130v^2\dot{r}^2 + 1295\dot{r}^4 - \frac{869}{3}v^2\frac{Gm}{r} + 849\dot{r}^2\frac{Gm}{r} + \frac{44}{3}\frac{G^2m^2}{r^2} \right) \right\},$$
(B.10)

$$\mathbf{a}_{RRSS} = \frac{G^2}{c^7 r^5} \left\{ \hat{\mathbf{n}} \left[\left(287 \dot{r}^2 - 99 v^2 + \frac{541}{5} \frac{Gm}{r} \right) \dot{r} (\mathbf{S}_1 \cdot \mathbf{S}_2) \right. \right. \\ \left. - \left(2646 \dot{r}^2 - 714 v^2 + \frac{1961}{5} \frac{Gm}{r} \right) \dot{r} (\hat{\mathbf{n}} \cdot \mathbf{S}_1) (\hat{\mathbf{n}} \cdot \mathbf{S}_2) \right. \\ \left. + \left(1029 \dot{r}^2 - 123 v^2 + \frac{629}{10} \frac{Gm}{r} \right) \left((\hat{\mathbf{n}} \cdot \mathbf{S}_1) (\hat{\mathbf{v}} \cdot \mathbf{S}_2) + (\hat{\mathbf{n}} \cdot \mathbf{S}_2) (\hat{\mathbf{v}} \cdot \mathbf{S}_1) \right) \right. \\ \left. - 336 \dot{r} (\hat{\mathbf{v}} \cdot \mathbf{S}_1) (\hat{\mathbf{v}} \cdot \mathbf{S}_2) \right] + \mathbf{v} \left[\left(\frac{171}{5} v^2 - 195 \dot{r}^2 - 67 \frac{Gm}{r} \right) (\mathbf{S}_1 \cdot \mathbf{S}_2) \right. \\ \left. - \left(174 v^2 - 1386 \dot{r}^2 - \frac{1038}{5} \frac{Gm}{r} \right) (\hat{\mathbf{n}} \cdot \mathbf{S}_1) (\hat{\mathbf{n}} \cdot \mathbf{S}_2) \right. \\ \left. - 438 \dot{r} \left((\hat{\mathbf{n}} \cdot \mathbf{S}_1) (\hat{\mathbf{v}} \cdot \mathbf{S}_2) + (\hat{\mathbf{n}} \cdot \mathbf{S}_2) (\hat{\mathbf{v}} \cdot \mathbf{S}_1) \right) + 96 (\hat{\mathbf{v}} \cdot \mathbf{S}_1) (\hat{\mathbf{v}} \cdot \mathbf{S}_2) \right] \right. \\ \left. + \left(\frac{27}{10} v^2 - \frac{75}{2} \dot{r}^2 - \frac{509}{30} \frac{Gm}{r} \right) \left((\hat{\mathbf{v}} \cdot \mathbf{S}_2) \mathbf{S}_1 + (\hat{\mathbf{v}} \cdot \mathbf{S}_1) \mathbf{S}_2 \right) \right. \\ \left. + \left(\frac{15}{2} v^2 + \frac{77}{2} \dot{r}^2 + \frac{199}{10} \frac{Gm}{r} \right) \dot{r} \left((\hat{\mathbf{n}} \cdot \mathbf{S}_2) \mathbf{S}_1 + (\hat{\mathbf{n}} \cdot \mathbf{S}_1) \mathbf{S}_2 \right) \right\}.$$
 (B.11)

In general, the accelerations \mathbf{a}_{SO} and \mathbf{a}_{SS} are not confined to the orbital plane thereby they yield a precession of this plane and, in turn, an amplitude and frequency modulation of the observed signal. In addition, spin vectors themselves precess according to their evolution equations

$$\mathbf{S}_{i} = \frac{G}{c^{2}r^{3}} \left\{ \frac{4 + 3\zeta_{i}}{2} \mathbf{L}_{N} - \mathbf{S}_{j} + 3\left(\hat{\mathbf{n}} \cdot \mathbf{S}_{j}\right) \hat{\mathbf{n}} + \frac{G^{2}\mu m}{c^{5}r^{2}} \left[\frac{2}{3} \left(\mathbf{v} \cdot \mathbf{S}_{j} \right) + 30\dot{r} \left(\hat{\mathbf{n}} \cdot \mathbf{S}_{j} \right) \right] \hat{\mathbf{n}} \right\} \times \mathbf{S}_{i},$$
(B.12)

where $\mathbf{L}_N = \mu \mathbf{r} \times \mathbf{v}$ is the Newtonian angular momentum and $\zeta_i = m_j/m_i$, with i, j = 1, 2, $i \neq j$. In Eq. (B.12), in addition to the standard spin-orbit and spin-spin terms (Kidder, 1995), the last expression stands for the 3.5PN spin-spin contribution (Wang and Will, 2007).

The terms in the equations of motion, Eq. (2.14), up to 2PN order can be deduced from a generalized Lagrangian which depends only on the relative acceleration. From this Lagrangian the energy E and total angular momentum J of the system can be computed which are known to be conserved up to 2PN order (Kidder, 1995), i.e. in the absence of radiation reaction.

The conserved total angular momentum is

$$\mathbf{J} = \mathbf{L} + \mathbf{S},\tag{B.13}$$

where

$$L = L_N + L_{PN} + L_{SO} + L_{2PN} + L_{3PN},$$
(B.14)

Notice that at the applied level of PN approximation there is no spin-spin contribution to J.

The leading order radiative change of the conserved quantities E and J is governed by the quadrupole formula (Iyer and Will, 1995). To lowest 2.5PN order the instantaneous loss of energy E is given as (Kidder, 1995)

$$\frac{dE_N}{dt} = -\frac{8}{15} \frac{G^3 m^2 \mu^2}{c^5 r^4} \left(12v^2 - 11\dot{r}^2 \right),\tag{B.15}$$

while the radiative angular momentum loss is

$$\frac{d\mathbf{J}_N}{dt} = -\frac{8}{5} \frac{G^2 m \mu}{c^5 r^3} \mathbf{L}_N \left(2v^2 - 3\dot{r}^2 + 2\frac{Gm}{r} \right). \tag{B.16}$$

$$\mathcal{A}_{1PN} = -\frac{3\dot{r}^{2}v}{2} + v^{2} + 3vv^{2} - \frac{Gm}{r} (4 + 2v), \qquad (B.17a)$$

$$\mathcal{A}_{2PN} = \frac{15\dot{r}^{4}v}{8} - \frac{45\dot{r}^{4}v^{2}}{8} - \frac{9\dot{r}^{2}vv^{2}}{2} + 6\dot{r}^{2}v^{2}v^{2} + 3vv^{4} - 4v^{2}v^{4}$$

$$+ \frac{Gm}{r} \left(-2\dot{r}^{2} - 25\dot{r}^{2}v - 2\dot{r}^{2}v^{2} - \frac{13vv^{2}}{2} + 2v^{2}v^{2} \right)$$

$$+ \frac{G^{2}m^{2}}{r^{2}} \left(9 + \frac{87v}{4} \right), \qquad (B.17b)$$

$$\mathcal{A}_{2.5PN} = \frac{8Gmv}{5r} \dot{r} \left[-\frac{17}{3} \frac{Gm}{r} - 3v^{2} \right], \qquad (B.17c)$$

$$\mathcal{A}_{3PN} = -\frac{35\dot{r}^{6}v}{16} + \frac{175\dot{r}^{6}v^{2}}{16} - \frac{175\dot{r}^{6}v^{3}}{16} + \frac{15\dot{r}^{4}vv^{2}}{2}$$

$$-\frac{135\dot{r}^{4}v^{2}v^{2}}{4} + \frac{255\dot{r}^{4}v^{3}v^{2}}{8} - \frac{15\dot{r}^{2}vv^{4}}{2} + \frac{237\dot{r}^{2}v^{2}v^{4}}{8}$$

$$-\frac{45\dot{r}^{2}v^{3}v^{4}}{2} + \frac{11vv^{6}}{4} - \frac{49v^{2}v^{6}}{4} + 13v^{3}v^{6}$$

$$+\frac{Gm}{r} \left(79\dot{r}^{4}v - \frac{69\dot{r}^{4}v^{2}}{2} - 30\dot{r}^{4}v^{3} - 121\dot{r}^{2}vv^{2} + 16\dot{r}^{2}v^{2}v^{2} \right)$$

$$+20\dot{r}^{2}v^{3}v^{2} + \frac{75vv^{4}}{4} + 8v^{2}v^{4} - 10v^{3}v^{4} \right)$$

$$+\frac{G^2m^2}{r^2}\left(\dot{r}^2 + \frac{32573\,\dot{r}^2\,\nu}{168} + \frac{11\,\dot{r}^2\,\nu^2}{8} - 7\,\dot{r}^2\,\nu^3 + \frac{615\,\dot{r}^2\,\nu\,\pi^2}{64}\right)$$

$$-\frac{26987\,\nu\,\nu^2}{840} + \nu^3\,\nu^2 - \frac{123\,\nu\,\pi^2\,\nu^2}{64}$$

$$-110\,\dot{r}^2\,\nu\,\ln\left(\frac{r}{r_0'}\right) + 22\,\nu\,\nu^2\,\ln\left(\frac{r}{r_0'}\right)\right)$$

$$+\frac{G^3m^3}{r^3}\left(-16 - \frac{437\,\nu}{4} - \frac{71\,\nu^2}{2} + \frac{41\,\nu\,\pi^2}{16}\right),$$

$$\mathcal{A}_{3.5PN} = \frac{Gm\nu}{r}\dot{r}\left[\frac{G^2m^2}{r^2}\left(\frac{3956}{35} + \frac{184}{5}\nu\right) + \frac{Gm\,\nu^2}{r}\left(\frac{692}{35} - \frac{724}{15}\nu\right)\right]$$

$$+\nu^4\left(\frac{366}{35} + 12\nu\right) + \frac{Gm\,\dot{r}^2}{r}\left(\frac{294}{5} + \frac{376}{5}\nu\right)$$

$$-\nu^2\dot{r}^2\left(114 + 12\nu\right) + 112\dot{r}^4\right]$$
(B.17e)

$$\mathcal{B}_{1PN} = -4\dot{r} + 2\dot{r}\nu, \tag{B.18a}$$

$$\mathcal{B}_{2PN} = \frac{9\,\dot{r}^3\,v}{2} + 3\,\dot{r}^3\,v^2 - \frac{15\,\dot{r}\,v\,v^2}{2} - 2\,\dot{r}\,v^2\,v^2 + \frac{Gm}{r}\left(2\,\dot{r} + \frac{41\,\dot{r}\,v}{2} + 4\,\dot{r}\,v^2\right),\tag{B.18b}$$

$$\mathcal{B}_{2.5PN} = \frac{8G \, m \, v}{5r} \left[3 \frac{Gm}{r} + v^2 \right],$$
 (B.18c)

$$\mathcal{B}_{3PN} = -\frac{45\,\dot{r}^5\,v}{8} + 15\,\dot{r}^5\,v^2 + \frac{15\,\dot{r}^5\,v^3}{4} + 12\,\dot{r}^3\,v\,v^2$$

$$-\frac{111\,\dot{r}^3\,v^2\,v^2}{4} - 12\,\dot{r}^3\,v^3\,v^2 - \frac{65\,\dot{r}\,v\,v^4}{8} + 19\,\dot{r}\,v^2\,v^4 + 6\,\dot{r}\,v^3\,v^4$$

$$+\frac{Gm}{r}\left(\frac{329\,\dot{r}^3\,v}{6} + \frac{59\,\dot{r}^3\,v^2}{2} + 18\,\dot{r}^3\,v^3 - 15\,\dot{r}\,v\,v^2 - 27\,\dot{r}\,v^2\,v^2 - 10\,\dot{r}\,v^3\,v^2\right)$$

$$+\frac{G^2m^2}{r^2}\left(-4\,\dot{r} - \frac{18169\,\dot{r}\,v}{840} + 25\,\dot{r}\,v^2 + 8\,\dot{r}\,v^3 - \frac{123\,\dot{r}\,v\,\pi^2}{32}\right)$$

$$+44\,\dot{r}\,v\,\ln\left(\frac{r}{r_0'}\right), \tag{B.18d}$$

$$\mathcal{B}_{3.5PN} = \frac{Gmv}{r} \left[\frac{G^2m^2}{r^2} \left(-\frac{1060}{21} - \frac{104}{5}v \right) + \frac{Gmv^2}{r} \left(\frac{164}{21} + \frac{148}{5}v \right) \right.$$

$$\left. + v^4 \left(-\frac{626}{35} - \frac{12}{5}v \right) + \frac{Gm\dot{r}^2}{r} \left(-\frac{82}{3} - \frac{848}{15}v \right) \right.$$

$$\left. + v^2\dot{r}^2 \left(\frac{678}{5} + \frac{12}{5}v \right) - 120\dot{r}^4 \right]$$
(B.18e)

BIBLIOGRAPHY

- Abbott, B. P., Abbott, R., Abbott, T. D., Abernathy, M. R., Acernese, F., Ackley, K., Adams, C., Adams, T., Addesso, P., Adhikari, R. X., Adya, V. B., Affeldt, C., Agathos, M., Agatsuma, et al. (2016). Observation of gravitational waves from a binary black hole merger. *Phys. Rev. Lett.*, 116:061102.
- Abbott, B. P. et al. (2020a). Gw190521: A binary black hole merger with a total mass of $150m_{\odot}$. *Physical Review Letters*, 125:101102.
- Abbott, B. P. et al. (2020b). Properties and astrophysical implications of the 150 m_☉ binary black hole merger gw190521. *The Astrophysical Journal*, 900:L13.
- Abbott, R., Abbott, T. D., Acernese, F., Ackley, K., Adams, C., Adhikari, N., Adhikari, R. X., Adya, V. B., Affeldt, C., and Agarwal, D. (2023). Population of merging compact binaries inferred using gravitational waves through gwtc-3. *Phys. Rev. X*, 13:011048.
- Ajith, P., Boyle, M., Brown, D. A., Fairhurst, S., Hannam, M., Hinder, I., Husa, S., Krishnan, B., Mercer, R. A., Ohme, F., Ott, C. D., Read, J. S., Santamaria, L., and Whelan, J. T. (2011). Data formats for numerical relativity waves.
- Armitage, P. J. and Natarajan, P. (2002). Accretion during the merger of supermassive black holes. *The Astrophysical Journal*, 567(1):L9.
- Ashton, G., Ackley, K., Hernandez, I. M., and Piotrzkowski, B. (2021). Current observations are insufficient to confidently associate the binary black hole merger gw190521 with agn j124942.3 + 344929. *Classical and Quantum Gravity*, 38(23):235004.
- Avara, M. J., Krolik, J. H., Campanelli, M., Noble, S. C., Bowen, D., and Ryu, T. (2024). Accretion onto a supermassive black hole binary before merger. *The Astrophysical Journal*, 974(2):242.
- Baruteau, C., Cuadra, J., and Lin, D. N. C. (2010). Binaries migrating in a gaseous disk: Where are the galactic center binaries? *The Astrophysical Journal*, 726(1):28.
- Bate, M. R., Bonnell, I. A., and Bromm, V. (2002). The formation of close binary systems by dynamical interactions and orbital decay. *Monthly Notices of the Royal Astronomical Society*, 336(3):705–713.
- Bern, Z., Parra-Martinez, J., Roiban, R., Ruf, M. S., Shen, C.-H., Solon, M. P., and Zeng, M. (2021). Scattering amplitudes and conservative binary dynamics at $O(G^4)$. *Phys. Rev. Lett.*, 126(17):171601.

- Bini, D., Damour, T., and Geralico, A. (2023). Comparing one-loop gravitational bremsstrahlung amplitudes to the multipolar-post-Minkowskian waveform. *Phys. Rev. D*, 108(12):124052.
- Blanchet, L. (1987). Radiative gravitational fields in general-relativity. II. Asymptotic-behaviour at future null infinity. *Proc. R. Soc. London, Ser. A*, 409:383–399.
- Blanchet, L. (2014). Gravitational radiation from post-Newtonian sources and inspiralling compact binaries. *Living Rev. Relativ.*, 17:2.
- Blanchet, L. and Damour, T. (1986). Radiative gravitational fields in general relativity I. General structure of the field outside the source. *Philos. Trans. R. Soc. London, Ser. A*, 320:379–430.
- Blanchet, L. and Damour, T. (1988). Tail-transported temporal correlations in the dynamics of a gravitating system. *Phys. Rev. D*, 37:1410–1435.
- Blanchet, L. and Damour, T. (1992). Hereditary effects in gravitational radiation. *Phys. Rev. D*, 46:4304–4319.
- Bondi, H., van der Burg, M. G. J., and Metzner, A. W. K. (1962). Gravitational Waves in General Relativity. VII. Waves from Axi-Symmetric Isolated Systems. *Proc. R. Soc. London, Ser. A*, 269:21–52.
- Bowen, D. B., Campanelli, M., Krolik, J. H., Mewes, V., and Noble, S. C. (2017). Relativistic dynamics and mass exchange in binary black hole mini-disks. *The Astrophysical Journal*, 838(1):42.
- Bowen, D. B., Mewes, V., Campanelli, M., Noble, S. C., Krolik, J. H., and Zilhão, M. (2018). Quasi-periodic behavior of mini-disks in binary black holes approaching merger. *The Astrophysical Journal Letters*, 853(1):L17.
- Bowen, D. B., Mewes, V., Noble, S. C., Avara, M., Campanelli, M., and Krolik, J. H. (2019). Quasi-periodicity of supermassive binary black hole accretion approaching merger. *The Astrophysical Journal*, 879(2):76.
- Burke, W. L. and Thorne, K. S. (1970). Gravitational radiation damping. In Carmeli, M., Fickler, S. I., and Witten, L., editors, *Relativity*, pages 209–228, New York; London. Plenum Press.
- Chen, H.-Y., Haster, C.-J., Vitale, S., Farr, W. M., and Isi, M. (2022). A standard siren cosmological measurement from the potential GW190521 electromagnetic counterpart ZTF19abanrhr. *Monthly Notices of the Royal Astronomical Society*, 513(2):2152–2157.
- Combi, L., Lopez Armengol, F. G., Campanelli, M., Noble, S. C., Avara, M., Krolik, J. H., and Bowen, D. (2022). Minidisk accretion onto spinning black hole binaries: Quasi-periodicities and outflows. *The Astrophysical Journal*, 928(2):187.
- Crowley, R. J. and Thorne, K. S. (1977). Generation of gravitational waves. II. Post-linear formalism revisited. *Astrophys. J.*, 215:624–635.
- Csizmadia, P., Debreczeni, G., Racz, I., and Vasuth, M. (2012). Gravitational waves from spinning eccentric binaries. *Class. Quant. Grav.*, 29:245002.
- Cutler, C., Apostolatos, T. A., Bildsten, L., Finn, L. S., Flanagan, É. É., Kennefick, D., Marković, D. M., Ori, A., Poisson, E., and Sussman, G. J. (1993). The Last Three Minutes: Issues in Gravitational-Wave Measurements of Coalescing Compact Binaries. *Phys. Rev. Lett.*, 70:2984–2987.

- Cutler, C. and Flanagan, É. É. (1994). Gravitational waves from merging compact binaries: How accurately can one extract the binary's parameters from the inspiral wave form? *Phys. Rev. D*, 49:2658–2697.
- Damour, T. and Iyer, B. R. (1991). Multipole analysis for electromagnetism and linearized gravity with irreducible Cartesian tensors. *Phys. Rev. D*, 43:3259–3272.
- Dempsey, A. M., Li, H., Mishra, B., and Li, S. (2022). Contracting and expanding binary black holes in 3d low-mass agn disks: The importance of separation. *The Astrophysical Journal*, 940(2):155.
- Dittmann, A. J. and Ryan, G. (2021). Preventing Anomalous Torques in Circumbinary Accretion Simulations. *The Astrophysical Journal*, 921(1):71.
- Dittmann, A. J. and Ryan, G. (2022). A survey of disc thickness and viscosity in circumbinary accretion: Binary evolution, variability, and disc morphology. *Monthly Notices of the Royal Astronomical Society*, 513(4):6158–6176.
- Dlapa, C., Kälin, G., Liu, Z., and Porto, R. A. (2022). Dynamics of binary systems to fourth Post-Minkowskian order from the effective field theory approach. *Phys. Lett. B*, 831:137203.
- D'Orazio, D. J. and Duffell, P. C. (2021). Orbital Evolution of Equal-mass Eccentric Binaries due to a Gas Disk: Eccentric Inspirals and Circular Outspirals. *The Astrophysical Journal Letters*, 914(1):L21.
- Droste, J. (1917). The field of a single centre in Einstein's theory of gravitation, and the motion of a particle in that field. *K. Nederl. Akad. Wetens. Proc.*, 19:197. Reprinted in Gen. Relativ. Gravit. 34, 1545–1563 (2002).
- Duez, M. D. (2025). Black Hole-Neutron Star Binaries, pages 573-617. Springer Nature Singapore, Singapore.
- Duffell, P. C., D'Orazio, D., Derdzinski, A., Haiman, Z., MacFadyen, A., Rosen, A. L., and Zrake, J. (2020).
 Circumbinary disks: Accretion and torque as a function of mass ratio and disk viscosity. *The Astrophysical Journal*, 901(1):25.
- Ecker, C., Topolski, K., Järvinen, M., and Stehr, A. (2025). Prompt black hole formation in binary neutron star mergers. *Phys. Rev. D*, 111:023001.
- Einstein, A., Infeld, L., and Hoffmann, B. (1938). The Gravitational Equations and the Problem of Motion. *Ann. Math.* (2), 39:65–100.
- Ennoggi, L. et al. (2025). Relativistic Gas Accretion onto Supermassive Black Hole Binaries from Inspiral through Merger.
- Farris, B. D., Duffell, P., MacFadyen, A. I., and Haiman, Z. (2014). Binary black hole accretion from a circumbinary disk: Gas dynamics inside the central cavity. *The Astrophysical Journal*, 783(2):134.
- Fung, J., Artymowicz, P., and Wu, Y. (2015). The 3d flow field around an embedded planet. *The Astrophysical Journal*, 811(2):101.
- Futamase, T. and Schutz, B. F. (1983). Newtonian and post-newtonian approximations are asymptotic to general relativity. *Phys. Rev. D*, 28:2363–2372.
- Gayathri, V., Healy, J., Lange, J., O'Brien, B., Szczepanczyk, M., Bartos, I., Campanelli, M., Klimenko, S., Lousto, C., and O'Shaughnessy, R. (2020). Eccentricity Estimate for Black Hole Mergers with Numerical Relativity Simulations. *arXiv e-prints*, page arXiv:2009.05461.

- Gerosa, D. and Fishbach, M. (2021). Hierarchical mergers of stellar-mass black holes and their gravitational-wave signatures. *Nature Astronomy*, 5:749–760.
- Goldreich, P. and Lynden-Bell, D. (1965). II. Spiral Arms as Sheared Gravitational Instabilities. *Monthly Notices of the Royal Astronomical Society*, 130(2):125–158.
- Gottlieb, O., Issa, D., Jacquemin-Ide, J., Liska, M., Tchekhovskoy, A., Foucart, F., Kasen, D., Perna, R., Quataert, E., and Metzger, B. D. (2023). Hours-long near-uv/optical emission from mildly relativistic outflows in black hole–neutron star mergers. *The Astrophysical Journal Letters*, 953(1):L11.
- Goulding, A. D., Pardo, K., Greene, J. E., Mingarelli, C. M. F., Nyland, K., and Strauss, M. A. (2019). Discovery of a close-separation binary quasar at the heart of a z0.2 merging galaxy and its implications for low-frequency gravitational waves. *The Astrophysical Journal Letters*, 879(2):L21.
- Graham, M. J., Ford, K. E. S., McKernan, B., Ross, N. P., Stern, D., Burdge, K., Coughlin, M., Djorgovski, S. G., Drake, A. J., Duev, D., Kasliwal, M., Mahabal, A. A., van Velzen, S., Belecki, J., Bellm, E. C., Burruss, R., Cenko, S. B., Cunningham, V., Helou, G., Kulkarni, S. R., Masci, F. J., Prince, T., Reiley, D., Rodriguez, H., Rusholme, B., Smith, R. M., and Soumagnac, M. T. (2020). Candidate electromagnetic counterpart to the binary black hole merger gravitational-wave event s190521g. *Phys. Rev. Lett.*, 124:251102.
- Graham, M. J., McKernan, B., Ford, K. E. S., Stern, D., Djorgovski, S. G., Coughlin, M., Burdge, K. B., Bellm, E. C., Helou, G., Mahabal, A. A., Masci, F. J., Purdum, J., Rosnet, P., and Rusholme, B. (2023). A light in the dark: Searching for electromagnetic counterparts to black hole–black hole mergers in ligo/virgo o3 with the zwicky transient facility. *The Astrophysical Journal*, 942(2):99.
- Harten, A., Lax, P. D., and Leer, B. v. (1983). On upstream differencing and godunov-type schemes for hyperbolic conservation laws. *SIAM Review*, 25(1):35–61.
- Iyer, B. R. and Will, C. M. (1995). Post-newtonian gravitational radiation reaction for two-body systems: Nonspinning bodies. *Phys. Rev. D*, 52:6882–6893.
- Kidder, L. E. (1995). Coalescing binary systems of compact objects to postNewtonian 5/2 order. 5. Spin effects. *Phys. Rev. D*, 52:821–847.
- Kramer, M. and Wex, N. (2009). The double pulsar system: A unique laboratory for gravity. *Class. Quantum Grav.*, 26(7):073001.
- Lai, D. and Muñoz, D. J. (2023). Circumbinary accretion: From binary stars to massive binary black holes. *Annual Review of Astronomy and Astrophysics*, 61(Volume 61, 2023):517–560.
- Li, R. and Lai, D. (2022). Hydrodynamical evolution of black-hole binaries embedded in AGN discs. *Monthly Notices of the Royal Astronomical Society*, 517(2):1602–1624.
- Li, Y.-P., Dempsey, A. M., Li, H., Li, S., and Li, J. (2022). Hot Circumsingle Disks Drive Binary Black Hole Mergers in Active Galactic Nucleus Disks. *The Astrophysical Journal Letters*, 928(2):L19.
- Li, Y.-P., Dempsey, A. M., Li, S., Li, H., and Li, J. (2021). Orbital Evolution of Binary Black Holes in Active Galactic Nucleus Disks: A Disk Channel for Binary Black Hole Mergers? *The Astrophysical Journal*, 911(2):124.

- Lin, D. N. C. and Papaloizou, J. (1979). Tidal torques on accretion discs in binary systems with extreme mass ratios. *Monthly Notices of the Royal Astronomical Society*, 186:799–812.
- Lorentz, H. A. and Droste, J. (1937). *The motion of a system of bodies under the influence of their mutual attraction, according to Einstein's theory*, pages 330–355. Nijhoff, The Hague. Translated from Versl. K. Akad. Wet. Amsterdam, 26, 392 and 649 (1917).
- MacFadyen, A. I. and Milosavljević, M. (2008). An Eccentric Circumbinary Accretion Disk and the Detection of Binary Massive Black Holes. *The Astrophysical Journal*, 672(1):83–93.
- McKernan, B., Ford, K. E. S., Bartos, I., Graham, M. J., Lyra, W., Marka, S., Marka, Z., Ross, N. P., Stern, D., and Yang, Y. (2019). Ram-pressure Stripping of a Kicked Hill Sphere: Prompt Electromagnetic Emission from the Merger of Stellar Mass Black Holes in an AGN Accretion Disk. *The Astrophysical Journal Letters*, 884(2):L50.
- McKernan, B., Ford, K. E. S., Bellovary, J., Leigh, N. W. C., Haiman, Z., Kocsis, B., Lyra, W., Mac Low, M. M., Metzger, B., O'Dowd, M., Endlich, S., and Rosen, D. J. (2018). Constraining Stellar-mass Black Hole Mergers in AGN Disks Detectable with LIGO. *The Astrophysical Journal*, 866(1):66.
- McKernan, B., Ford, K. E. S., Callister, T., Farr, W. M., O'Shaughnessy, R., Smith, R., Thrane, E., and Vajpeyi, A. (2022). LIGO-Virgo correlations between mass ratio and effective inspiral spin: testing the active galactic nuclei channel. *Monthly Notices of the Royal Astronomical Society*, 514(3):3886–3893.
- McKernan, B., Ford, K. E. S., Kocsis, B., Lyra, W., and Winter, L. M. (2014). Intermediate-mass black holes in AGN discs II. Model predictions and observational constraints. *Monthly Notices of the Royal Astronomical Society*, 441(1):900–909.
- McKernan, B., Ford, K. E. S., Lyra, W., and Perets, H. B. (2012). Intermediate mass black holes in AGN discs I. Production and growth. *Monthly Notices of the Royal Astronomical Society*, 425(1):460–469.
- Mignone, A., Bodo, G., Massaglia, S., Matsakos, T., Tesileanu, O., Zanni, C., and Ferrari, A. (2007). PLUTO: A Numerical Code for Computational Astrophysics. , 170(1):228–242.
- Miranda, R., Muñoz, D. J., and Lai, D. (2016). Viscous hydrodynamics simulations of circumbinary accretion discs: variability, quasi-steady state and angular momentum transfer. *Monthly Notices of the Royal Astronomical Society*, 466(1):1170–1191.
- Mishra, B. and Calcino, J. (2024). Nature vs Nurture: Three Dimensional MHD Simulations of Misaligned Embedded Circum-Single Disks within an AGN Disk. *arXiv e-prints*, page arXiv:2409.05614.
- Moody, M. S. L., Shi, J.-M., and Stone, J. M. (2019). Hydrodynamic Torques in Circumbinary Accretion Disks. *The Astrophysical Journal*, 875(1):66.
- Most, E. R. and Wang, H.-Y. (2024). Magnetically Arrested Circumbinary Accretion Flows. , 973(1):L19.
- Mougiakakos, S., Riva, M. M., and Vernizzi, F. (2021). Gravitational Bremsstrahlung in the post-Minkowskian effective field theory. *Phys. Rev. D*, 104(2):024041.
- Muñoz, D. J., Lai, D., Kratter, K., and Miranda, R. (2020). Circumbinary Accretion from Finite and Infinite Disks. *The Astrophysical Journal*, 889(2):114.

- Muñoz, D. J., Miranda, R., and Lai, D. (2019). Hydrodynamics of Circumbinary Accretion: Angular Momentum Transfer and Binary Orbital Evolution. *The Astrophysical Journal*, 871(1):84.
- Muñoz, D. J. and Lai, D. (2016). Pulsed accretion onto eccentric and circular binaries. *The Astrophysical Journal*, 827(1):43.
- Noble, S. C., Mundim, B. C., Nakano, H., Krolik, J. H., Campanelli, M., Zlochower, Y., and Yunes, N. (2012). Circumbinary magnetohydrodynamic accretion into inspiraling binary black holes. *The Astrophysical Journal*, 755(1):51.
- Ormel, C. W. (2013). The steady-state flow pattern past gravitating bodies. , 428(4):3526–3542.
- Papapetrou, A. (1962). Relativité une formule pour le rayonnement gravitationnel en première approximation. C. R. Acad. Sci. Ser. II, 255:1578.
- Penrose, R. (1963). Asymptotic Properties of Fields and Space-Times. Phys. Rev. Lett., 10:66-68.
- Peters, P. C. (1964). Gravitational Radiation and the Motion of Two Point Masses. Phys. Rev., 136:B1224–B1232.
- Poujade, O. and Blanchet, L. (2002). Post-Newtonian approximation for isolated systems calculated by matched asymptotic expansions. *Phys. Rev. D*, 65.
- Pringle, J. E. (1991). The properties of external accretion discs. Monthly Notices of the Royal Astronomical Society, 248(4):754–759.
- Rendall, A. D. (1992). On the definition of post-Newtonian approximations. *Proc. R. Soc. London, Ser. A*, 438:341–360.
- Ressler, S. M., Combi, L., Ripperda, B., and Most, E. R. (2025). Dual Jet Interaction, Magnetically Arrested Flows, and Flares in Accreting Binary Black Holes., 979(2):L24.
- Ryan, G. and MacFadyen, A. (2017). Minidisks in binary black hole accretion. *The Astrophysical Journal*, 835(2):199.
- Sachs, R. K. (1962). Gravitational Waves in General Relativity. VIII. Waves in Asymptotically Flat Space-Time. *Proc. R. Soc. London, Ser. A*, 270:103–126.
- Sachs, R. K. and Bergmann, P. G. (1958). Structure of Particles in Linearized Gravitational Theory. *Phys. Rev.*, 112:674–680.
- Shi, J.-M. and Krolik, J. H. (2015). Three-dimensional mhd Simulation of Circumbinary Accretion Disks. II. net Accretion Rate. *Astrophys. J.*, 807(2):131.
- Siwek, M., Weinberger, R., Muñoz, D. J., and Hernquist, L. (2022). Preferential accretion and circumbinary disc precession in eccentric binary systems. *Monthly Notices of the Royal Astronomical Society*, 518(4):5059–5071.
- Tagawa, H., Haiman, Z., and Kocsis, B. (2020). Formation and Evolution of Compact-object Binaries in AGN Disks. *The Astrophysical Journal*, 898(1):25.
- Tagawa, H., Kocsis, B., Haiman, Z., Bartos, I., Omukai, K., and Samsing, J. (2021). Eccentric Black Hole Mergers in Active Galactic Nuclei. *The Astrophysical Journal Letters*, 907(1):L20.

- Tang, Y., MacFadyen, A., and Haiman, Z. (2017). On the orbital evolution of supermassive black hole binaries with circumbinary accretion discs. *Monthly Notices of the Royal Astronomical Society*, 469(4):4258–4267.
- Taylor, J. H. (1993). Pulsar timing and relativistic gravity. Class. Quantum Grav., 10:167-174.
- Taylor, J. H., Fowler, L. A., and McCulloch, P. M. (1979). Measurements of general relativistic effects in the binary pulsar PSR 1913+16. *Nature*, 277:437–440.
- Taylor, J. H. and Weisberg, J. M. (1982). A New Test of General Relativity: Gravitational Radiation and the Binary Pulsar PSR 1913+16. *Astrophys. J.*, 253:908–920.
- Thorne, K. S. (1980). Multipole expansions of gravitational radiation. Rev. Mod. Phys., 52:299–339.
- Thorne, K. S. and Kovàcs, S. J. (1975). Generation of gravitational waves. I. Weak-field sources. *Astrophys. J.*, 200:245–262.
- Tiede, C., Zrake, J., MacFadyen, A., and Haiman, Z. (2020). Gas-driven Inspiral of Binaries in Thin Accretion Disks. *The Astrophysical Journal*, 900(1):43.
- van Leer, B. (1979). Towards the ultimate conservative difference scheme. v. a second-order sequel to godunov's method. *Journal of Computational Physics*, 32(1):101–136.
- Wang, H. and Will, C. M. (2007). Post-newtonian gravitational radiation and equations of motion via direct integration of the relaxed einstein equations. iv. radiation reaction for binary systems with spin-spin coupling. *Phys. Rev. D*, 75:064017.
- Will, C. M. and Wiseman, A. G. (1996). Gravitational radiation from compact binary systems: Gravitational waveforms and energy loss to second post-newtonian order. *Phys. Rev. D*, 54:4813–4848.
- Yang, Y., Bartos, I., Gayathri, V., Ford, K. E. S., Haiman, Z., Klimenko, S., Kocsis, B., Márka, S., Márka, Z., McKernan, B., and O'Shaughnessy, R. (2019). Hierarchical Black Hole Mergers in Active Galactic Nuclei. *Physical Review Letters*, 123(18):181101.
- Zackay, B., Dai, L., Venumadhav, T., Roulet, J., and Zaldarriaga, M. (2021). Detecting gravitational waves with disparate detector responses: Two new binary black hole mergers. *Phys. Rev. D*, 104:063030.
- Zeng, J. and Will, C. M. (2007). Application of energy and angular momentum balance to gravitational radiation reaction for binary systems with spin-orbit coupling. *General Relativity and Gravitation*, 39:1661–1673.
- Zrake, J., Tiede, C., MacFadyen, A., and Haiman, Z. (2021). Equilibrium Eccentricity of Accreting Binaries. *The Astrophysical Journal Letters*, 909(1):L13.